NTNU
Norwegian University of
Science and Technology

Characterization of Structure and Optical Properties of Diatoms for improved Solar Cell Efficiency

Anne Kirsti Noren

Nanotechnology
Submission date: June 2011
Supervisor: Gabriella Tranell, IMTE
Co-supervisor: Arne Røyset, SINTEF

Norwegian University of Science and Technology
Department of Materials Science and Engineering

Preface

This master thesis was written during the spring of 2011 at the Norwegian University of Science and Technology (NTNU) in Trondheim. This thesis is the basis for a diploma - one of three student diplomas issued under Solbiopta, a joint research project between NTNU and SINTEF. Initiated in the spring of 2010, Solbiopta is financed by the Research Council of Norway and will be ongoing until 2013. The report is aimed at readers who are involved or show interest in this project and new students who are joining Solbiopta.

First and foremost, I want to express my gratitude to my excellent supervisors - Gabriella Tranell and Arne Røyset. I would like to thank Dr. Tranell for her inspiring attitude and for her support throughout the project. Furthermore, I want to give special thanks to Dr. Røyset, who has played a crucial role in the practical implementation of the project and who has also provided me with a wide array of valuable inputs. I would like to thank Per Erik Vullum for assisting me in carrying out the FIB work and for the front page image. Gratitude is also given to Matilde Chauton and Lasse Olsen at the Department of Biotechnology for providing me with the sample material. Further on I would direct a thank to the rest of the inspiring people in the Solbiopta group. I am also grateful to my fellow students - Lotte Skolem and Petter Ottesen: Thanks for fruitful and inspiring discussions. Finally, the financial support provided by the Norwegian Research Council through the Solbiopta project is gratefully acknowledged.

I hereby declare that the work in this project has been performed independently and in accordance with the examination regulations of Norwegian University of Science and Technology (NTNU).

Anne Kirsti Noren

Trondheim, June 23th 2011

Summary

Interest in renewable energy resources has increased in recent years, and solar cells are one of the areas that have been subject to intensive research. For solar energy to develop into a competitive alternative to fossil fuels, the ratio between cost and efficiency has to be reduced. One of the reasons for low efficiency is the optical losses due to reflection and poor absorption of the red and infrared segment of the light spectrum. Applying more ideal anti-reflection structures and a back-side diffraction layer to increase the path length of light would certainly constitute steps in the right direction. Diatoms, a type of algae, are one of nature's most efficient light harvesting structures. It is suggested that their nano- and microporous silica shell (frustule) possess optical properties that make them attractive options for increasing the efficiency of solar cells. This project aimed at studying the structural and optical properties of selected diatom species and investigating the potential for efficiency enhancements in solar cells through the incorporation of diatoms.

Two different species, *Coscinodiscus wailesii* and *Coscinodiscus sp.*, were investigated through the use of a scanning electron microscope. They were found to have different structures, with the frustule of *Coscinodiscus sp.* as having a more regular pore pattern and a more complex structure consisting of several silica layers. The *Coscinodiscus sp.* structure was chosen as the foundation for modelling a diffraction grating in GD-Calc, a Matlab implemented simulation software based on rigorous coupled-wave analysis. The diffraction simulations were carried out both on the grating in air and on the grating incorporated in solar cell-like setups.

The simulations demonstrated that the diatom structure diffracted light efficiently to higher orders. It was also shown that the anti-reflection structure provided low levels of reflection for a given set of geometric combinations. The back-side diffraction grating reflected light with efficiencies of 0.9, however, the level of diffraction to higher orders was below 0.1.

This study shows that that diatom frustule exhibits interesting diffraction grating properties which should be investigated further, both for solar cell schemes and for other applications.

Contents

List of Figures

1 Introduction

1.1 Background

The interest in sustainable energy resources has increased in recent years due to climate change and limited fossil fuel reserves, as well as the need to secure future energy supplies. The sun is an abundant energy resource, with the capacity to deliver some 5,000 times the current annual energy demand. Therefore, in many energy scenarios, solar-generated electricity has the potential to dominate electricity production within the next 50 years. In order to realize this potential, the cost of solar cell production has to decrease while simultaneously realizing higher efficiency levels. The incorporation of nano-porous silica from diatoms as optically active layers is suggested by some as a route with the potential to improve the performance and profitability of solar cells [14] [16] [8].

Diatoms are one of the most common types of algae and they can be found in almost every aquatic habitat on earth [25]. These unicellular organisms are encased in a biomineralized cell wall, named frustule, which is made up of hydrogenated amorphous silica. The frustules possess intricately designed two- and three-dimensional patterns with regularities on both on the micro- and nano-scales. Estimations indicate that approximately 200,000 extant species can be found [10]. The shape and pattern of the frustule is usually specie specific and the various species show a wide range of diversity in form. Since the periodicity of the pattern is in the order of the wavelength of visible light, it is believed that frustule provides an advantage for harvesting light, while providing physical protection of the cell at the same time [27].

For a variety of reasons, diatoms have received a fair amount of attention over the past decades and centuries. The first studies of diatoms were carried out by hobby microscopists from the British gentry; The diatoms were popular study objects due to their fascinating structure. In modern times, the diatom populations have been viewed as indicators of environmental change. Indeed, diatoms contribute to as much as 45% of the total primary production in the ocean [18], making them crucial change indicators. Only in recent years have the organisms gained attention among physicists and material scientists due to their intricate nano-scale silica structures.

Aside from their potential application in solar cells, diatom nanotechnology has a multiplicity of other potential applications. Photoluminescent diatom frustules can be exploited for creating gas-sensing devices. Recent studies have already demonstrated their ultra-sensitive abilities to detect a series of organic vapours and gases [2]. Since silica is biocompatible, chemically inert

and biodegradable, the diatom silica shell is a promising biomaterial for drug delivery applications. By exploiting the nano-sized pores, the frustules can be designed and functionalized for the controlled release of drugs [10]. The diatom's small-sized pores translates into frustule valves with a potential for diffusive separation of molecular or nanoparticular components [17]. In short, there are a manifold of possible applications based on the porous biosilica from diatoms. When compared to synthesized or fabricated nanostructures, one of the great advantages with the nanostructured biosilica from diatoms is the non-demanding process in making them. Diatom cultivation only requires light and simple nutrients. This also makes the diatom structures potentially applicable to solar cell technology.

There are several suggested routes for improving the conventional silicon solar cell. For starters, efficiency can be increased by addressing the various loss mechanisms. The reflection from silicon is around 40% of incident power flux [12] and reflection loss is, therefore, a significant contribution to the overall loss of efficiency. By applying an antireflection coating and texturing the surface of the solar cell, reflection can be reduced to lower values [13]. Current texturing methods are mainly based on anisotropic etching. However, this technique lacks in versatility since it cannot be applied to polycrystalline silicon. A layer of diatoms has the potential to serve as a texturing surface due to the periodic presence of micro- and nano-sized pore structures and the low refractive index of silica [8]. Making thinner and hence less expensive solar cells, while at the same time maintaining a high efficiency, is another way to improve the cost-to-efficiency ratio. However, thin-film silicon solar cells have a poor rate for absorbing the red and infrared sections of the solar spectrum due to the shortened path-length of light. Therefore, such a solar cell has to be equipped with a back-side diffraction grating in order to increase the length of the light path inside the solar cell. A satisfactory method for fabricating such structures has yet to be developed. Diatom structures could serve as a possible solution to this challenge.

1.2   Objective

The goal of the Solbiopta research project, which this master thesis is a part of, is to investigate the potential for enhancing the efficiency of solar cells by incorporating diatom frustules. The aim of this thesis was to contribute to the overall goal by characterizing the structures and optical properties of diatoms. The diatom genus, which was the subject of this investigation, was *Coscinodiscus*. The structure was characterized by utilizing scanning electron microscope (SEM). The results from the characterization process and the measurements of the structural parameters did together constitute the

foundation for constructing a model of a simplified diatom structure. The model was constructed in a GD-Calc (Grating Diffraction Calculator), which is a simulation software based on rigorous coupled-wave analysis (RCWA).

The questions which were addressed in this study were: What does the structure of the *Coscinodiscus* diatom species look like? Can it be described with a few parameters and modeled in GD-Calc? How can the simulation software GD-Calc be used to simulate the diffraction of light from this model grating? How does a model of the diatom frustule structure diffract light? What would be the most ideal diatom structural dimensions for the purpose of diatoms as diffraction grating or in solar cell technology? Would incorporating these structures on the frontal and back-side surfaces increase the light absorption capacities of solar cells?

The modeling and simulation part were dependent on the result from the structural characterization. The characterization results are for this reason presented prior to the description of the modeling and simulations, in other words; there are two separate chapters presenting experimental method and two chapters describing the results. The characterization work was done by the author, with the exception of the FIB work which was done with assistance from Per Erik Vullum. Some parts of the source code (marked with "'ar'" in the filename) was created by Arne Røyset. The function gdc_ak_eff was also developed mostly by Dr. Røyset.

2 Theory and Previous Work

This study spans fields like biology, physics and material science - all of which have their own scientific terminologies. The aim has been to avoid making an overly comprehensive theory chapter, while at the same time providing a framework sufficient enough for readers with various scientific backgrounds. Each part, therefore, contains some basic theory followed by material aimed at readers with more experience in the field. Relevant optical theory is included in the first chapter, however, the report can not take the size of a textbook. Unexperienced readers can find "Optics" (1974) written by Hecht as useful starting point for more advanced optical theory. The state of the art of current solar cell technology is presented in order to clarify the motivation behind incorporating diatoms into solar cells. The basic operation principal of solar cells will be described as well as the definition of solar cell efficiency and efficiency loss mechanisms. For readers unfamiliar with this area, additional background material can be found in "Solar Cells" (1982), authored by Martin A. Green. Furthermore, this piece will present some possible ways of applying diatom frustules to solar cell technology. Since the field of diatoms is unfamiliar for most material scientists and physicists, there will be a brief introduction of the diatom life form with the aim of improving the understanding of the silica cell wall structure. The book entitled "The Diatoms" (1990), by Round, Crawford and Mann, is recommended for more extensive reading on the topic. An introduction to the limited number of studies done on optical properties of diatoms is found at the end of this chapter. A short glossary of useful terms related to the diatom frustules structure is included in appendix A.

2.1 Optical theory

The following sections include a basic description of the optical theory relevant for this study.

2.1.1 Light

Light or visible light is the portion of the electromagnetic spectrum with wavelengths between 400 - 780 nm. Electromagnetic waves can generally be the described by a wave equation given as

$$\psi(\mathbf{r}, t) = A cos(\mathbf{k} \bullet \mathbf{r} - \omega t - \varphi) \tag{1}$$

Here, A is the amplitude of the wave, $\mathbf{k}$ is the wave vector, $\mathbf{r}$ is the position

vector in three-dimensional space and φ is the phase which describes how two waves can be out of sync. The wave vector has a magnitude which is inversely proportional to the wavelength and a direction which is in the direction of wave propagation. Electromagnetic waves oscillate perpendicular to the direction of propagation. If these oscillations are aligned, the wave is said to be polarized. The plane made by the propagation direction and a vector perpendicular to the plane of a reflecting surface is known as the plane of incidence. The component of the electric field parallel to this plane is termed p-like and the component perpendicular to this plane is termed s-like. Light with a p-like electric field is said to be p-polarized, and s-like electric field is said to be s-polarized [11]. Visible light is unplolarized.

2.1.2   Refractive index

The refractive index of a medium is a measure of the speed of light in that medium. It is expressed as a ratio of the speed of light in vacuum (c) relative to the phase speed (v_p) of the wave in the medium in question.

$$n = \left(\frac{c}{v_p} \right) \tag{2}$$

This means that a high refractive index will prevail in a medium where light has a low phase speed. The refractive index can be complex, ñ=n+iκ. While the real part (n) indicates the phase speed, the imaginary part (κ) represents the amount of absorption loss when the electromagnetic wave propagates through the material. Both the real and the imaginary parts of the refractive index are dependent on the wavelength of the electromagnetic wave. The refractive index of air is generally set to 1 since the difference between the refraction of light in air and its refraction in a vacuum is small [11]. In the software GD-Calc, the term permittivity is used instead of refractive index. The permittivity is simply the square of the complex refractive index. The permittivity can be found from a dispersion equation;

$$\epsilon_v = \frac{\epsilon_{fin} + \left(\left(\epsilon_s - \epsilon_{fin} \right) * \omega_t^2 \right)}{\left(\left(\omega_t^2 \right) - \left(\omega_v^2 \right) + i * \gamma_0 * \omega_v \right)} \tag{3}$$

were ϵ_{fin} and ϵ_s are permittivity constants, ω_t and γ_0 are constants with unit eV. γ_0 must be zero for lossless real index. ω_v is the quantum energy the electromagnetic wave (1239.8 eV nm/ λ).

2.1.3   Reflection

Snell's law describes the relationship between angles and velocities of light.The relation between the angle of incidence and transmission θ_i,θ_t, and the refractive index of incident, n_i medium and transmitted medium, n_t are as following,

$$n_i sin\theta_i = n_t sin\theta_t \tag{4}$$

An other relation resulting from from the derivation of Snell's law, states that the angle of incidence is equal to the angle of reflection. The behaviour of light when it moves between media of differing refractive indexes is described by the Fresnel equations. A simplified Fresnel equation calculates the intensity of light that is reflected under normal surface incidence.

$$R = \left(\frac{n_1 - n_2}{n_1 - n_2}\right)^2 \tag{5}$$

R is the reflection coefficient when light travels from a medium with a refractive index of n_1 to a medium with refractive index of n_2. The value of R varies from 0 (no reflection) to 1 (all light reflected) and is usually quoted as a percentage. When exceeding an incidence angle known as the critical angle, all light is reflected as it moves from a medium with greater density into a one with a lower density ($n_1 > n_2$). This phenomenon is known as total internal reflection - a process that coincides with the formation of evanescent waves, where the wave vector is imaginary. The amplitude of evanescent waves drops of exponentially as it penetrates a less dense medium.

2.1.4   Diffraction

Diffraction refers to a variety of phenomena that occur when a wave encounters an obstacle. While diffraction occurs whenever propagating waves encounter obstacles, its effects are generally most pronounced for wavelengths that are roughly similar to the dimensions of the diffracting objects. If the obstructing object provides a multitude of closely-spaced slits, a complex pattern of varying intensity can result. This is due to the superposition, or interference, of different parts of a wave that travel through different paths to reach the observer. The phases of the waves from each slit will vary from one another, and will partially or totally cancel one another out. However, all the waves will all be in phase in conditions where the path differences between the light from adjacent slits is equal to the wavelength, λ (see figure 1). This occurs
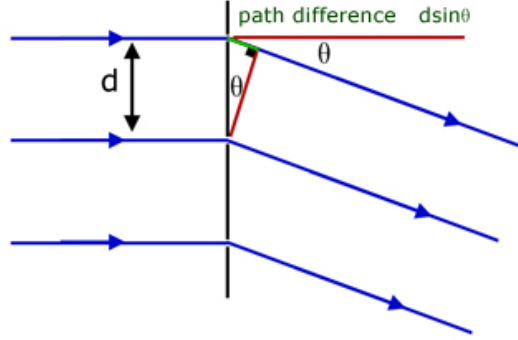
Figure 1: The relation between path difference and angle of transmitted light
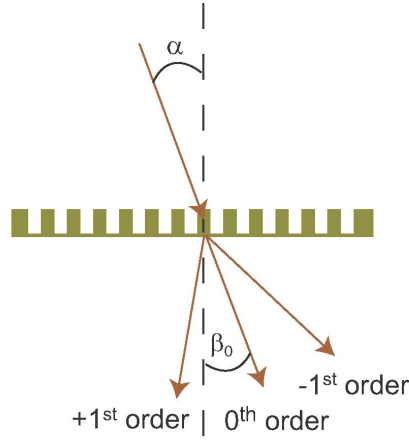
Figure 2: Transmitted light diffraction orders. Illustration from [24].

at angles θ, which satisfy the relationship $d * sin\theta/\lambda = m$, where d is the separation of the slits and m is an integer. Thus, the diffraction of light will be at a maximum at angles θ_m, as given by

$$dsin\theta_m = m\lambda \tag{6}$$

The light that corresponds to the wave that is transmitted or reflected at the same angle as the angle of incidence is named the zero order, and is denoted m_1, $m_2 = 0$, 0. The other maxima occur at larger angles and are denoted by m_1 and m_2 integers that correspond to the distance from zero order (see figure 2).
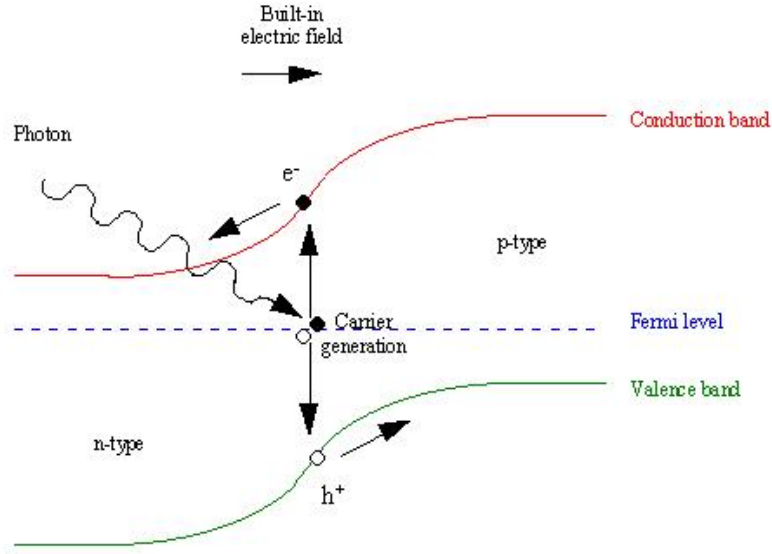
Figure 3: Principle of a photovoltaic device.

2.2   Solar cell

2.2.1   Solar cell operation principles

The principle for the operation of solar cells is based on the ability of semiconductors to convert sunlight directly into electricity by exploiting the photovoltaic effect. The photovoltaic effect describes how voltage or a corresponding electric current can be created within a material upon its exposure to light. Energy from absorbed light excites electrons from occupied low energy states in the valence band to unoccupied higher energy states in the conduction band. This can also be described as charge separation of holes and electrons. The mobile electrons are then transported through the p-n junction with the electric field as a driving force, thus producing electric current across the device as seen in figure 3

2.2.2   Solar cell efficiency

For solar cells to become a competitive alternative to energy produced from fossil fuels, the ratio between cost and efficiency needs to be reduced. Efficiency η is defined as the ratio of power P_{max} produced by the cell at the maximum power point under standard test conditions to the power of the radiation

Figure 4: Pmax is the area of the larges rectangle under the IV-curve
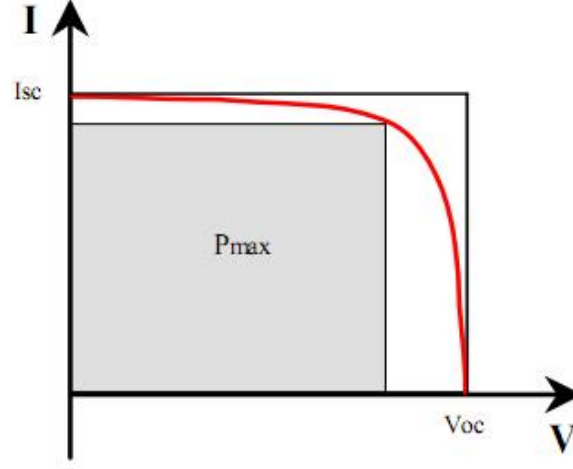
incident upon it, P_{in}.

$$\eta = \frac{P_{max}}{P_{in}} \tag{7}$$

The maximal power produced by the solar cell can be derived from the cells current-voltage curve, which give a full characterization of the electric behavior of a photovoltaic cell, see figure 4.

More about the background for the IV-curve can be found in in Solar cells (1982) by Martin A. Green.

2.2.3   Loss mechanisms

Several loss mechanisms limit the ability of solar cells to exploit all of the incident solar energy. Photons with energy below the band gap cannot be absorbed by the semiconductor material and will instead be transmitted through the material. The energy from photons that exceed the band gap energy will be dissipated as heat. These two mechanisms are fundamental losses which reduce the maximum theoretical efficiency of a single threshold solar cell to 48% [28]. Loss in the solar cell is produced where electrons recombine with holes before they reach the junction. Recombination is most common in the face of impurities or defects in the crystal structure and on the surface of the semiconductor. Recombination leads to both voltage and current loss.

Optical losses in solar cells occur when light is reflected from the front surface and when a particular part of the wavelength spectra is poorly absorbed

in the active material. In bulk silicon solar cells, surface reflection is the dominant loss mechanism. Loss due to poor absorption of the red- infrared segment of the spectrum is most significant in thin-film solar cells [15]. These are the types of inefficiencies that can potentially be reduced through the incorporation of diatoms. There are a number of ways of reducing these optical losses. Reflection can be reduced by attaching anti-reflection (AR) structures on the solar cell surface. For thin-film solar cells the solution is to increase the optical path length within the solar cell through the use of back-side diffraction gratings. Anti-reflection structures and back-side diffraction gratings will be described more in detail in the following sections.

2.2.4 Anti-reflection structures

Ideally, anti-reflection structures on solar cell surfaces should lead to zero reflection loss that covers an extended solar spectral range for all angles of incidence [15]. Omni-directional AR (omni-AR) structures for solar cell applications have been a subjected to intensive research [6] [23] [5]. There are three major types of non-absorbing omni-AR structures: single or multilayer quarter-wavelength film stacks, textured surfaces, and graded index AR-structures. The two first alternatives are relevant for this study.

The single or multilayer quarter-wavelength film stacks greatly reduce reflection by making use of phase changes and the dependence of the reflectivity on index of refraction [3]. A single quarter-wavelength coating of optimum index can eliminate reflection at one wavelength. Multi-layer coatings can reduce the loss for the entire visible spectrum. The idea behind AR coatings is that the creation of a double interface by means of a thin film gives you two reflected waves. If these waves are out of phase, they are partially or totally cancelled. If the coating is a quarter wavelength in thickness and the coating has an index of refraction that is less than the refractive index of silicon then the two reflections are 180 degrees out of phase, see figure 5. However, this approach is challenged by the scarcity of materials that possess the correct indexes and good optical transparency, as well as the challenge of precisely controlling the film thickness [15]. A thin film of (SiN_x) for silicon solar cells is often used as a cost effective approach. Yet, this single-layer AR coating only reduces reflectivity within a limited spectral range under normal surface incident conditions.

The textured surface AR structures on solar cells reduces reflection by directing reflected light back into the texture on the surface, as seen in figure 6. Of the textured surface AR structures, the most successful example is the anisotropic etching of single crystal Si(100) surface in a solution containing potassium hydroxide (KOH) [4]. However, the anisotropic etching method is hazardous
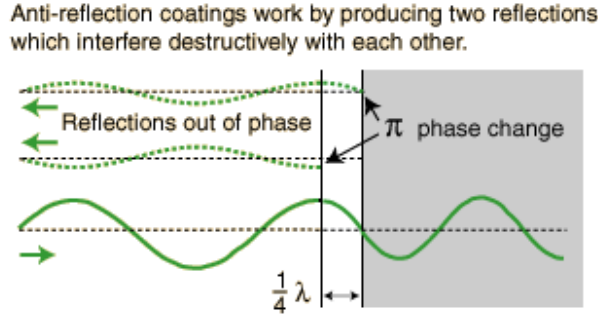
Figure 5: Anti-reflection coatings work by producing two reflections which interfere destructively with each other. Illustration from hyperphysics.phy-astr.gsu.edu.
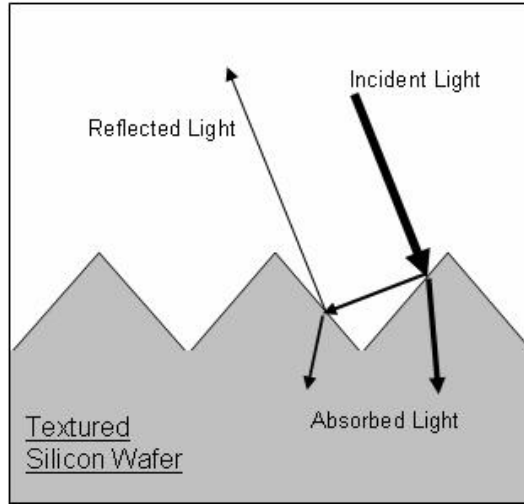
Figure 6: Texture layer leading to increased absorption in silicon wafer.

and it does not apply to poly-crystal Si and Si(111) wafers. Likewise, this technique cannot be used on thin-film solar cells since the etching depth would exceed the thickness of the wafer. For these reasons, the development of better texturization techniques, potentially involving diatoms would be advantageous.

2.2.5   Back-side diffraction grating

The purpose of back-side diffraction gratings is to increasing the probability of absorption of photons by increasing the path length of light inside the semiconductor material. The grating diffracts light in to higher orders and thereby increases the path length of the light. Theoretical studies of a back-side diffraction grating have been done by Gjessing *et. al.*(2010) A grating

comprising silica cylinders was positioned above a silica layer on an aluminium substrate with amorphous silica on top. The grating had was defined by a period, p, and a SiO_2 fill factor ff, which was varied to find the ideal parameters. The optimal parameters was found to be close to 0.9 μm for p and around 0.7 for the SiO_2 fill factor [9]. The lack of practical implementation of this concept are point out.
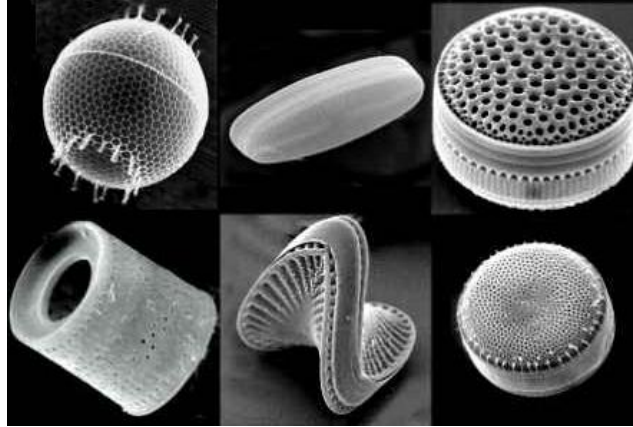
Figure 7: Diversity of diatom silica structures.

2.3   The diatoms

2.3.1   The life form of diatoms

Diatom populations can exist as single cells, filaments (a long chain of cells) or colonies. In this study, diatoms living as single cells and filaments have been investigated. Most species live in open water (pelagic), although some live as surface films on the water-sediment interface (benthic) [25]. For the purpose of organizing diatoms into a monolayer on a substrate, the benthic diatom species would be of interest. Most species are autotrophic, meaning that they are capable of synthesizing their own nutriments from inorganic substances by using the energy from light. Some species of diatoms can, however live, hetrotrophically - i.e. without sunlight - and can instead obtain energy by taking in organic substances [25]. Growing diatoms hetrotrophically is interesting from an industrial point of view since this method gives a higher growth rate and produces a higher number of algae. Some of the species included in this study can be grown both autotrophically and hetrotrophically.

2.3.2   Cell cycle, biomineralization and frustule structure.

The diatom silica frustule is formed by biomineralization during vegetative (asexual) reproduction. The mechanism behind this process, together with the frustules structures, will be described in this section. The silica cell walls of diatoms consist of two parts, named thecae, which overlap one another like the two halves of a petri dish. The two thecae are correspondingly termed hypotheca and epitheca and consist of two valves - the hypovalve and the epivalve - and girdle bands, see figure 8. The epitheca is slightly larger than
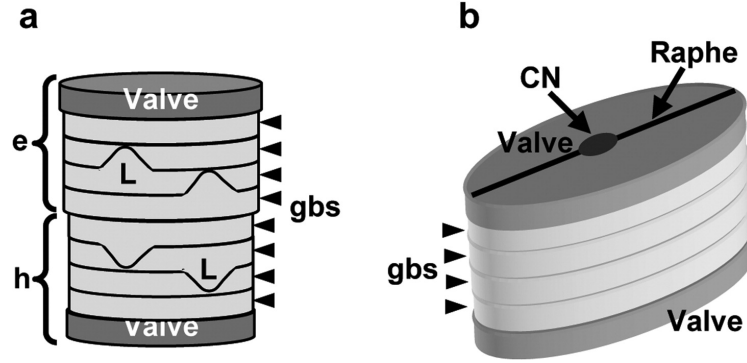
Figure 8: Schematic diagram of diatom cell wall structure. (a) Diagram of the features of centric diatom cell walls. Vales at the top and bottom are labelled. The epitheca and hypotheca are labelled as (e) and (h) respectively. Arrows are used to locate the girdle bands (gbs). (b) Diagram of pennate diatom cell wall features. Valves and girdle bands are labelled as they are in diagram a. On the upper valve, they are denoted as the central nodule (CN) and raphe. Image and text from Hildebrand (2008)

the hypotheca [25]. A glossary of diatom terminology describing the different valve structures is included in Appendix A.

The diatoms usually reproduce by mitotic cell division, where one mother cell divides into two daughter cells, see figure 9. During the division of diatom cells, each of the daughter cells will keep one of the valves from the mother cell (figure 8). These valves will both become the large epivalve for each of the daughter cells. New hypovalves will be produced at the interface between the two cells during the division [1]. Prior to a new cell division, the cell needs to grow to around twice its initial volume. Because of their rigid structure, diatom cells can increase in only one direction [25]. To enable this expansion, girdle bands will grow between the two thecae and the volume of the cell will increase [19]. Because the new valves are formed within the confines of the parent frustules, the mean cell size of a given population will decrease with each cell division. Size will be restored through meiosis (sexual reproduction) by formation of an auxospore, a specialized cell without a silica cell wall. The auxospore will swell to maximum size and new thecae will be synthesized inside of it.

2.3.3   Size and micro structure

Since there exist 200 000 different species, there is a wide range of shapes and structures. It is known that even if the size of the diatoms changes in the cell
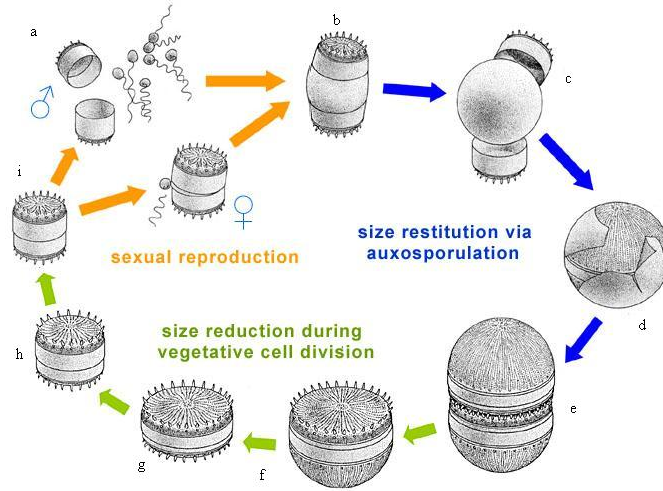
Figure 9: Life cycle of diatoms. (a) Formation of motile gaments (sex cells). (b),(c) Formation of auxospore (d) Auxospore wall breaking open to reveal initial cell. (e) First division of initial cell to form two new normal hypovalves back to back. (f) One of the cells from stage (e) with a normal valve and an initial cell valve. (g) A cell formed following several divisions of (f). (i) A Small cell which will give rise to either the male or female gametes. Source: www.ces.ernet.in

cycle, the size of the features in the valve is constant [8]. Only the number of such features in the valve varies. This means that material with homogenous pore size can be obtained from a culture of diatoms. However, the periodic pattern of pores which are attractive for the purpose of this study are only found in some of the species. The size of the openings varies from some tens of nanometers to some a few micrometers. Some of the diatom species do not exhibit a hierarchical pore pattern, with pores inside of other pores in three levels. The structure of seven different species grown at NTNU have been described in a previous study [22].

2.3.4 Optical properties of diatoms

This section describes previous studies of optical properties of diatoms and research on diatoms in solar cell applications. The number of studies on both of these topics are limited.

The most sensational result is found by Rorrer *et.al* which claim to have tripled the efficiency in dye senzitised solar cells by adding diatoms with metabolically incorporated TiO_2. It has been suggested that the increased efficiency is due to increased interaction between the dye molecule and the light since the light

"bounce" around in the diatom pores. However, the paper from this study is not yet published.

In previous studies carried out by Stefano *et. al* it was found that *Coscinodiscus wailesii* can narrow down a 100 μm red laser beam to less than 10 μm at a distance of 104 μm after transmission. The focusing effect was attributed to a coherent superposition of the unfocused wave fronts coming from the areolae. The light scattered by the pores was found to interfere constructively at a fixed distance [26].

The photonic crystal properties of diatoms have been investigated by Fuhrman *et al.*(2004) [8]. Important for the discussion of the spectral range for which the cell wall acts as a photonic crystal, are the physical dimensions of the periodic structures and the refractive-index contrast. The refractive index of the silica shell was measured to be 1.43 with index matching liquids. It was shown that the optical properties of the diatom shell can influence incoming light by coupling into waveguides with distinct photonic crystal modes [8]. In general, electromagnetic waves incident on a photonic crystal structure are reflected, refracted and scattered due to the refractive index alternation of the structures. Superposition of the resulting waves can lead to a nearly perfect reflection over a certain frequency range. These properties are attractive for 2D- backside diffraction gratings for solar cells to double the path length of light trough the semiconductor material.

3   Method - Characterization

This section provides a description of the diatom structural investigation procedure. The first part includes a brief description of the investigated diatom genus *Coscinodiscus* and the sample preparation method. In the following section are the characterization techniques with detailed operational settings described. SEM was the main tool used to study the diatoms. Focused ion beam (FIB) was utilized in order to cut cross sections. A schematic model was developed based on the SEM images and the characteristic structural parameters were established. The software "Paint" was used to make sketches to describe the structure. Measurements were done to find average values of the structural parameters.

3.1   Material

The particular species of diatoms that were used in the study belong to the genus *Coscinodiscus*. This genus was chosen due to its large size and well ordered periodic pore patter. Culture containing the species *Coscinodiscus wailesii* (*C. wailesii*) was ordered from a diatom species bank and it was grown at the Institute of Biotechnology at NTNU under the conditions described in the following setction. Other species included in the study originated from diatom material collected from the Trondheim's fjord through the use of a landing net. Since the exact species is unknown, these samples are only referred to as *Coscinodiscus sp.* (*C. sp.*). *Coscinodiscus* is a large centric diatom typically 160-500 μm in diameter. In terms of volume, it is one of the largest diatoms. [25] The genus is known to be robust and demonstrates a wide tolerance to variations in temperature, salinity and nutrients. *Coscinodiscus* is very common in the Trondheims fjord during the blooming season. There are at least 400 different species in this genus and the most widely studied species is *C. wailesii* [10]. According to literature, *C. wailesii* cells complete their first cell division within 48 hours. Each *C. wailesii* cell is cylindrical, with the pervalvar axis size approximating or equal to the diameter of the cell, thus giving the appearance of a square or rectangular shape when viewed in girdle view, see figure 10 of living diatom cell. For further discussion of the frustule morphology of *Coscinodiscus*, see Gran Angst (1931) and Hasle Lange (1992).
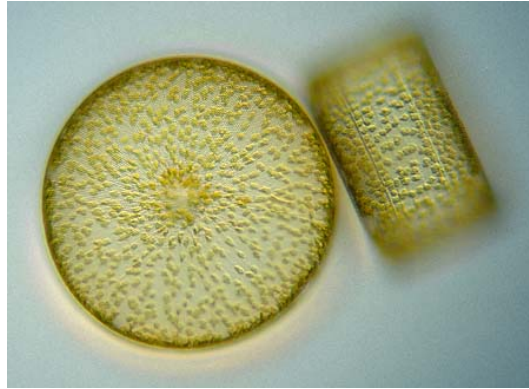
Figure 10: Living Coscinodiscus with visible chloroplasts, in valve view to the left and mantle view to the right

3.2   Sample preparation

The *Coscinodiscus wailesii* have been cultivated in enriched seawater medium (f/2). In order to optimize the conditions for diatom growth, Si(OH) and carbon are added regularly and the culture was subject to constant aeration by using normal pressurized air. This species grows phototrophically (with light), and is, therefore, subjected to artificial sunlight in order to obtain optimal lighting conditions. The removal of organic material from the diatom silica frustule has been done in accordance with two different procedures. In the protocol described by Throndsen *et al.* (2007) HNO_3 and H_2SO^4, has been used to isolate the frustule. These acids dissolve the proteins in the girdle bands and, as a consequence, the hypothecae and epithecae are separated. The second protocol, which was originally described by Schmid and Schulz and modified by Jeffryes *et al.*, involves treating diatoms with sodium dodecyl sulfate and ethylenediaome tetra acid (EDTA). Treating the diatom cells with the SDS detergent separates organic cell matter from the frustule biosilica, but does not remove the girdle band proteins. Therefore, the epitheca and hypotheca remain attached. The cleaned diatom frustules are stored in methanol at -20 degrees Celsius. Pipettes are then used to transfer a volume of $3\mu l$ of the frustules suspension to the substrate. The methanol from the droplet trickles onto the substrate and evaporates within a few seconds, leaving the frustules attached to the substrate. TEM grids made from carbon film-coated copper was utilized as sample holders. The TEM grids are useful since the electrical conduction are good and charge-up is avoided, even with the nonconductive silica. Aluminium stubs have been employed in investigations with Ultra TM55. These samples were coated with gold using a JEOL JFC-1600 Auto Fine Coater (JEOL, Tokyo, Japan) with thicknesses of 4 nm.

3.3   Characterization

I order to understand the optical properties of diatoms, gaining knowledge about their structure and morphology is the first important step. Studies of the techniques most convenient for diatom investigation have been carried out earlier [22]. In accordance with prestudies, scanning electron microscope (SEM) was found to be the most convenient technique. Therefore, SEM was used to investigate the diatom samples. While a light microscope can also give useful information, using visible light in structure investigation would be inferior since the structure is believed to diffract and affect this wavelength spectra. FIB was used to make cross sections, which were then imaged with the electron beam in the dual beam instrument. These cross-section studies were only applied to the material collected with a landing net. The *Coscinodiscus* species are large and it is possible to see them with the naked eye. It was, therefore, easy to confirm the presence of the material on the substrate. The aim of structure characterization was to perform measurements of the structural variable in order to find the average and, thereafter create a sketch that could serve as the starting point for Matlab-based modeling. The measurements of structural parameters are done through the SEM software. Together with the geometry, the refractive index determines the optical properties and the degree of light diffraction in a material. It is, therefore, important to obtain an impression of the morphology of the material to see if it consists of massive silica, or maybe some percentage of air.

3.3.1   Scanning electron microscope

The SEM creates images of the sample surface by scanning it with a high energy beam of electrons in a raster scan pattern. Electrons interact with the atoms that make up the sample, producing signals which contain information about the sample's surface topography and composition. In ideal conditions, SEM can have a resolution of between 1nm to 20nm. One drawback with this instrument is the need for coating the nonconductive samples in order to prevent a charge-up of electrons. It is possible that the coating can hide surface features with sizes that fall within the nanometer range. However, the advantage of this technique is its ability to provide information about both the topography and the composition without the need of using an additional instrument. High resolution images are obtained quickly and easily. The contrast is produced by variations in the number of electrons that reach the detector. The number of electrons generated from a point on the sample is dependent upon the elements present in the sample as well as the geometry of the sample. It must be kept in mind that SEM images do not necessarily reveal the true topography.

Two different SEMs have been utilized in this study. Hitachi's S-5500 (In-lens) ultra high resolution S(T)EM is situated in the clean room at NTNU nanolab. With a 0.4 nm resolution at 30 kV and a 1.6 nm resolution at 1 kV, this model is claimed to hold the world's record on SEM resolution. The magnification ranges from 60 to 2,000,000X. Moreover, since this instrument is a scanning transmission electron microscope (STEM), bright field and dark field imaging are possible. However, since the sample is positioned in a gap of the split objective lens pole piece, the working distance cannot be adjusted and the sample tilting angle is limited to 25 degrees. Hence, the sample size is limited to 5 x 8 mm. In this study images were acquired at voltages of 2 kV and currents of 7nA. The species *C. sp.* was investigated with this instrument.

The Zeiss UltraTM55 FEG-SEM, located in F-362 in the Metallurgical Department at NTNU, has also been used. This instrument is equipped with an EDAX EDS detector, an in-lens (SE) secondary electron detector and an in-lens backscattered electron detector (BSE). It has a resolution of 1nm. The advantage with this SEM when compared to the one mentioned above is fact that this one allows for the possibility of rotating the sample up to 70 degrees. The Zeiss Ultra TM55 has been useful when studying the cross sections that were fabricated with the FIB. Compared to the STEM, it gives a better impression of the three-dimensionality of the sample. This instrument was used to investigate *C. wailesii*. Voltages of 3kV, aperture of 30 and working distance of 7mm was used.

3.3.2   Focused ion beam

Scanning through the use of a focused ion beam makes it possible to obtain images. In addition, the FIB allows fabricated cuts to be made. The FIB utilized in this study is a dual beam device situated at the NTNU Nanolab. Dual beam means that it has both an electron source for SEM imaging and a Ga ion source for FIB imaging. Ion currents higher than 48mA could not be used, since high levels of current would destroy the diatom valve completely. The parameters needed to describe the process is the ion current used for cutting. 28mA was used when making "cleaning cross section", the finest possible type of cut. In cross-section investigations, is useful to determine the structure of the biosilica in order to see whether it is porous or solid and to measure the thickness of the valves. A voltage of 10kV was used for the SEM imaging.

4   Result - Characterization

Both *C. wailesii* from culture and *C. sp.* from landing net material were investigated in this study. A brief description of the *C. waiilesi* structure is given and the structure is presented with representative SEM images. *C. sp.* was chosen as the subject of in depth studies and modeling, and its structure is, therefore, described more in detail. The results from the investigations of *Coscinodiscus sp.* structures are summarized by SEM images, a description of the structure, sketches and a table that summarizes the measurements of structural parameters. The results are presented with a focus is on providing the information relevant to the optical properties of the frustule. The description can, therefore, not be read as a full biological diagnostic description. Tables of measurements and more SEM images are included in Appendix B.

4.1   Structure of *Coscinodiscus wailesii*

C. wailesii from culture were investigated in the STEM in both transmission and secondary electron modes. These diatoms were found to have a homogeneous size distribution of 220 ± 15 μm in radius. The valve face is slightly concave and the transition from valve face to valve mantle is abrupt, forming a near 90 degree angle. The valve face exhibits a radiating pore pattern consisting of circular pores (areolae) with a size of 1.1 ± 0.2 μm (see figure 11). The areolae contain smaller pores, named cribral pores, which have a radius of 210 ± 13 nm (see figure 12). The majority of the cribra pores deviate from the circular form. *C. wailesii* have only a single layer of silica in the valve. The centre of the valve face has a hyaline area (not perforated by pores) due to the variable termination of the radial rows of areolae in valve centre.

4.2   Structure of *Coscinodiscus sp.*

The *C. sp.* sample material was cleaned according to the SDS protocol, and the samples were investigated by the STEM in secondary electron mode. The size distribution was found to be less homogeneous than *C. wailesii*, with a radius of $180\pm35\mu$. This is natural since the sample is harvested in the fjord where the individual diatoms can exist at different stages in the reproduction process. It was found that *C. sp.* had the same overall shape as *C. wailesii*, with the same slightly concaved valve face (see figure 13). Instead of a radiating pattern of pores, the *C.sp.* have a hexagonal pore pattern. Since the valve face is circular, the hexagonal pattern cannot be perfect. Yet the pattern is still
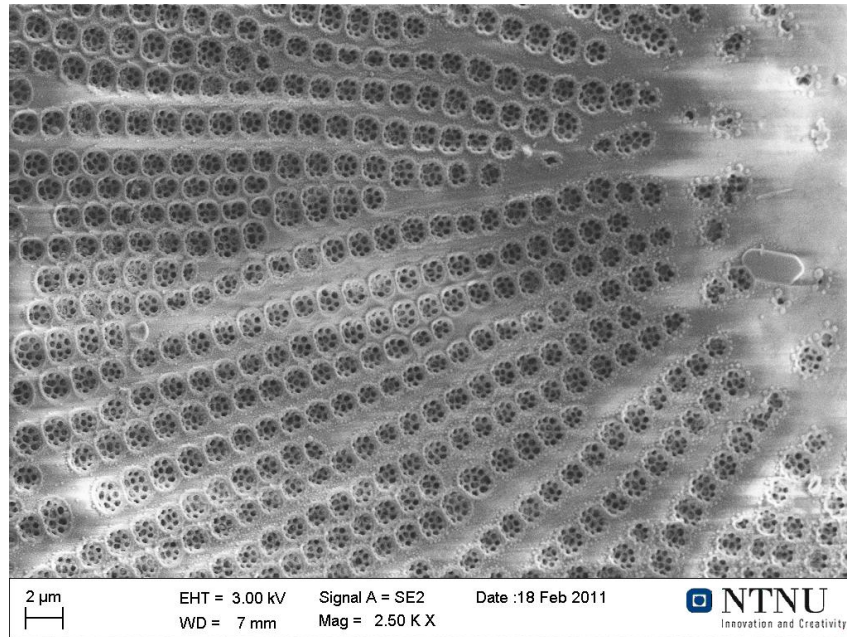
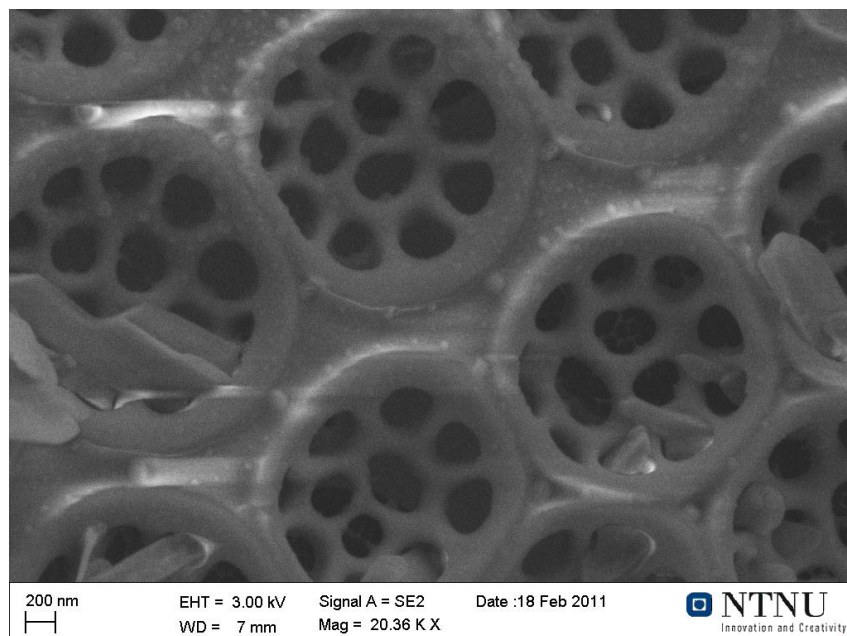Figure 11: Overall pore pattern of *C. wailesii*
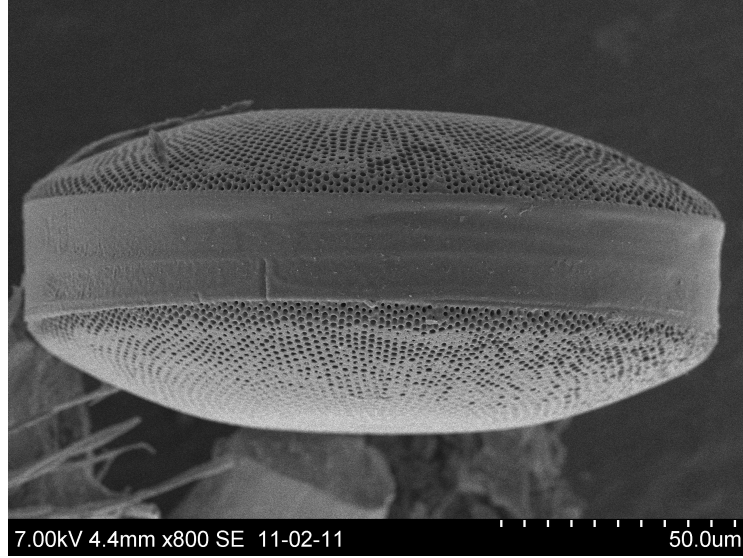

Figure 12: Areolae in *C. wailesii*

Figure 13: Overall structure of *C. sp.*in girdleview with epivalve, hypovalve and girdleband. This SEM image is acquired by Anita Fossdal.

very well maintained, and only small irregularities was found in places where a new row of pores begin (see figure 14).

The most important difference between *C.sp.* and *C. wailesii* is seen in the more complex three-dimensional structure of *C.sp.*. *C. sp.* is found to have loculate areolae, as seen in figure 15. This means that the perforations in the valve, the areolae, are enclosed by an inner and an outer siliceous layer. In the case of *C. sp.*, the areola is shaped as a hexagonal cylinder (see figure 16). The outermost siliceous layer, the cribrum (on top of the hexagonal cylinder), contains smaller pores named cribal pores. The cribal pores are found to be around 0.7±0.2 μm in diameter. These pores are covered by a thin perforated siliceous, plate termed cribellum (see figure 17). The cribellum have a fine mesh of pores with sizes of around 100 nm. The thickness of the cribrum and cribellum together is around 50 nm. Since it is so thin, it is also difficult to measure the exact thickness. The innermost layer (bottom of the hexagonal cylinders), which sits just opposite to the cribellum, is perforated by pores named foramen. The foramen are located at the centre of the base of the areola and the radius have two separate size distributions. The average of all measured values from both distributions are 342±184 nm. The girdle bands of *C.sp.* have a pattern of monosized pores that form an almost perfectly ordered hexagonal pattern. With a size of 95±5 nm, these pores are much smaller than the pores in the valve.
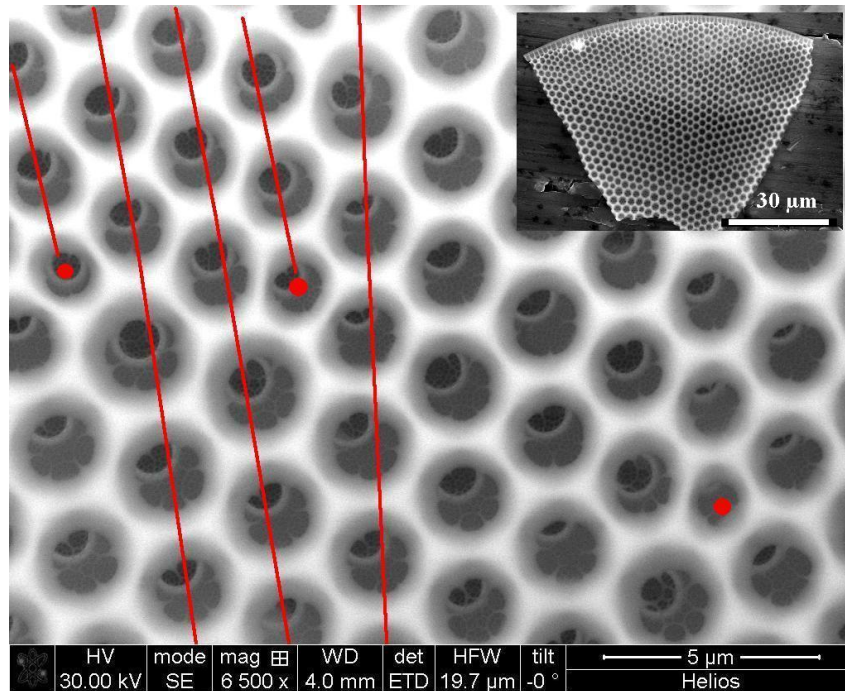
Figure 14: Overall areolae pattern showing how the hexagonal pattern is maintained by inserted rows of areolae. Input image with lower magnification show a part of a destroyed *C. sp* valve.
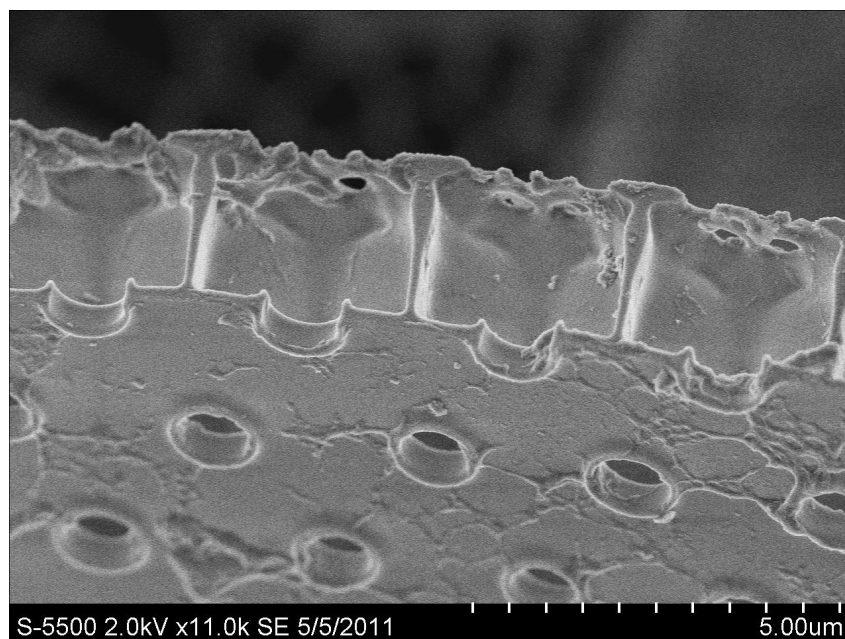

Figure 15: Cross section of the loculate areolae. Inner layer with foramen (below) and outer layer with cribal pores (above).
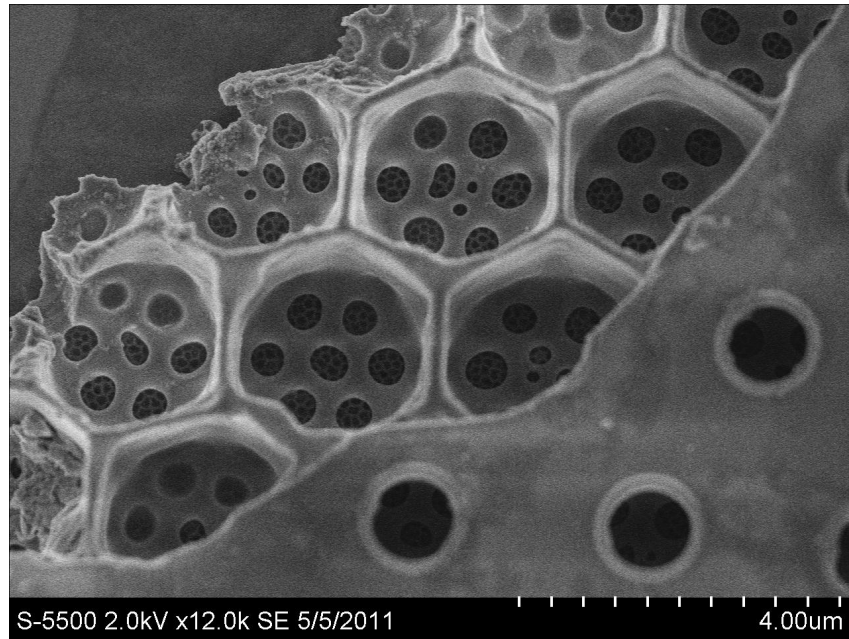
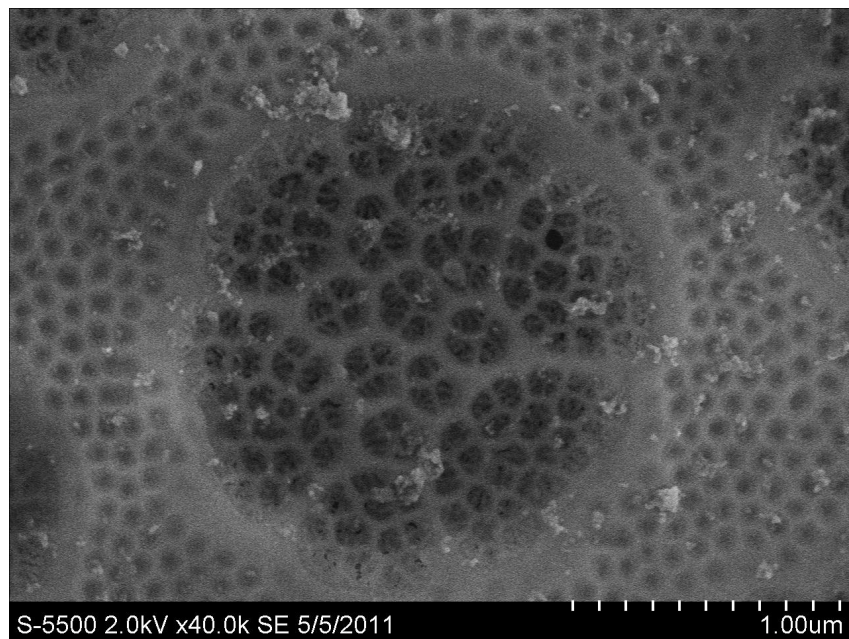Figure 16: Partly destroyed diatom revealing the areola and cribal pores beneath the foramen layer.
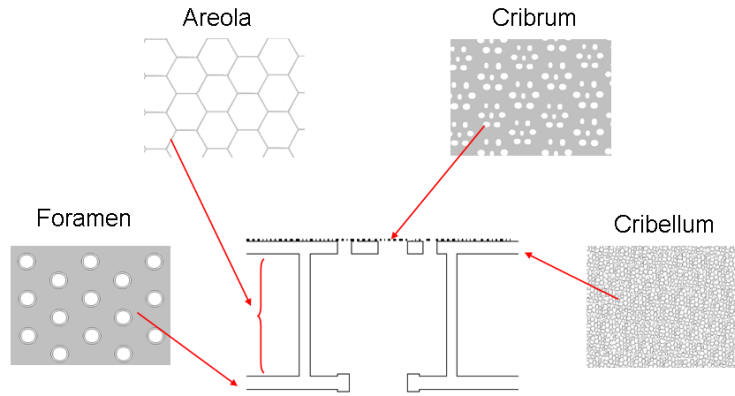

Figure 17: Cribrum, the outermost silica layer.

Figure 18: Schematic cross section view with the four distinct layers, cribellum, cribrum, areolae and foramen.
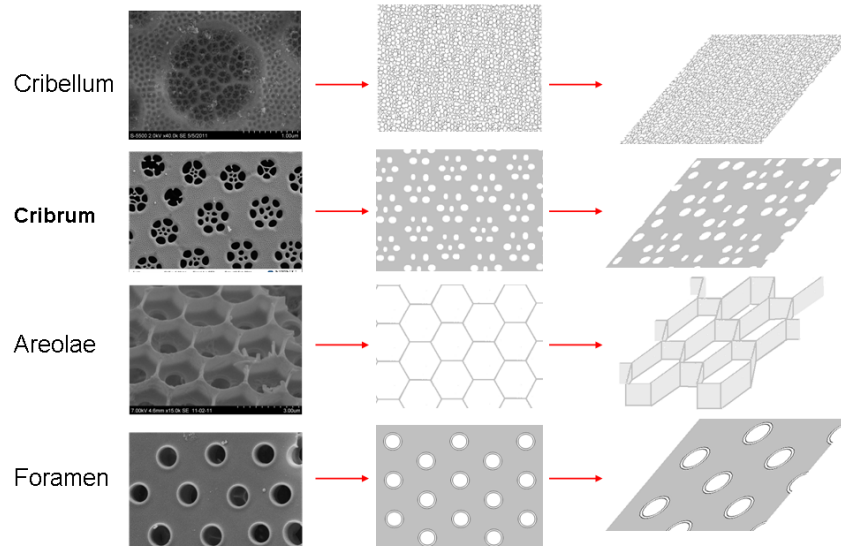
Figure 19: Relation between real diatom structure and the schematic model. The image of cribellum has a higher magnification than the three other images.
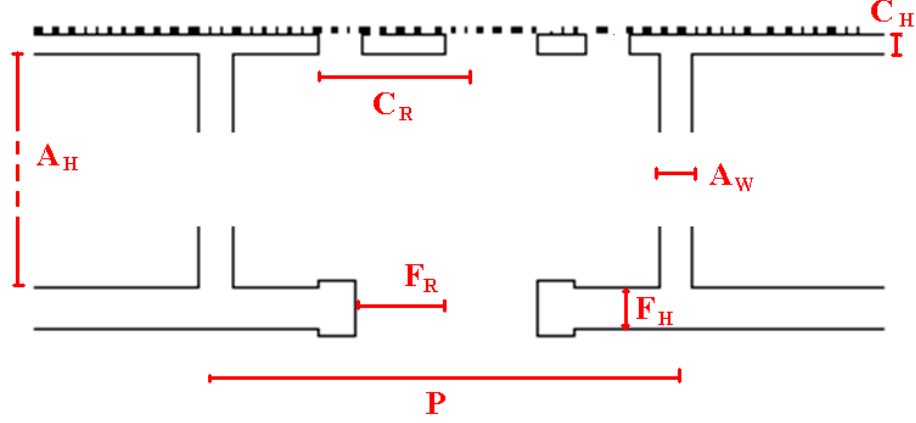
Figure 20: Illustration of the seven different structure parameters

Value of structure parameters of *C.sp.*(nm)						
	Radius foramen (F_R)	Height foramen (F_H)	Periode (P)	Wall thickness (A_W)	Height areola (A_H)	Height cribrum (C_H)	Radius Cribrum (C_R)
Average	342	97	1840	135	2390	50	360
Std. dev.	184	30	350	13	111	10	54

Table 1: Result of structural measurements on *C.sp.*. Between 15 and 50 measurements are done on each of the parameter. Tables are included in appendix B.

4.3   Schematic model

Based on the results from SEM imaging, simplified sketches were drawn in order to describe the microstructure. Figure 18 shows a cross section of the valve. Each of the four distinct layers - the foramen, areola, cribrum and cribellum - is illustrated in the sketch in figure 19. SEM images are included to show the relation between the sketched layers and the actual silica layers of the diatoms. Seven different structural parameters were defined in order to describe the structure (see figure 20). Table 1 summarizes the measurements made of the structural parameters of *C. sp.*. These values were the starting point for the modeling in GD-Calc.

5 Method - Diffraction calculations

The Matlab-based simulation software GD-Calc was utilized to create a model of the structure and to carry out the diffraction calculations. A description of the software and its theoretical background is given here. This part also includes information on how the source code was adapted to this project and how it was tested in order to evaluate whether or not the results could be trusted. The grating setup for each of the simulations is presented together with the assumptions and different parameter values used in each of the simulations. The last section contains a description of how the new algorithm was tested in order to evaluate whether or not the results could be trusted.

5.1 Gd-Calc software

GD-Calc (Grating diffraction calculator) is an electromagnetic simulation software based on a MATLAB function (gdc.m). This function can be incorporated into other MATLAB functions or scripts. The algorithmic foundation is based on a generalized variant of rigorous coupled-wave analysis (RCWA), which is used for EM and optical analyses of planar diffraction gratings. This means that the method represents both the electromagnetic field and the optical permittivity at any particular height in the grating in terms of their Fourier series in two lateral grating coordinates, and a set of differential equations are developed that describes the propagation of the field's Fourier coefficients through the grating. Software based on the finite-difference time-domain (FDTD) could have also been utilized, but with FDTD there is no possibility for a straightforward analysis of the strength of each separate diffraction order. RCWA is also better suited when the model structure contains layers with large differences in thickness, which was found to be the case with the *Coscinodiscus* structures. Information about the software can be found on the webpage software.kjinnovation.com.

5.2 Rigorous coupled-wave analysis

The RCWA is a method used for computing the amount of diffraction caused by a given grating structure [20]. In the original formulation of RCWA theory, the propagation equations were numerically solved in order to determine a "transmission matrix". The matrix defined the field amplitudes (Fourier coefficients) at the top of each stratum as a linear function of the amplitudes at the bottom. Errors that grew exponentially were found when these matrices were multiplied to determine the composite transmission matrix. This problem

has been resolved by using an alternative "S-matrix" (scattering matrix) approach. This matrix represents each stratum in terms of a linear mapping that relates the outgoing field amplitudes to the incoming field amplitudes at both boundaries. The individual mappings (S matrices) for the strata are combined by means of a numerically stable "stacking" algorithm in order to determine the grating's composite S matrix. The S-matrix method resolved the numerical stability problem, but convergence with respect to the number of Fourier coefficients retained in the calculations was typically very slow. This problem has been resolved by using a "Fast Fourier Factorization" method. Gd-Calc uses both the S-matrix method and Fast Fourier Factorization as ways for optimizing computational performance. More details on RCWA and the numerical algorithms can be found in relevant literature [20] and in GD-Calc.pdf.

5.3   GD-Calc algorithm

As previously stated, GD-Calc is based on the Matlab function gdc.m. This section includes a description of the algorithm of this funtion. gdc.m uses information about the incident field, the number of retained diffraction orders, and description of a diffraction grating to calculate the the resulting transmitted and reflected electromagnetic field. The gdc.m function takes inc_field, order and grating as its input arguments. The output arguments are param_size, scat_field and inc_field. These arguments will be described in the following paragraphs.

The incident field is defined by parameters that specify the wavelength, polarization and direction of the incident electromagnetic wave. The electromagnetic field is defined in accordance with equation 1 in section 2.1.1. inc_field consists of several elements;

  * inc_field.wavelength

    inc_field.f2,f3

  * inc_field.f1

  * inc_field.s2,s3

  * inc_field.p1,p2,p3

f2 and f3 are the incident field's tangential spatial frequency vectors, while f1 is the grating normal spatial frequency (k-vector). f2 and f3 are dependent on the polar angle, θ, and the azimuthal angle, ϕ, of the incident light. Along with the wavelength, these three variables are defined in the inc_field input argument. s2 and s3 are the grating's tangential basis vectors for S-polarization. The

basis vectors for P-polarization are p1, p1 and p3. All of these variables are defined in the output argument inc_field.

Generally, the order indices range from minus infinity to plus infinity, but for computational applications only a finite number of orders are retained. The number of retained orders is defined by the variable m_max. As an example; with m_max equal to 1, the zero and the first orders are retained. The orders are described by the index combinations m_1 and m_2 as described in section 2.1.4. The accuracy of the calculation result increases with increasing number of retained orders.

The grating consists of one or more strata (see figure 21). These are layers that are bounded by upper and lower planes which are parallel to the grating substrate. The strata can be uniperiodic, biperiodic or homogenous. The homogeneous stratum is optically homogeneous and it is not characterized by any periods. A uniperiodic stratum is subdivided into a number of stripes and it is periodic in one dimension. The biperiodic stratum is periodic in two dimensions and the stripes are subdivided into blocks. The permittivity must be specified for each block in a biperiodic grating and for each stripe in a uniperiodic grating. More complicated grating geometries, such as round shapes, can be approximated with these block-partitioned structures. The grating is assumed to consist of isotropic, non-magnetic optical media. Therefore, its optical properties are fully characterized by the scalar, complex permittivity η (see theory section). The grating is characterized by two fundamental vector periods, each of which describes the permittivity function's translational symmetry characteristic. These vectors run parallel to the substrate. The permittivity of the superstrate (the volume located below the grating) and substrate (the volume above the grating) are independent and constant. When constructing the grating, only one unit cell is defined and the grating is a periodic repetition of this unit cell.

The output argument Scat_field contains all the information about the reflected and transmitted waves. Each element in scat_field(k) corresponds to one diffracted order.

* scat_field(k).m1, m2 diffraction order indices

  scat_field(k).f2, f3, field's grating-tangential spatial frequencies (components of the wave vector)

* scat_field(k).f1t, f1r reflected and transmitted field's grating-normal spatial frequencies (components of the wave vector)

* scat_field(k).s2, s3 grating-tangential basis vector for S polarization

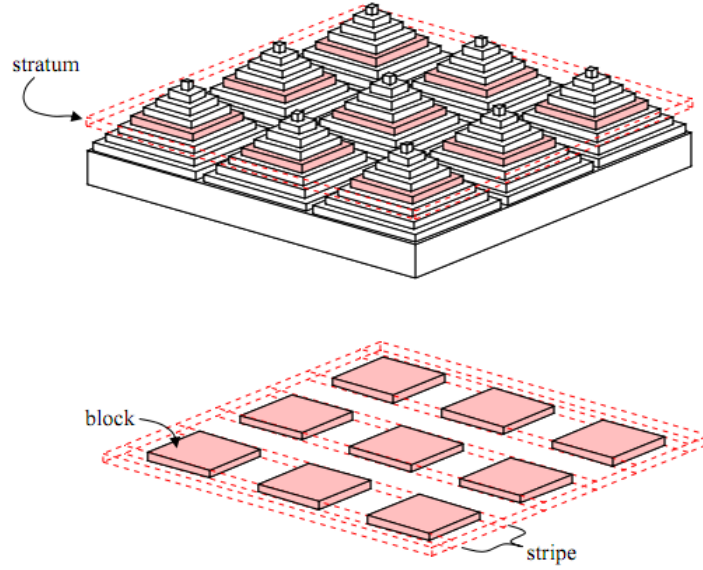* scat_field(k).p1t, p2t, p3t the three basis vectors for P polarization, for

Figure 21: Illustration of blocks, strips and strata in an example grating. Image from GD-Calc_Intro.pdf

> transmitted field

* scat_field(k).p1r, p2r, p3r basis vectors for P polarization, for reflected field

* scat_field(k).Tss, Tsp, Tps, Tpp transmission matrix, field transmitted from s-polarization to s- and p-polarization and p-polarization transmitted to s- and p-polarization.

* scat_field(k).Rss, Rsp, Rps, Rpp reflection matrix, same description as the transmission matrix.

The transmission and reflection matrices represent the diffracted electromagnetic field. The transmitted and reflected field consists of a superposition of plane-wave Fourier orders with spatially frequency vectors, which are labelled by two diffraction order indices m1 and m2. The transmittance and reflectance field are calculated at the interface between the grating and the substrate and superstrate. In order to transform these electromagnetic field values into diffraction efficiencies, the values for each of the two polarizations are summed and squared. Afterwards, the average value of both polarizations are multiplied with the term c, which is the ratio between the real value of the grating-normal spatial frequencies of the diffracted field and the incident field (scat_field.f1r(t)/inc_field.f1i). If the average values were not multiplied by c,

the obtained efficiency value would be dependent upon the photon flux through the cross section situated perpendicular to the wave direction. However, by definition the power should instead be described by the photon flux through the cross section that parallels the grating, hence the need to multiply by c. Since the amplitude of evanescent waves drops of exponentially as it penetrates a less dense medium, these values should not be retained in the calculations. They are removed by setting imaginary elements in the transmission and reflection matrix equal to zero. The operations described in this section are carried out in gdc_eff. The output diffraction efficiencies are the resultant values from this function.

5.4   Adaption of the algorithm

The algorithm utilized in simulations in this study was based on the source code from GD-Calc demos, which was further adapted to fit the needs of this study. Also, some new functions and scripts were established. The arithmetic operations were adjusted by adding ('.') to the arithmetic operations in the code order to perform calculations with matrices. This opens up for the possibility to define the wavelength and grating geometry parameters as vectors. The grating geometry parameters are parameters describing the structure of the grating, for instance the period. Definition of these variables as vectors enables simulation with, example given; different periods and wavelengths simultaneously. This leads to a scat_field matrix with dimensions a x b x c, where a is the length of the wavelength vector, b is the length of the grating geometry parameter vector and c is the number of orders. The advantage with this method is that it makes it possible to look at different sets of parameter combinations without doing numerous simulations. Below is a description of the algorithm in list form. The list is followed by a more detailed description of step 2, 5 and 7. All of the source code files are included in appendix D.

1. Definition of the wavelength vector, the angle of the incident light and the number of orders retained in the calculations. The script "gdc_ak_defineincidetfield" allocates values to the inc_field f2, f3 and wavelength

2. Get data for the refractive indexes by interpolation and calculation based on dispersion functions, function ar_wk_interp and ar_disp_lorenz.

3. Allocate refractive index values to the permittivity vector, grating.pmt

4. Define and allocate values to the grating geometry parameters that describe the grating.

5. Construct the grating with its different strata based on the given grating

geometry parameters and refractive indexes from the permittivity vector. (Construct_grating).

6. Run the diffraction calculations (gdc.m).

7. Run calculations to obtain diffraction efficiencies (gdc_ak_eff).

8. Plot and save graphs.

5.4.1   Algorithm step 2

The wavelength-dependent refractive index data was obtained through two different methods. First, interpolation was used to construct new refractive index data points within the range of a discrete set of known refractive indices. The set of known refractive indices that was found in the literature. The other method used dispersion constants and equation 2 in section 2.1.2 to calculate refractive index data for given wavelengths. These data are given in section 5.6.

5.4.2   Algorithm step 5

The grating was created to represent a simplified diatom model of the valve structure of *C. sp.*. It was constructed based on the information from the structure characterization. The grating comprised three different strata, where the first and third are simply variants of the same stratum. The first stratum was based on GD-Calc demo 5. The details can be found in GD-Calc_demo.pdf. This stratum represented a layer consisting of homogeneous material perforated by hexagonally-ordered pores. This stratum resembled the inner silica layer with the foramen holes. The grating geometry parameters of this stratum were the radius of the pores and the height of the stratum. The second stratum was a imitation of the areola (honeycomb pattern). As seen in figure 23, the unit cell comprises a part of a hexagonal cylinder. This stratum consists of four groups of stripes, the vertical wall two sloping walls and two triangles connecting these walls. The thickness of the walls and the height of the stratum were varied. With the exception of the thickness and the radius of the pores, the third stratum is equal to stratum number one. It is supposed to resemble the cribrum layer. The height of this stratum is kept constant. Since this layer was found to be so thin, the structure of this layer does not significantly affect the diffraction. The pores in the upper layer consist of many smaller pores and can, therefore, be approximated by finding the average refractive index. It is estimated to be 80% air and 20% silica in the cribellum pattern. The radius of this air/silica pore has the ratio 0.4
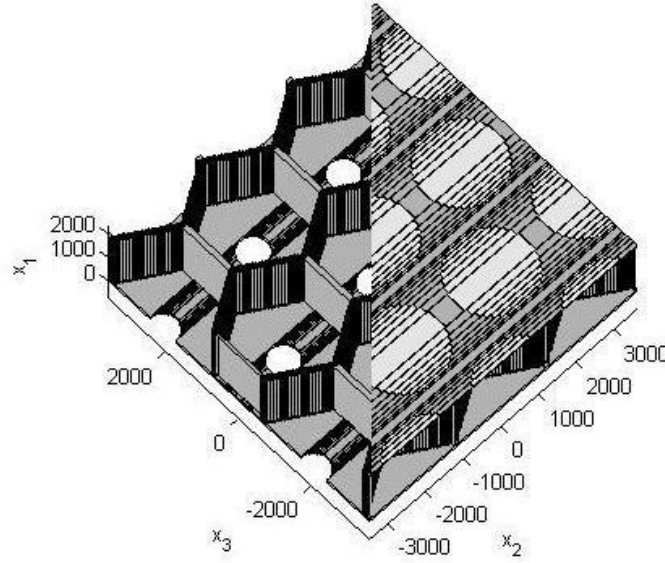
Figure 22: All three strata in the grating. Foramen layer at the bottom (stratum 1), areola in between (stratum 2) and cribrum at the top (stratum 3). The black stripes seen in the structure is only the borderlines between adjacent stripes and blocks. These stripes has no physical impact on the model.

to the periodicity of the grating, so the cribellum is made to scale with the periodicity. The periodicity is common for the entire grating and this was the last grating geometry parameter that was varied in the simulations. The grating geometry parameter vector and the vectors of the angles θ and ϕ must have the same dimension.

5.4.3   Algorithm step 7

gdc_ak_eff.m creates the outputs efficiencies that enable an evaluation of transmission and reflection. The algorithm converts the electromagnetic field values into diffraction efficiencies. The different values obtained are:

* T_eff_sum_m is the sum of the transmitted light to all orders

  T_eff_00_m is the zero order diffraction for transmitted ligth

* T_eff_01sum_m is the sum of transmitted light diffracted to the first orders

* T_eff_m is the sum of all orders averaged over the wavelengths
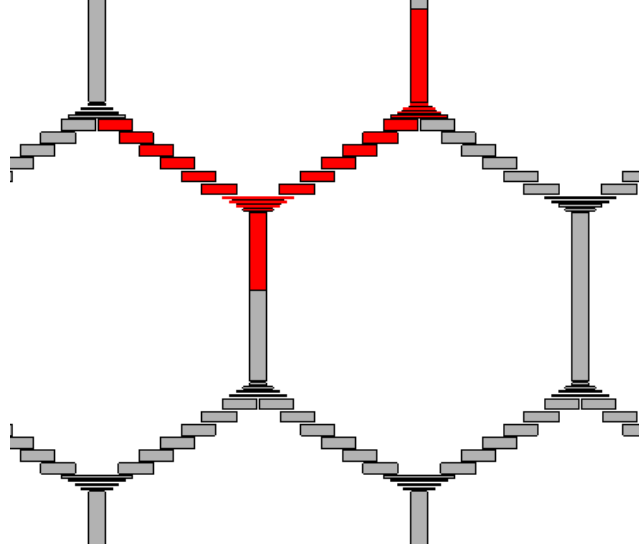
Figure 23: Model of hexagonal structure, stratum 3. Illustration of the four stripe regimes; the vertical wall, the sloping wall and the to triangles connecting these walls. A higher number of stripes give a more accurate model.

* T_eff_ave_01 is the sum of firstorders and the average of the wavelengths

The same values are calculated for the reflection. The matrix elements that comprise complex electromagnetic field values (evanescent field) are removed in this function.

5.5   Simulation setups

Three different types of grating setups were investigated in this study (see figure 9). The first setup employed all three strata in the grating, hence resembling the diatom valve structure. The superstrate and the substrate were both fixed as air with a refractive index of 1. In the simulations, the five different grating geometry parameters were varied in order to see if and how the optical properties were altered by changes in the structure. While varying one parameter, the default values were used for the other parameters. The values are listed in table 2 and they are based on the result from measurements of the frustule structure (see table 1). The middle value is the default value in the simulations.

In the setup that emulated a solar cell, only the first stratum - i.e. the foramen layer - was used. The reason for this choice was to avoid introducing too many variables and because this layer closely resembles the optically active layers

Grating geometry parameters					
Nr.	Radius foramen (nm)	Height foramen (nm)	Periode (nm)	Wall thickness (nm)	Height of areola (nm)
1	0	0	1000	10	0
2	100	20	1700	70	1200
3	**350**	**100**	**2400**	**135**	**1800**
4	500	300	3600	150	2400
5	1000	500	4200	180	300

Table 2: The five values for the grating geometry parameter. The choice of the bold default values was based on the measured values.

which are typically found in solar cells. The grating was included in two different solar cell setups. First, it was sandwiched between a substrate of amorphous silicon and a superstrate of air. The material inside the diatom's pores was varied, switching between air, amorphous silicon (aSi), and silicon nitrate (Si_3N_4). In the second setup, the grating was placed between an aluminium (Al) substrate and an aSi superstrate. The values in the first three rows of the grating geometry table 2 were used. The two last rows were not relevant in this case since the grating did not contain the areola layer.The height of cribrum was kept constant and the radius of the cribrum scaled as 40% of the periode.

5.6   Assumptions and data

Normally-incident unpolarized light was assumed in all simulations. The wavelength ranged from 400 nm to 1000 nm and was varied with step sizes of 20 nm. Wavelength-dependent refractive index data was obtained by two different methods: interpolation and calculations based on the dispersion equation (see figure 3) and constants. Refractive index values for aSi and Al were found by interpolation. The original values were taken from an ellipsometry database and the SOPRA database. Values for Si_3N_4 were found by interpolation. The dispersion constants were also gathered from the ellipsometry database. Aside from the a-Si in the substrate and superstrate, the complex index of refraction was used for all materials. Since the values for the complex electromagnetic field (evanescent field) are removed from the transmission matrix, all reflection values would also be set to be zero with the use of a complex refractive index. For this reason, only the real part of the refractive index of amorphous silicon is used.

(a)   (b)

(c)
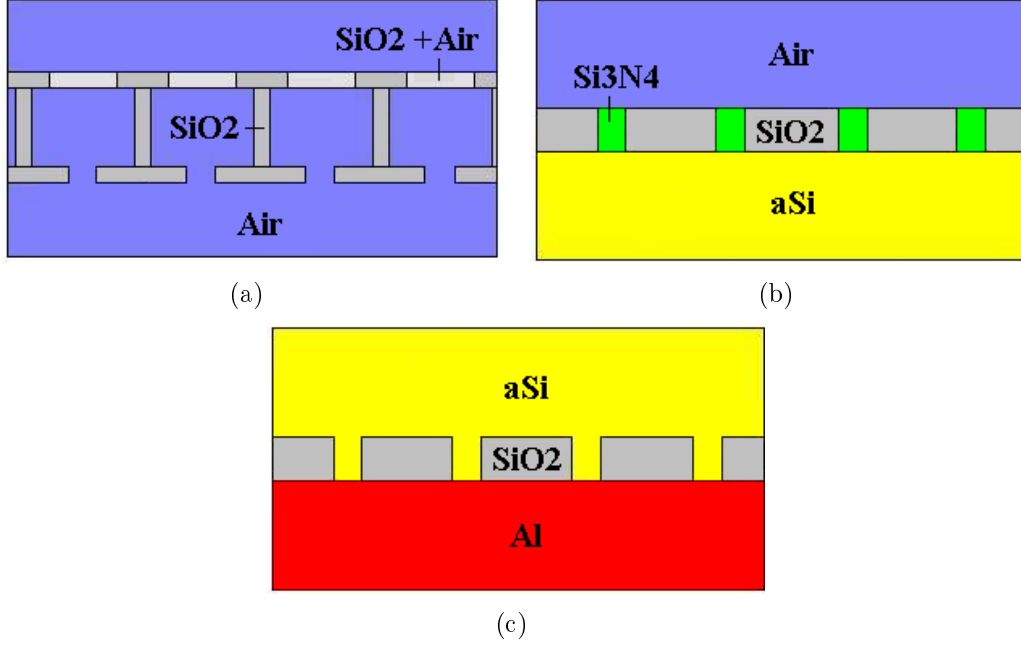
Figure 24:
Diffraction grating setup for the simulations (a) Grating emulating the
diatom valve structure, (b) Anti-reflection structure. (c) Back-side diffraction
grating. For (b) and (c) only the foramen layer was included.

Dispersion constants				
	ϵ_{fin}	ϵ_s	ω_t	γ_0
SiO$_2$	5.377	3.186	1.787	1
Si_3N_4	4	9	0.1	1

Table 3: Dispersion constants for SiO$_2$ and Si_3N_4 obtained from deltapsi2
ellipsometry software
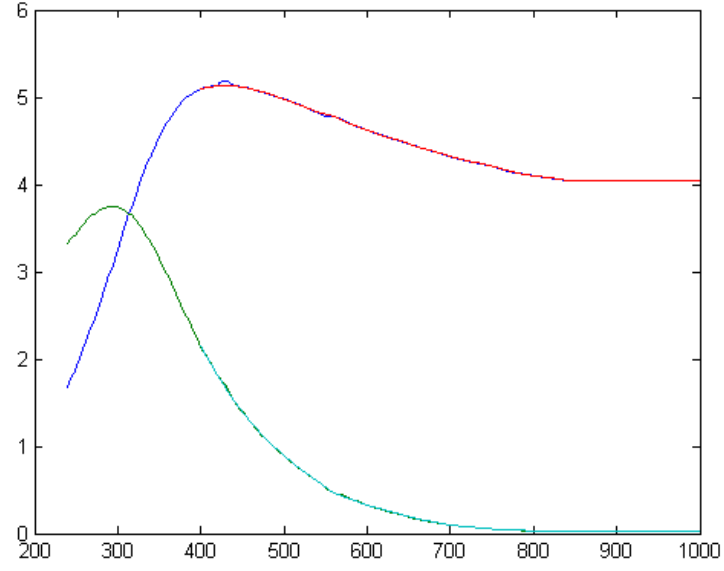
Figure 25: Real and imaginary part of the refractive index of aSi. Only the real part used in the calculations
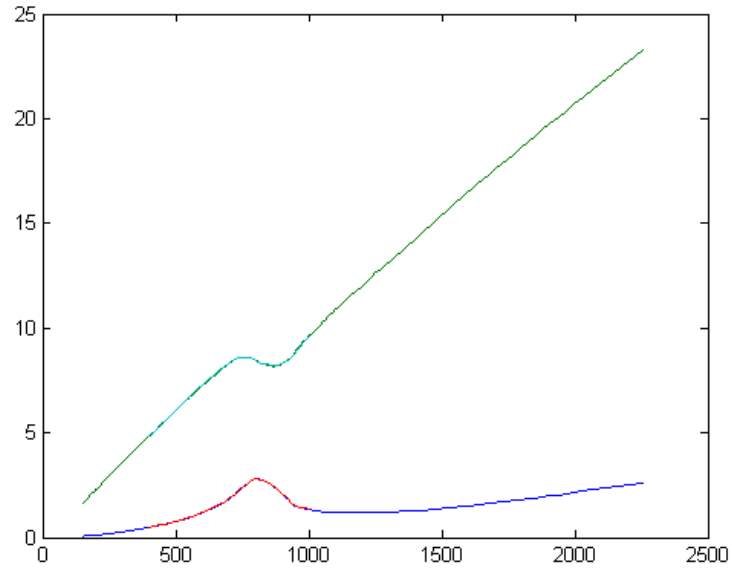
Figure 26: Real and imaginary part of the refractive index of Al

Parameters in the simulations	
Angle of incident light	0
Wavelength steps	20
M_max	5
Stripes in the vertical wall	1
Stripes in the sloping wall	16
Stripes in the triangles	8
Partition blocks in the foramen	8

Table 4: The standard settings utilized in the simulations

5.7   Number of stripes and orders

The number of stripes, wavelengths and orders that were retained in the calculations were found by a test simulation containing a single set of structural parameters. The number of stripes was chosen with the focus on constructing an accurate model of the diatom structure. The number of orders was determined with an eye for striking a balance between achieving exact simulation results versus being able to run the simulation within a reasonable time frame. A certain number of the wavelengths had to be used in order to resolve the wavelength and the changes in the diffraction efficiencies. The test simulations were done with the m_max equal to 3, 6 and 9. For each value of m_max, the number of stripes was varied between one and five. The wavelength step sizes were varied between 200, 50 and 20. Graphs showing transmission efficiencies with m_max equal to 3 and to 9 are displayed in figure 27(a) and 27(b). It can be seen that the results change from figure 27(a) to figure 27(b). Therefore, it can be concluded that three orders are not sufficient for obtaining an accurate result. In the simulations m_max = 5 was used due to a lack of computer memory and to time limitations. The number of wavelengths needed in order to get a good result is dependent on the type of grating being investigated. Grating that consists of several layers needs a larger resolution due to the larger number of terms in the Fourier series. In this study, the wavelengths are varied with a step size of 20 nm. The simulation result was found to be accurate and stable, with few stripes in the stratum. This can also be seen in the graphs. The parameter settings used in the simulations are summarized in table 4

These test simulations demonstrated that the number of orders retained was of greater importance when compared to the number of stripes. In other words, there is no use in increasing the number of stripes without increasing the number of orders.

(a)

(b)
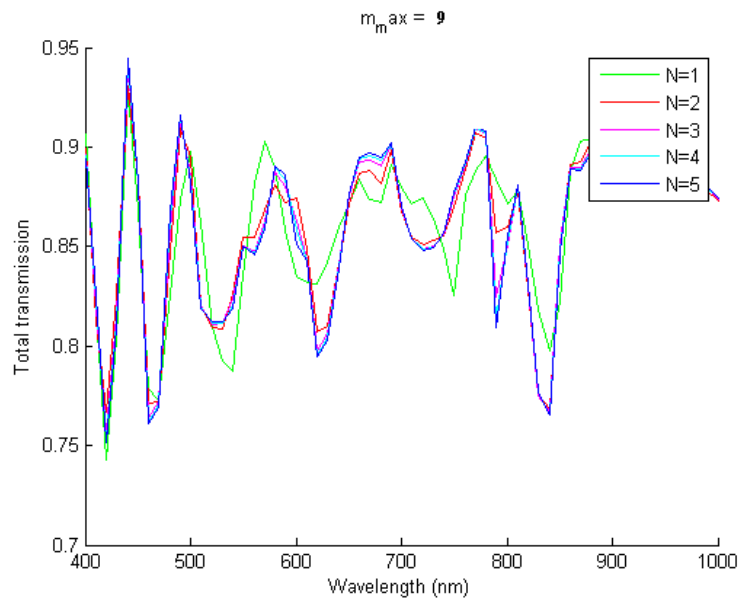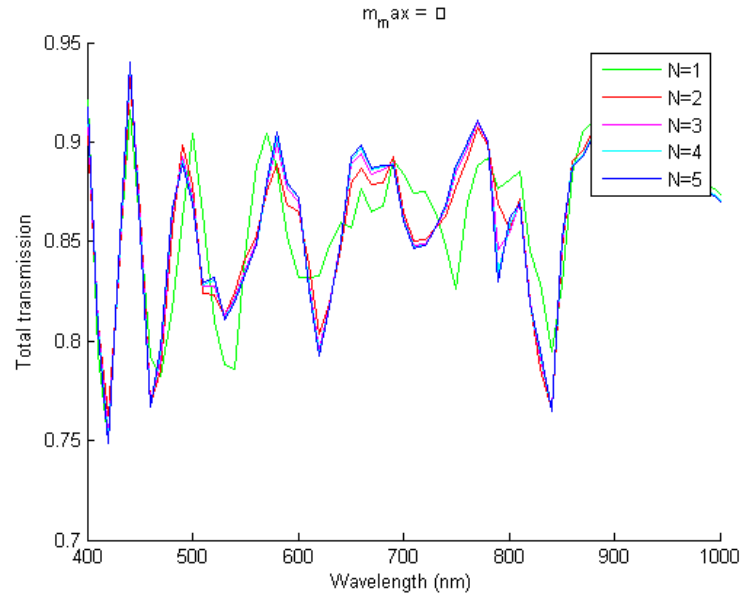
Figure 27: Test of number of stripes and orders retained (a) m_max=3 (b) M_max=9

5.8   Verification

To verify whether the algorithm produce trustworthy results or not, a test was carried out comparing simulated reflection values to reflection found through equation 5. The test was carried out on a layer of homogeneous material in air. The foramen radius was set close to zero, thus approximating a homogeneous stratum. The substrate was air, while the refractive index of the material in the stratum was set to equal the refractive index of aluminium and amorphous silica used in the calculations. Both approaches gave the value of 0.0359 for silica and 0.42 for amorphous silicon. Since the values were found to coincide, it is assumed that this algorithm can be trusted.

6 Result - Diffraction calculations

The results from calculating diffraction within the full grating structure in an air surrounding and in the solar cell setups are presented in this section. In the presentation of the results, the efficiencies are described with numbers ranging between 0 and 1, although one could just as adequately describe the efficiencies as a percentage. In this case, the efficiencies of 1 correspond to 100%. Those graphs that reveal the most interesting results are included in this section, while the remaining results can be found in appendix C. The plots show values for transmission efficiency (TE) and reflection efficiency (RE) among the different grating setups. There are five types of graphs. Graphs with the title "all" are plots of T_eff_sum_m, which show the sum of the TE or the RE for all diffraction orders as a function of wavelength. The graphs termed "first order" describe how the first-order diffraction (T_eff_01sum) changes as the wavelength changes. A plot of the transmission to the zero order, T_eff_00_m, was also done, as shown by the graphs marked as "zero order". The plots with the name "average" show the total diffraction (R_eff_ave_m) and the first-order diffraction (R_eff_ave_01) averaged over the wavelengths for all five values of the grating's geometric parameters. The integers on the x axis of these graphs correspond with the grating's geometric parameter numbers listed in the table 2. For example, x=2 for the radius graph corresponds to a radius of 100 nm. These graphs describe how the diffraction efficiencies vary with changes in the geometry. A few plots, such as those like figure 28, are also made for displaying efficiency information for all of the parameters. In all of the plots where the wavelength appears on the x-axis, the red curve represents the default parameters.

6.1 Grating in air

Diffraction simulations were first performed on the grating by using air as the superstrate and substrate. This was done in order to obtain a better understanding of the optical properties of the diatom's structure and to investigate how variation of the different geometries would affect the diffraction. The calculations were performed with five different values for each of the grating's geometric parameters. Since silica has a low refractive index, it will not function as an efficient reflector material, a conclusion that strongly coincides with the simulation results. For this reason, only the most interesting transmission graphs are present here. Figure 28 and figure 29 show how variations in the grating's geometric parameters affect the total efficiency and the zero-order efficiency, both of which are averaged over the wavelength. As shown by 28, the TE lies around 0.88 for all wall thickness, period and
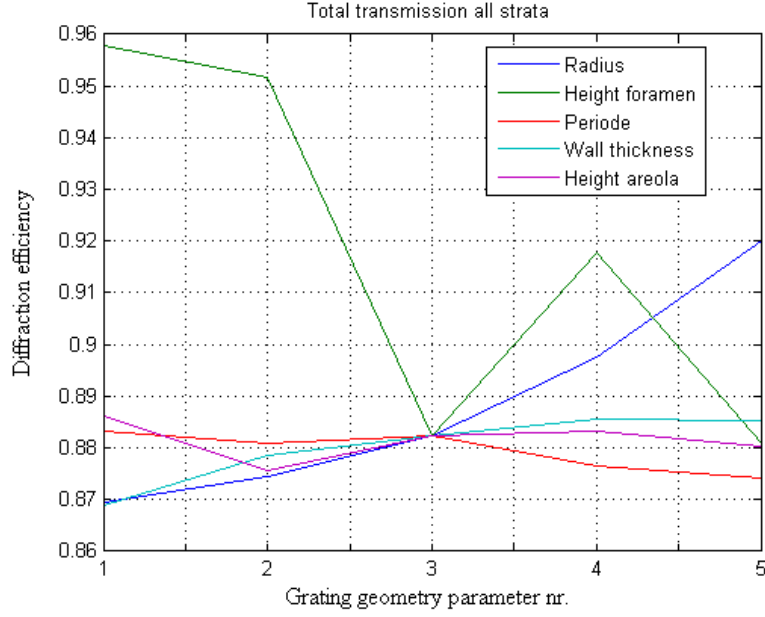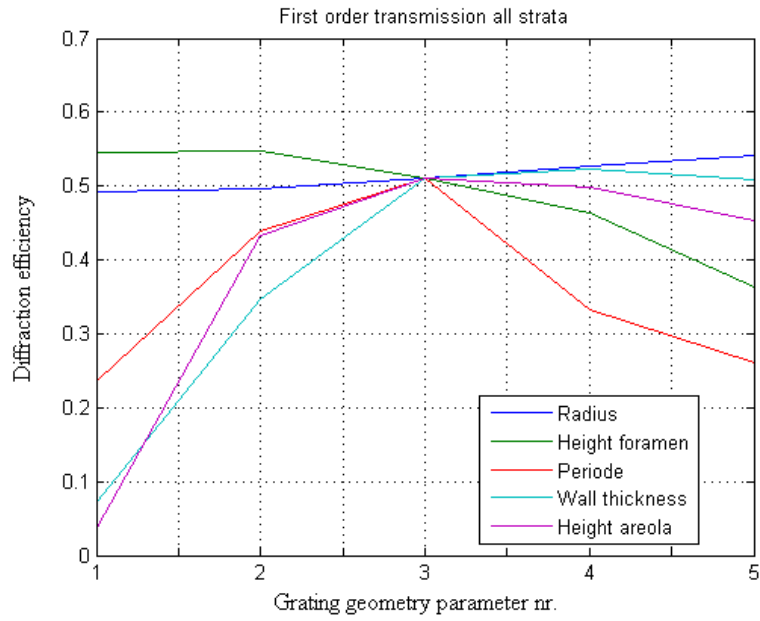
Figure 28: Total TE for all of the grating geometry parameters. The values are summed over all orders and averaged over the number of wavelengths.

areola height values. The TE is found to be dependent to a larger extent of the height and radius of the foramen. The first-order transmission efficiencies are found to change with all five of the grating's geometric parameters (see figure 29). The following sections describe in greater detail the effects of variations in geometric parameters of the grating.

6.1.1 Radius foramen

The diffraction calculation was run for five values of the foramen radius: 0, 100, 350, 500, 1000 nm. From figure 28 it can be seen that a larger radius gives a higher total TE, from 0.87 with $F-R$ equal to 0 nm, to 0.92 for R_F equal to 1000 nm (see figure 28). The total TE does not have strong wavelength dependencies. Almost all of the values were found to be between 0.85 and 0.95 (see appendix figure 62(g)). However, this was found to be the case for the first-order TE, which exhibits a broad maximum for wavelengths between 500 and 1000 nm (see figure 30). The first-order TE value is above 0.4 for all wavelengths larger than 500 nm. According to 31, the zero-order TE falls below 0.1 between 500 and 750 nm. With wavelengths close to 600 nm, the efficiency is zero. The first-order TE exhibits the same increase in efficiency as the total TE.

Figure 29: First order TE for all grating geometry parameters. The values are summed over the first order TE and averaged over the number of wavelengths.
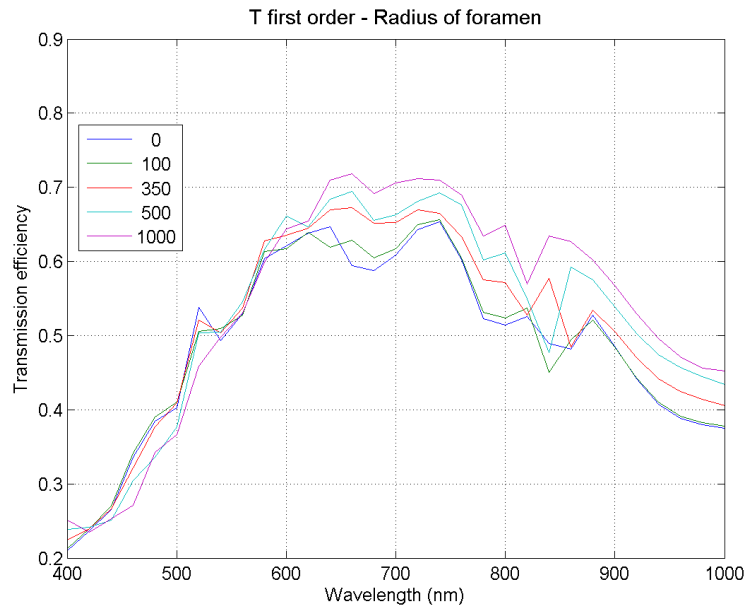
Figure 30: First order TE spectra for five different radius values in the full grating setup
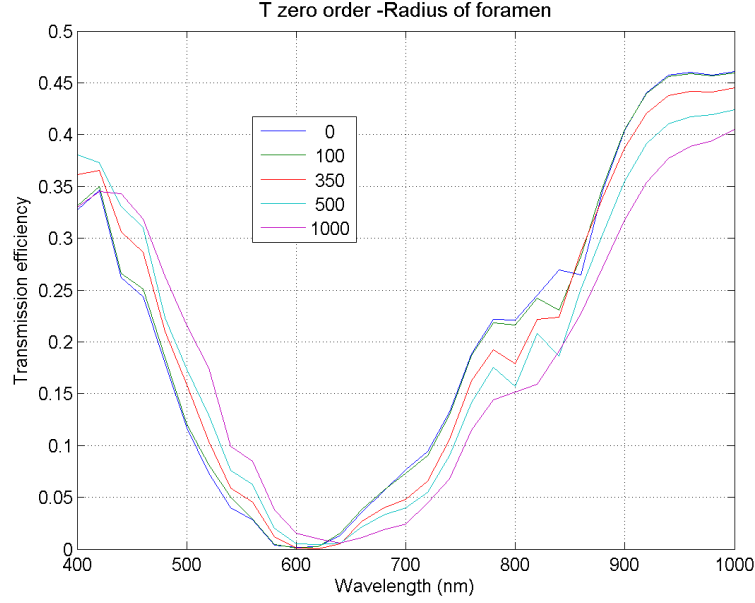
Figure 31: Zero order TE spectra for five different radius values in the full grating setup

6.1.2   Height foramen

Simulations were performed for height values of 0, 20, 100, 200 and 500 nm for the foramen layer. The results showed that the total TE through the grating varied between 0.88 and 0.96 (see 32). The wavelength dependency of the total TE was not large (See figure 62(k) in appendix). The broad peak of first-order transmitted light is the same as the one seen when the radius varies. However, it can be seen that the peak is somewhat lower and shifted to the left when layer thickness is increased (33). The first-order transmission values are highest for zero thickness.

6.1.3   Period

The period took the values 1000, 1700, 2400, 3600 and 4200 nm. Changing the period did not significantly alter the total TE value. It is also found to be mostly independent of the wavelength, except for a minimum variation at wavelengths of 900 nm for periods of 1000 and 1700nm (see appendix C). The first-order scattering is largest for the middle period values (1700, 2400, 3600 nm). The default value gives the highest first-order transmission, both for the average value and for the long wavelength segment of the spectra.
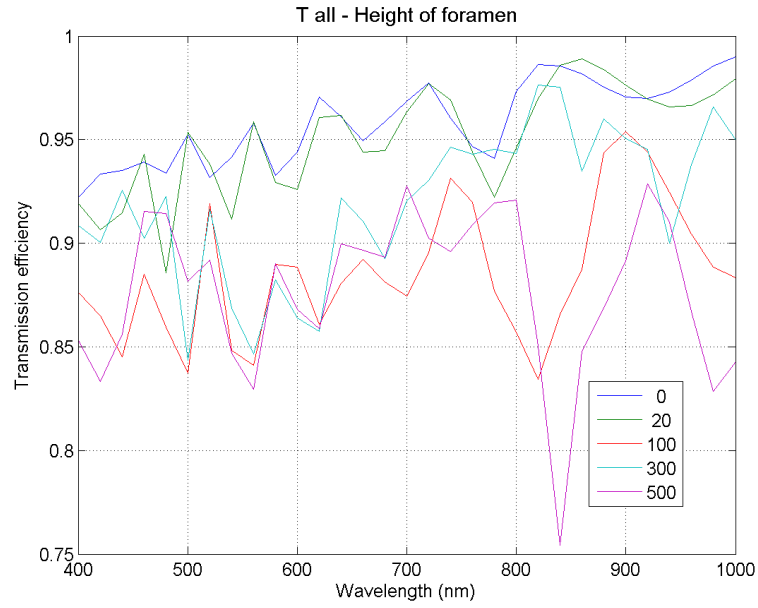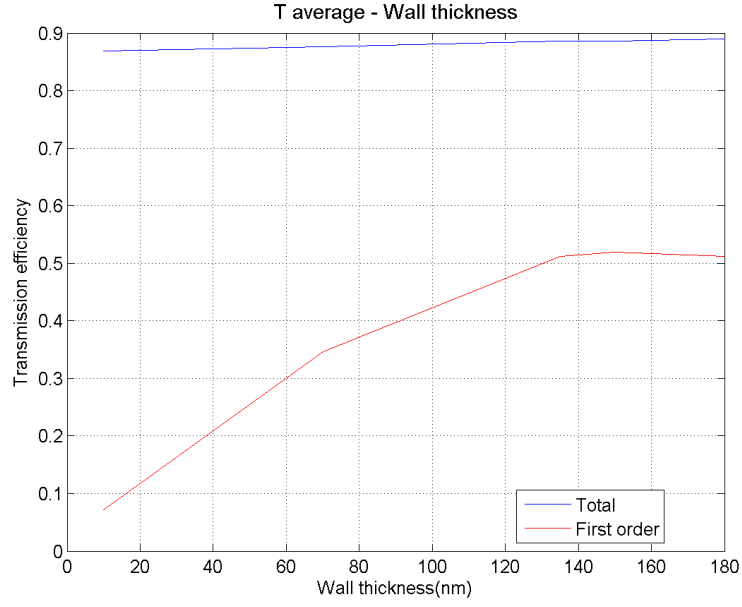
Figure 32: Total and first order TE spectra averaged over wavelength for five different values of the height in the full grating setup.
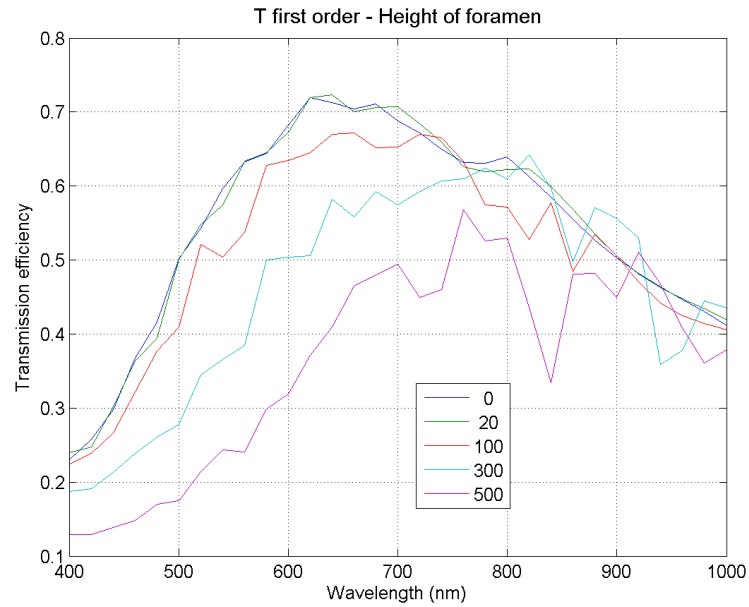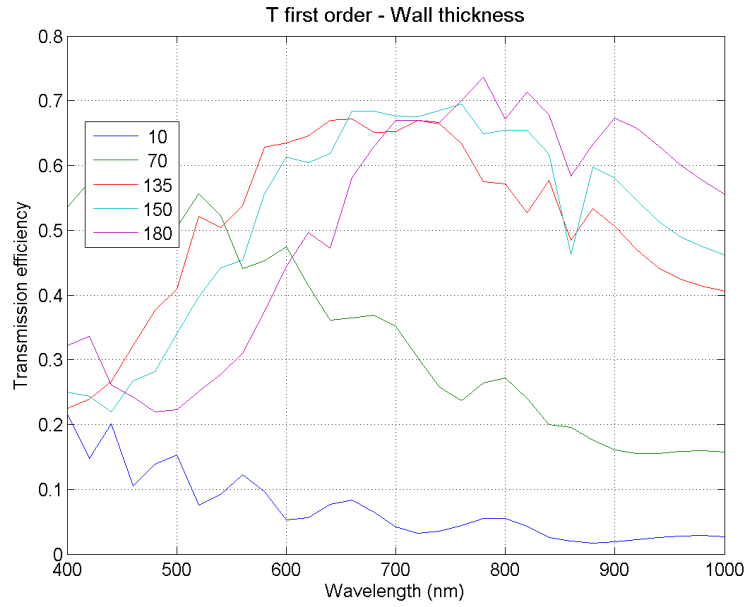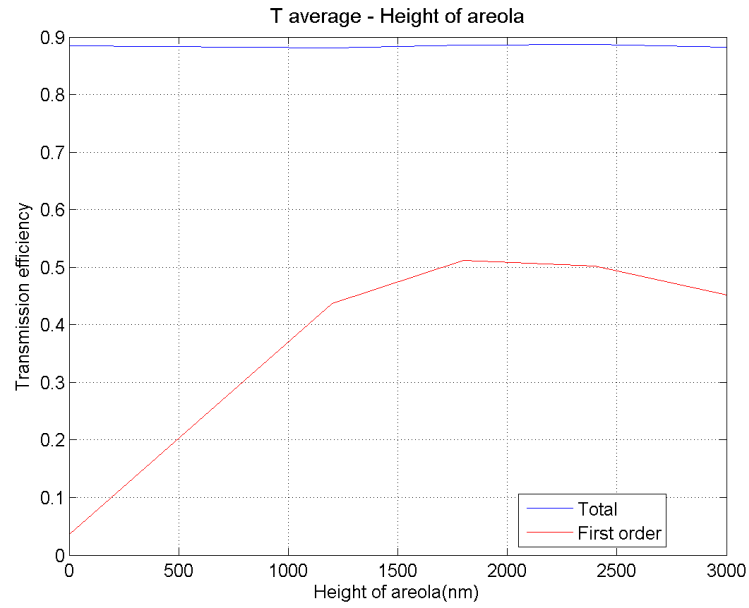

Figure 33: First order TE spectra for five different values of the height in the full grating setup
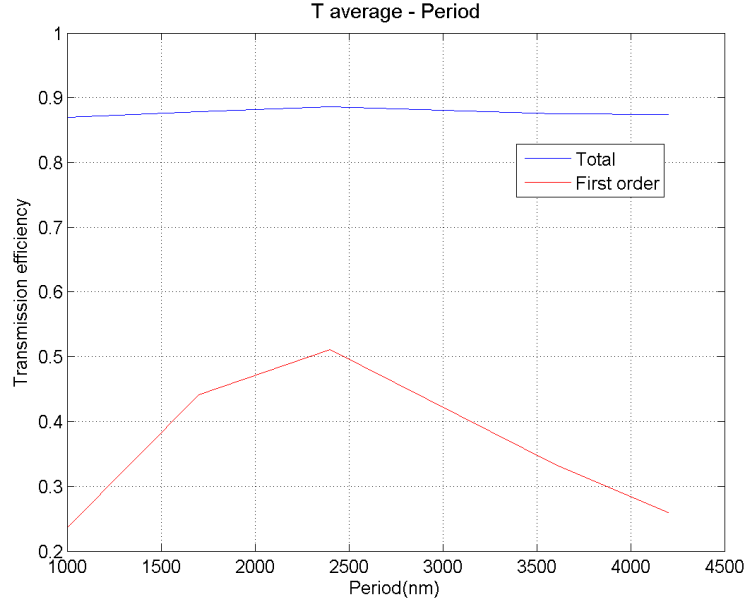
Figure 34: Total and first order TE spectra averaged over wavelength for five different values of the period in the full grating setup.
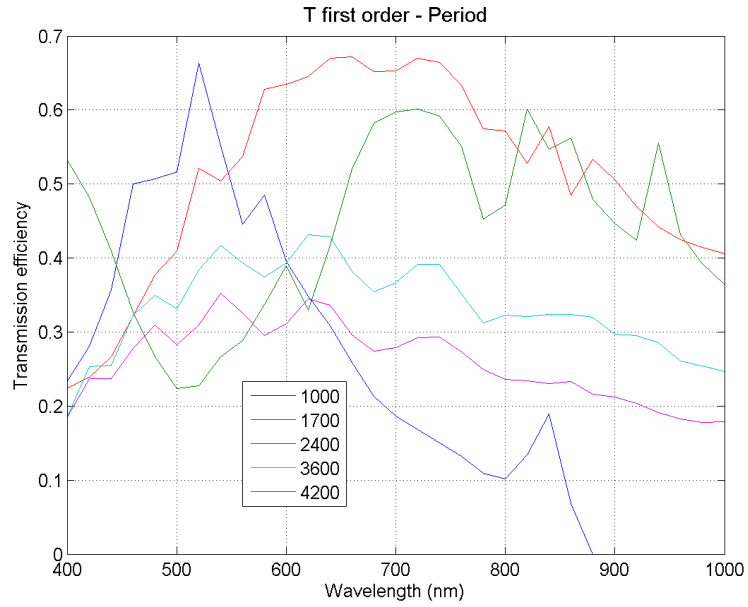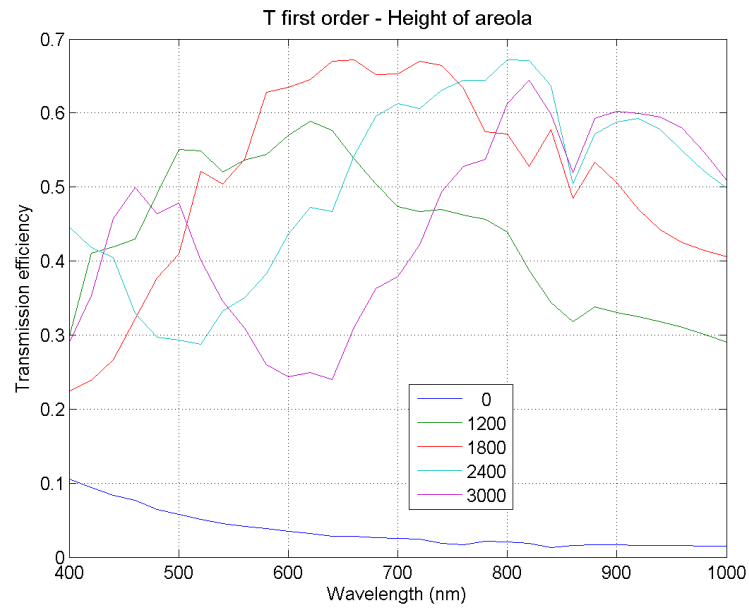

Figure 35: First order TE spectra for five different values of period in the full grating setup

6.1.4 Thickness wall areola

The wall thicknesses used in the calculation was 10, 70, 135, 150 and 180 nm. The total TE was found to be largely independent of the wall thickness. Only a slight increase in the TE was found at the thickest level (see figure 36). The first-order transmission was found to be significantly dependent on the wall thickness. As shown in figure 37, the broad first-order transmission peak disappears when the thickness of the wall is less than 70 nm. Instead, the transmission becomes more pronounced for shorter wavelengths. The broad peak is shifted a bit to the right with thicker walls.

6.1.5 Height areola

The height of the areola was varied between 0, 1200, 1800, 2400 and 3000 nm. The total TE was independent of height variations (see figure 38). As figure 39 demonstrates, the broad first-order diffraction is most pronounced for areola heights that equal 1800 nm, as was seen in 29. This was the default value of the height, and the spectrum corresponding to this height can be seen in the previous figures. If only considering long wavelengths, the first-order TE is a bit higher for heights that equal 2400 nm.

6.1.6 Summary and comparison of measured and "ideal" values

The simulations found that the total and first-order reflections were low, with a total RE below 0.12 for all values. The transmission was around 0.9 and was affected mostly by the height and radius of the foramen. The highest first-order transmission value was found where the foramen height was low and the foramen radius was large, where wall thickness was wide, and where the default values for the period and areolae were 2400 and 1800 nm respectively. Figure 40 and 5 compare the "ideal" structure with the values from structural measurements in SEM.

Structure parameter values (nm)					
	Radius foramen (F_R)	Height foramen (F_H)	Period (P)	Wall thickness (A_W)	Height areola (A_H)
Measured	342	97	1809	135	2390
Ideal	1000	0	1800	180	2400

Table 5: Measured diatom structural values and "ideal" grating geometry values.

Figure 36: Total and first order TE spectra averaged over wavelength for five different values of the wall thickness in the full grating setup.

Figure 37: First order TE spectra for five different values of wall thickness in the full grating setup. Legend unit is nm.

Figure 38: Total and first order TE spectra averaged over wavelength for five different values of the height of the areola in the full grating setup. Legend unit is nm.

Figure 39: First order TE spectra for five different values of height of areola in the full grating setup. Legend unit is nm.
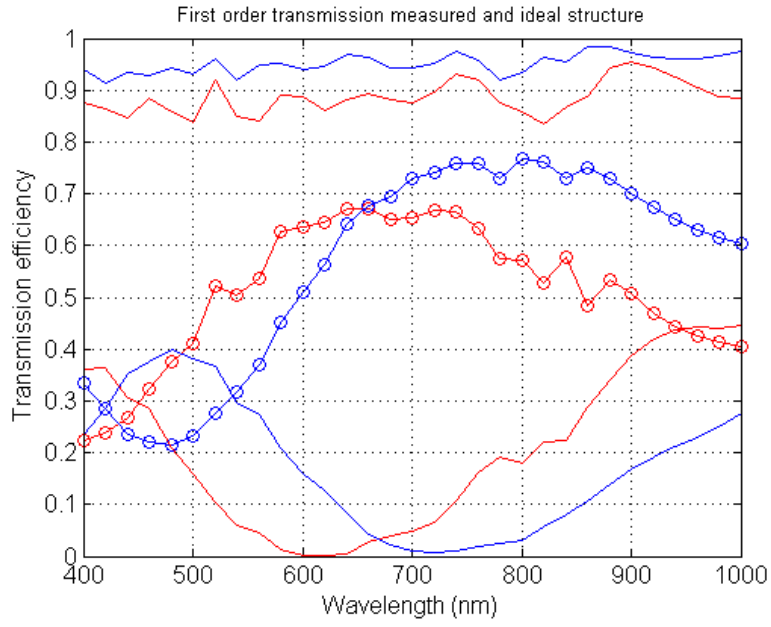
Figure 40: Comparison of measured (red) and "ideal" (blue) parameters. Graphs on top - total TE, middle - first order TE, below - zero order TE

6.2 Anti-reflection structure

The anti-reflection properties of the diatom structures were studied by constructing a grating that comprised only the first stratum, the foramen layer, and the top of an aSi substrate, with air as the superstrate (see figure 9). The pores in the grating were filled with Si_3N_4. The same values for A_H, A_R and P were used in these simulations (see table 2). For the anti-reflection arrangement, we are interested in low RE and large TE values for the first order. As described in the theory section, light diffracted to higher orders translates into a longer path length of light and a higher probability of absorption.

Figure **??** compares the result for both the total RE and the first order for all three of the grating's geometric parameters. The total reflection efficiency is largely dependent on all of the geometric parameters of the grating, but most significantly on the height of the foramen. Increasing the period and decreasing the radius impacts the result in the same manner. Only the period is described here, but results are similar for the radius and the plots can be found in appendix C.

The total RE and the first-order TE can be optimized by choosing a period value equal to 1000 nm (to the left in figure 41).). The values are 0.6 and 0.06. The first order TE can be increased even more by changing the height of the foramen to 500nm , but this increase is obtained at a cost of a larger RE of 0.22. The spectra for total RE and the first order TE for the most optimal result, period equal to 1000 nm, are shown in figure 42 and in figure 43. From the total RE plot it can be seen that the total RE was below 0.1 for wavelengths between 650 and 900 nm. However, at this part of the spectra the first order TE was low and found to decrease from 0.07 to 0.025. From figure 44 and 45 it can be seen how the total RE and first order TE varied with the wavelength for different values of height and it was clear that the default value of the height (100 nm) was the best to obtain low RE.

The result from calculation with a varying period was compared to total RE and first order TE for a homogeneous layer of Si_3N_4. The foramen layer was defined to consist of Si_3N_4 and the radius of the foramen pores was set to be 1 nm. The result can be seen in figure 46 and in table 6. It was found that the first order TE was much larger for the grating structure. The total RE was largest for the grating structure for half of the wavelength spectrum (700 - 1000 nm).
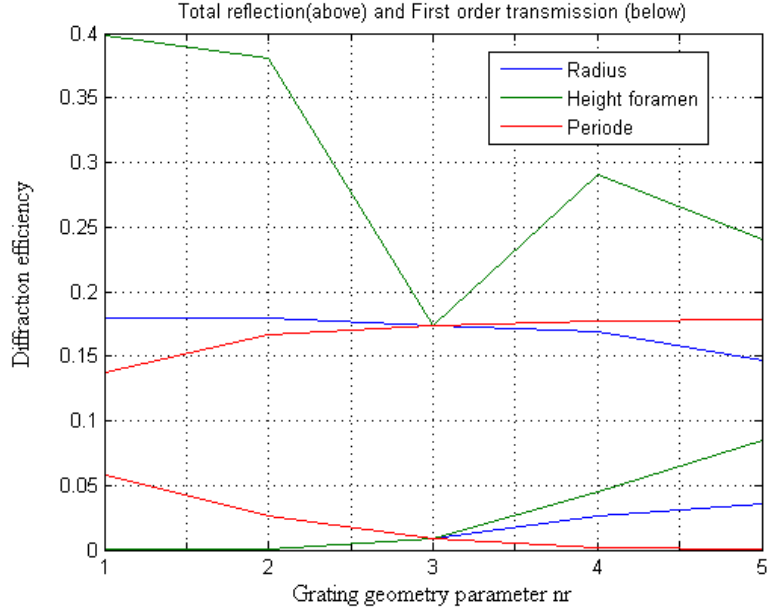
Figure 41: Total RE (above) and first order TE (below) for the anti-reflection structure with foramen between aSi and air and with Si_3N_4 in the pores. The plot corresponds to the upper red curve in figure 43. Legend unit is nm.
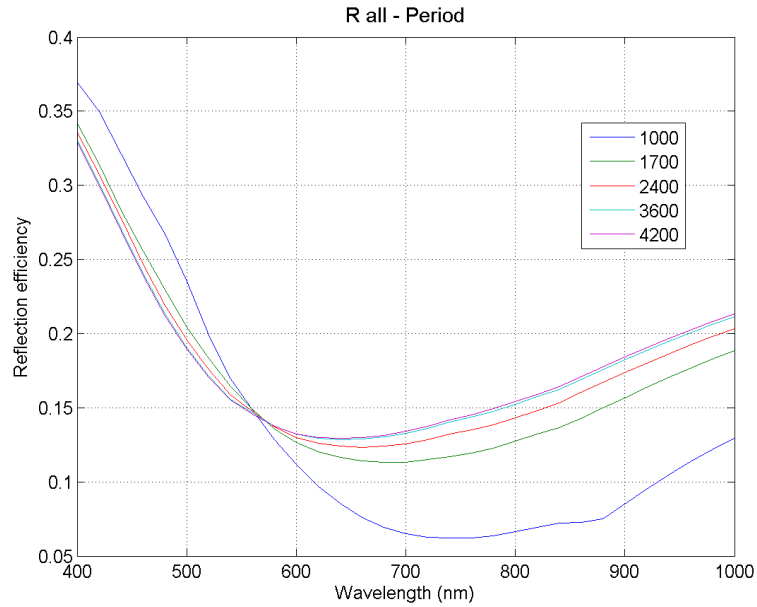
Figure 42: Total RE spectra for five different values of periode in the anti reflection structure setup. The plot corresponds to the lower red curve in figure 43. Legend unit is nm.
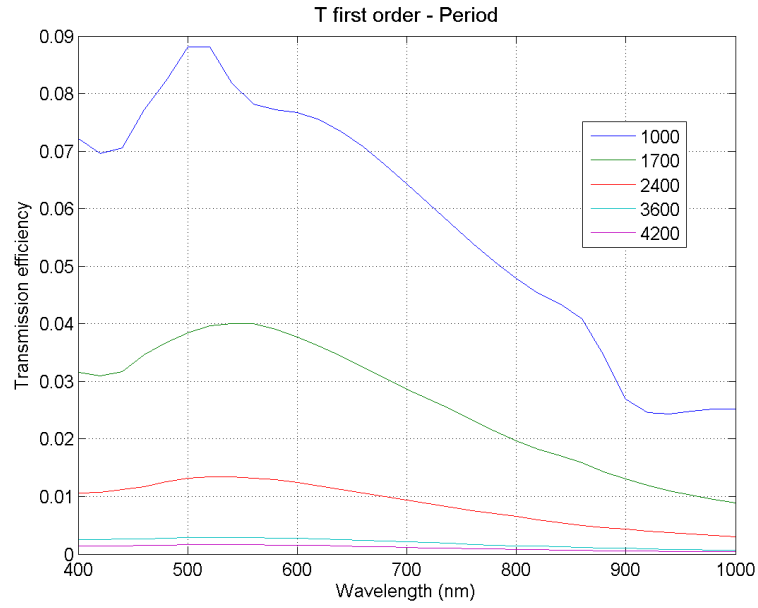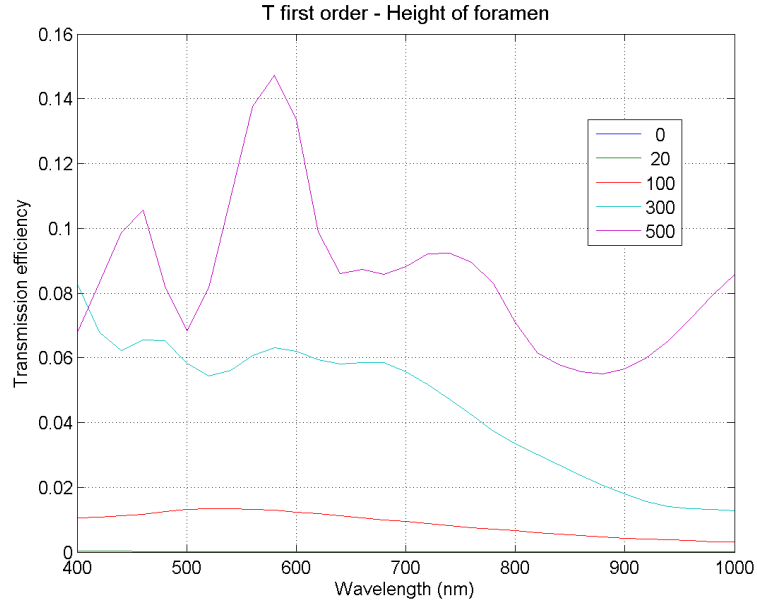
Figure 43: First order RE spectra for five different values of period in the anti-reflection structure setup. Legend unit is nm.
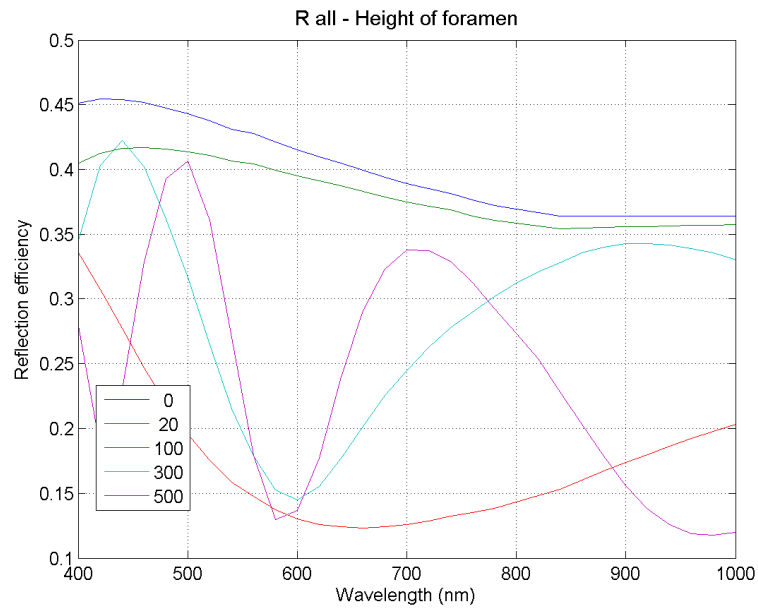
Figure 44: Total RE spectra for five different values of height of the foramen in the anti-reflection structure setup. Legend unit is nm.

Figure 45: First order TE spectra for five different values of height of the foramen in the anti-reflection structure setup. Legend unit is nm.
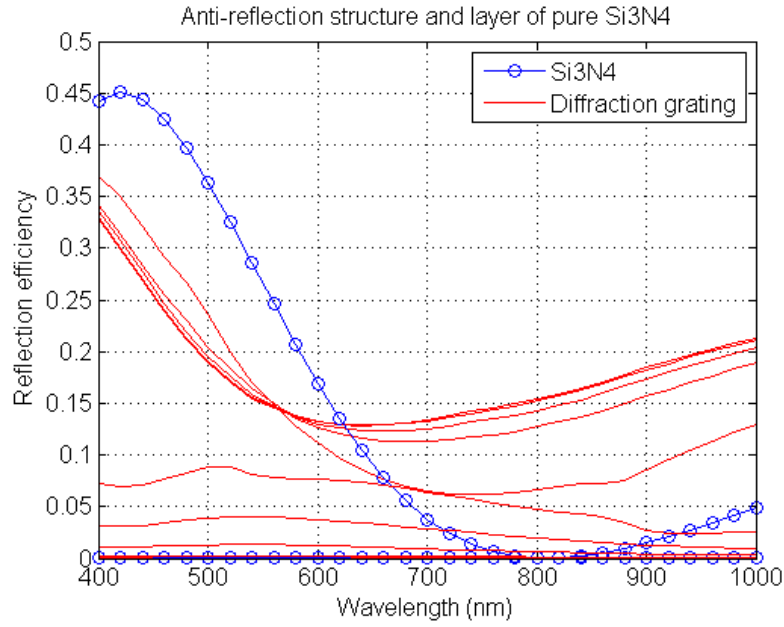
Figure 46: Comparison between layer of Si_3N_4 and the diffraction grating. Total reflection above and first order transmission below. With the five different values of period. Period equal to 1000 closes to the values of a layer of pure Si_3N_4

Comparison of anti-reflection structure with grating and with Si_3N_4 layer		
	Average total RE	Average first order TE
Grating	0.1368	0.0523
Si_3N_4	0.1425	1.5024e-011

Table 6: Comparison of grating structure and with 100 nm thick Si_3N_4 coating

6.3   Back-side diffraction grating

A back-side diffraction grating arrangement was investigated by sandwiching the grating between an Al substrate and an aSi superstrate. The grating consisted of the foramen layer, with aSi in the pores (see figure 9). Here the results are attractive, where the total reflection and the reflection to the first order were both high.

Figure 47 shows the total reflection and the first-order reflection averaged over all wavelengths. It can be seen from this figure that all three of the grating's geometric parameters affect the total transmission. With default parameters, the total reflection is 0.92. However, a slightly higher level of reflection could be achieved by decreasing the radius or increasing the period. The first-order RE has a value of 0.05 at the default values, but can be increased to 0.35 by decreasing the period to 1000 nm. This higher level is obtained at the cost of a 0.1 decrease in total RE.

Figure 49 shows that the total RE exhibits a minimum where wavelengths are around 800 nm. The first-order RE has a maximum at around 550nm and increases from 0 RE at 650 to 0.65 at 1000 nm (see figure 48). The same pattern is seen when the radius is increased. In short, the back-side diffraction grating reflects light efficiently at the default values. At the same time, the first-order reflection is low at these values. By sacrificing some of the total RE, the average first-order RE can be increased to 0.35.

The result form calculation with a varying period was compared to total RE and first order RE for a homogeneous layer of Al. The foramen layer was defined to consist of Al and the radius of the foramen pores was set to be 1 nm. The result can be seen in figure 50 and in table 7. It was found that the first order RE is much larger for the grating structure. With the parameters giving maximum first order RE for the grating, the total RE is slightly lower than the total RE for pure aluminium. For other values of the period, the total RE is largest for the grating structure.

Comparison of two types of back-side reflectors		
	Average total RE	Average first order RE
Grating	0.8322	0.3393
Aluminium	0.9082	3.8519e-013

Table 7: Comparison of back-side reflector with grating structure and aluminium layer
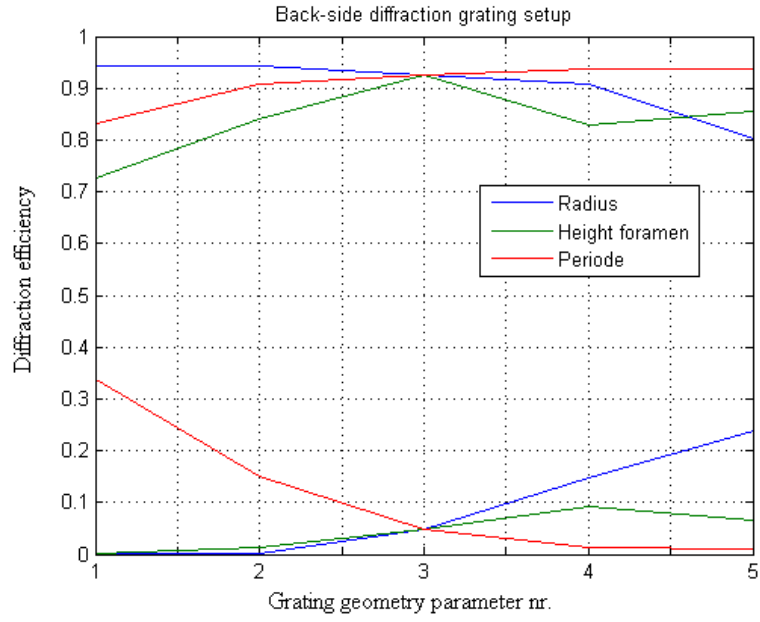
Figure 47: Total RE (above) and first order TE (below) for the Al in the pores
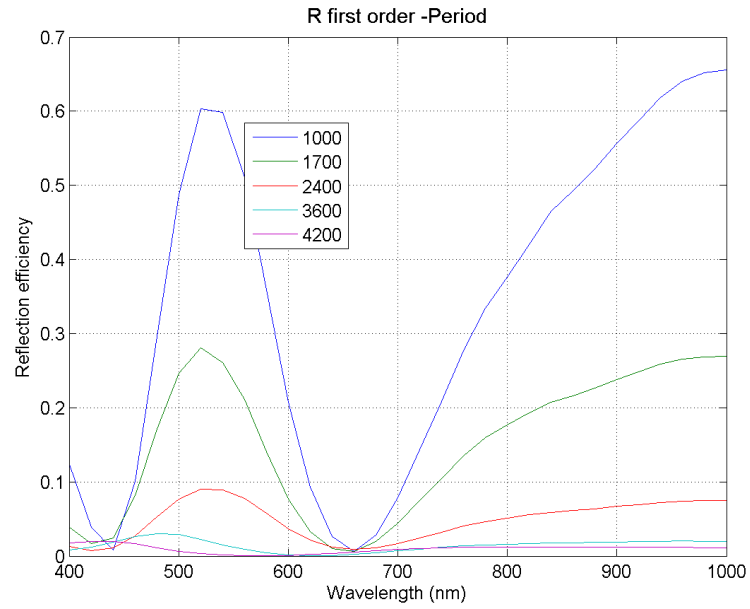
Figure 48: First order RE spectra for five different values of period in the back-side diffraction grating setup. Legend unit is nm.
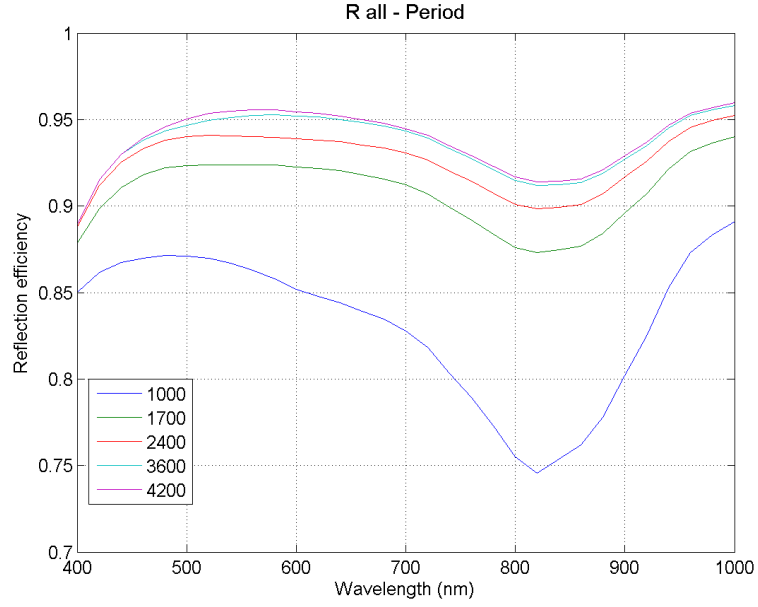
Figure 49: Total RE spectra for five different values of period in the back-side diffraction grating setup. Legend unit is nm.
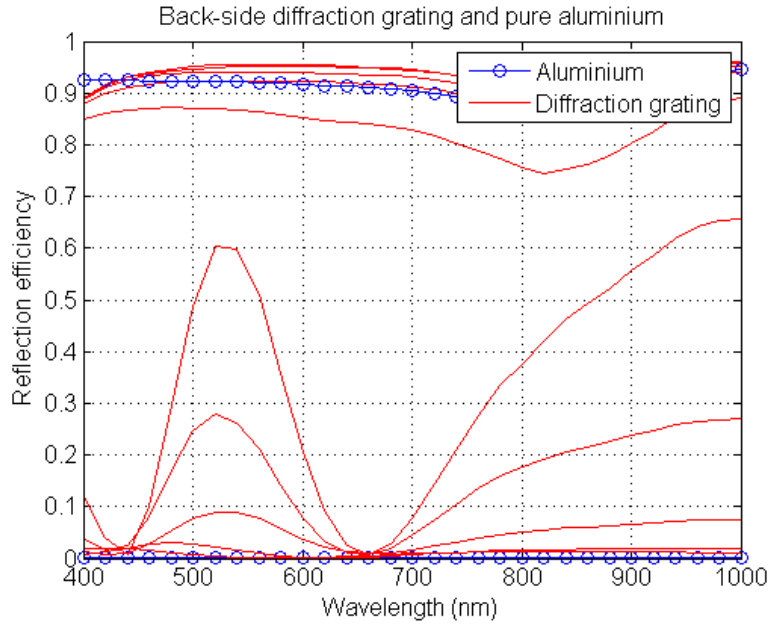

Figure 50: Comparison of two types of back-reflectors; pure aluminum and grating. Total reflection above and first order reflection below.

7 Discussion

This section evaluates the choice of species, the sample preparation method and the characterization technique. This section also includes opinions about the choice of software and an analysis of the degree of accuracy of the model. Finally, the discussion in this section seeks to answer the questions that were asked in the introduction: *How does a model of the diatom frustule structure diffract light? What would be the most ideal diatom structural dimensions for the purpose of diatoms as diffraction grating or in solar cell technology? Would incorporating these structures on the frontal and back-side surfaces increase the light absorption capacities of solar cells?*

7.1 Diatom species

The choice of diatom species appeared to be successful in the way that they had a well-defined and well-ordered pore structure in the valve. This made it possible to adequately describe the structure by using a few parameters and allowed the structure of the model to closely approximate the actual physical structure. The fact that these species are large would be an advantage in any future experiments that employ light beams. It would make it possible for the entire beam of light to strike the inside of the diatom's surface. Since *C. sp.* was harvested from their natural habitat, one does not have the security of being able to collect more material from the same species for future studies. Even though the literature states that the *C.wailesii* manages to complete their first cell division within 48 hours [25], it became clear during the study that this species grows slowly in culture. The species grows hetrotrophically; hence one does not have the same possibility of obtaining large amounts of material as with autotrophic species.

7.2 Characterization - method and results

The cleaning procedure and the sample preparation technique were both found to be suitable for the purpose of the study. Moreover, the characterization procedure allowed for the convenient collection of needed information. However, an atomic force microscope should be used in order to more carefully investigate the fine features of the cribellum. Through the prestudies, this proved to be the optimal technique for looking at thin cribellum structures [22]. Such studies were not carried out here, as they are not crucial for understanding optical properties. The structures are measured quite accurately by the SEM software, where an average of 20-35 values was obtained.

7.3 Method-GD-Calc

FTDT was mentioned as an alternative to RCWA. However, since the differences in thickness were found to be large, RCWA was the best alternative. Another argument supporting this choice is the ability to obtain the efficiencies for separate diffraction orders. Since we are interested in large diffraction, it is important to be able to separate first and zero-order diffractions. Software with a more intuitive user interface could have been an advantage. However, the versatility of GD-Calc means that this software is able to outperform other software solutions. For future studies, it will be advantageous to be able to build the diffraction calculations into a solar cell model that gives current as the output parameter in the same manner as Gjessing *et. al* (2004). However, the analysis is limited to periodic structures, and is thus unable to resemble any given diatomic structure. Constructing diatomic structures with greater complexity would be a tedious process.

7.4 Modeling

As described in the experimental section, the GD-Calc model comprised of three different strata made up of blocks. Due to limitations in the programme, the curvature of the valve is difficult to obtain. It is also very challenging to make a model with the radiating or spiralling pore pattern found in the *Coscinodiscus*. Therefore, the simulations carried out in this study correspond to directing light towards a small portion of the valve. Hence, the optical effects due to the overall structure would not be detected. Since the grating is built from a limited number of stripes and blocks, one might think that it is an inaccurate model. Yet the tests that were carried out (section 5.7) demonstrated that stable results could be obtained with only a few stripes.

The cribrum layer was simplified in the model. Instead of small pores arranged in a group, the model was based only on one large pore with a homogeneous average refractive index. The cribrum pore structure was estimated to be 20% silica and 80% air, thus having a refractive index of 0.2 times the refractive index of SiO_2. Since the layer is only 50 nm thick, the detailed structure in the layer does not significantly affect the diffraction of visible light. Therefore, an arrangement of small pores can be modelled by one large homogeneous pore without seriously affecting the results.

The precise refractive index of the silica is not known. The refractive index of standard silica has been assumed in this study. Previous studies found the refractive index of diatom biosilica to be 1.43 [8], although the variation with the wavelength was not described. A refractive index of 1.43 is 4% lower than

the lowest refractive index used in this study and 7% lower than the highest value. This means that, in reality, the ratio between the refractive indexes for materials used in the grating are somewhat lower, as seen from equation 5. The degree of diffraction could, therefore, be even larger in reality. However, the effect of this difference would not be very pronounced. More accurate values of the refractive index of the diatom biosilica could be obtained in additional studies. At the very least, these small inaccuracies must be kept in mind when comparing simulations and experimental results.

7.5   Simulations

The results obtained when simulating the diffraction in diatom-based grating constitute the foundations for discussions on the diffraction grating properties of the diatom's structure. In the following section, the optimal values for the grating's geometric parameters are discussed. Output values from the two other setups made up the foundation for discussing the role of the diatom's structure in the optically active layers of solar cells. This chapter includes an evaluation of the probability of increasing light absorption through the incorporation of diatoms. The aim has not been to explain the physics behind the light propagation, but rather to look into the practical implementation of diatom structures. The reflected and transmitted efficiencies are compared to some results found in the literature. However, this is not so straight forward, as most studies only describe the resulting cell current and most setups differ somewhat from the setups used in this study.

7.5.1   Grating in air

In the case of the diffraction calculations on the grating in air, only the transmission was investigated. The total TE was found to increase with increasing radius of the foramen and it was also found to vary with the height of the foramen, with a maximum for foramen height equal to zero. The total TE was not proportional to the decrease in height due to a deep minimum at 840 nm wavelength for height equal to 100 and height equal to 500. This minimum was most likely due to constructive interference of the reflected waves leading to higher reflection. Large radius means that the foramen layer was almost removed. It might not be surprising that the transmission through the grating was higher with only one silica layer (stratum 3/cribrum) instead of two. However, it is not straightforward to understand how the thicker walls play a role in the increase of the total transmission. With wall thickness of 10 and 70 nm, the walls was more or less transparent to the light. With larger

thickness the structure served as a diffraction grating. The higher transmission indicates that the grating has some anti-reflection properties.

The most surprising result was the large first order TE between wavelengths of 500 to 1000 nm. The first order TE was affected by change in all of the grating geometry parameters. However, the change in first order TE with radius of the formamen seemed to only be due to the increase in total. The amount of first order transmitted light per the amount of total transmitted light seemed to be constant. The reason why change in radius did not contribute to a change in total TE could be because the foramen was so thin. The thickness of the layer, on the other hand affected the first order transmission. With zero order thickness, the first order TE is largest. The default value of the period (2400 nm) gave significantly higher first order transmission than the lower and higher values of the parameter. The first order TE also increased significantly with increase in the wall thickness. The average value of the first order TE was not changed above a thickness of 135 nm, but the with an increased thickness the curve was shifted to the right. Larger thickness of the wall increased the first order TE and shifted the maximum of the curve to the right. In other words the the spectra of the first order transmitted light could be tuned by changing the wall thickness. This assumption should test with even thicker areola walls.

From the results it seemed like a large part of the transmitted light was diffracted into diffraction orders with higher order than 1. For light with a wavelength of 600 nm the total first order reflectance was around 0.9. and the zero order TE was zero. However, the TE in first order was found to be only 0.65 and consequently must the transmitted efficiency into higher orders have been 0.25. The amount of light scattered to higher orders should be investigated in further studies. The answer could also be found by looking at Fourier transformations and Bessel functions describing the intensity in various diffraction orders as a function of the grating properties. This type of investigation would also reveal whether the result could be trusted or not.

The full parameter combination space have not been investigated in this study, the perfect combination of parameters giving the maximum transmission and scattering could there for be somewhat different. Iterations could be used to find a potentially higher maximum, but this would be a demanding procedure.

In our limited search for the ideal parameters, the original parameters gave good results. However, it was shown that the result could be improved further by removing the foramen and increasing the thickness of the wall. Originally, the default value for the radius was calculated as an average over two size distributions (see table in appendix B). The first distribution had radius of 450 nm, and this would bring the measured value closer to the ideal value. The small difference between the "ideal" and the measured values are surprising.

Several diatoms do only have one layer of silica, like in the "ideal" structure. *C. wailesii* is one example, however this species do not exhibit the same hight of the areola. A diatom with high areola walls, a certain thickness and a certain period is needed to get the best results.

It can seem as if the the diatom structure are optimized for diffraction of visible light. However, it must be kept in mind that the diatoms live in water, whit have a refractive index of 1.33. This means that the refractive index ratio is much lower than the ratio between air and silica and one can not make any clear conclusions about the diatom frustles impact on the light harvesting based on simulations of the frustule in air. Simulations done with water as the surrounding media would shed light on this question. It could also be that the radiating pattern and the curvature of the valve may play a role for the light behavior in diatom. These features could be included in a future study.

According to Stefano *et. al* the diatoms exhibit a lensing effect focusing light passing through the diatom. It was found that the lensing effect was due to light scattered by pores on the diatom surface and interfering constructively at fixed distance. This is in agreement with the strong scattering found in this study. With the strong scattering, the result will be a higher intensity at a centered at a certain distance from the valve.The species studied by Stefano *et. al* was *C. sp.* It could be that the rows of pores found in *C. sp.* affects the diffraction and directs a portion of the spectra towards. Radiating pore pattern. Fuhrmann *et. al* described enhanced light absorption of blue light and stated that excess supply of blue light give rise to active oxygen, which would be harmful for the organism.It could be that the blue light is scattered inside the frustule to uniformly irradiate chlorophylls inside the diatoms. It is known that the diatoms use both blue and red wavelength regions for photosynthesis. An excess supply of blue light, however, gives rise to active oxygen, which is harmful to organisms. Thus, one of the roles of the nanostructures inside the frustules may be the tuning the amount of blue light focused inside of the frustule.

The relevant question for this study is whether or not this properties could be exploited in a solar cell. The high transmission and high degree of scattering is desired to increased the path length of light in the active material. Even though the properties of diatoms seems promising the However, For the diffraction grating to work as efficient in a solar cell setup, the same ratio between the refractive indexes must be maintained. Without the foramen layer, the structure will be more easy to fill with a different material. The same ratio as of air and silica, the with silicon, the silica have to be replaced with a material with refractive index of 2.85. But with these high refractive indices, the reflection would be quite large. Maybe other applications for the naturally fabricated diffraction gratings would be more useful in other applications.

7.5.2   Anti-reflection structure

The total RE was lowest for the default value of the height (100 nm). The value of the height affects the path length of light and consequently the degree of phase shift of the beam reflected from the aSi surface. The maximum and minimum at different heights was due to different degree of interference due to the different phase shifts (Se figure 5).

Further on, a period equal to 1000 nm gave the lowest total RE. This value also gave the highest first order TE with a maximum of 0.09 for light with wavelengths equal to 500 nm. However, as described in the result section, the part of the spectrum scattered most was the high energy segment. In silicon solar cells, this segment of the spectrum is already sufficiently absorbed in the active layer. The result is therefor not optimal if considering the distribution of the first order diffraction.

The maximum first order TE was found at foramen height equal to 500 nm and the maximum first order transmission was found at wavelengths of 570 nm with a value of 0.145. In reality this value might be lower since since the complex part of the aSi is not included, assuming no absorption in the substrate.

It was found that response to variation of period and radius is the same. the degree of diffraction is obviously dependent on the ratio of area covered with silica to the total area. This parameter is termed fill factor. In further studies this parameter should be used in stead of the radius and period.

Compared to a homogeneous layer of 100 nm Si_3N_4, the reflection was lower for the low energy part of the spectrum. The average is quite similar. With a reflection of 0.1368 for the grating and 0.1425 for the Si_3N_4 layer, the total reflection is in average 4% lower for the grating. The first order transmission of 0.058 in average was also higher for the grating structure. With the homogeneous layer, the first order TE is close to zero. The grating would be a better solution if low reflection over the the whole wavelength spectrum (400 - 1000 nm) is desired, assuming that the absorption in aSi do not affect the results.

7.5.3   Back-side diffraction grating

The results showed that the total reflection was above 0.7 for all values of the grating geometry parameters. The total TE was highest for small foramen radius and high period. The highest first order RE was achieved for a radius of 1000 nm or a period of 1000 nm. In other words none of the values are optimal for achieving both high first order and total RE.

The default value for the first order reflection is 0.05. By choosing a smaller period, the first order RE can be increased from 0.05 to 0.35. At the same time will the total transmission be reduced from 0.92 to 0.83. This can however be a beneficially trade. The low diffraction is however not surprising since the ratio between the refractive indices of aSi and SiO_2 is small.

Increasing the period and decreasing the radius gives the same output. The relation between area SiO_2 and area of aSi (relation between period and radius) are named fill factor. Hence, the degree of first order RE and total RE are found to be dependent of the fill factor. As stated above, high total reflection was achieved with large fill factor (large coverage of SiO_2), while a high first order RE was achieved with a lower fill factor.

Gjessing *et. al* found that a fill factor of 0.7 and a period of 900 nm was beneficial [9]. The fill factor found to be optimal in this study was 0.88. The optimal period was 1000 nm. However, the results can not be compared directly since Gjessing *et. al* have a layer of silica in between. As mentioned by Gjessing *et. al*, an advantage of using SiO_2 is the reduced parasitic absorption.

The total reflection from a layer of aluminum was lower than expected, but it is anyway used as the foundation in this discussion. Comparison with a layer of pure aluminium showed that the diatom grating gave better results. With the default parameters, the total reflection was only 0.92. The "loss" in reflection efficiency compared to having pure aluminum have to be compensated by more first order reflection for the scheme to be efficient. As seen in table 7 Could get even better result with aluminium in the pores or with a layer of aluminum on top of the grating. he efficiencies would have been higher if one had a larger refractive index ratio. Hence, aluminum could be used inside of the pores instead of aSi.

7.5.4   Diatom structures in solar cell

As seen in the previous sections, diatoms in optical active layers in solar cells has a potential to outperform current technologies. In order to achieve successful incorporation of diatoms in a solar cell arrangement, a method for creation of a diatom monolayer has to be developed. Also a cleaning procedure which preserves the structure is important. In order for incorporation of biosilica from diatoms to be a good solution it has to alter the price/efficiency ratio in the right direction. Current etching technology is demanding and hazardous. The growth process of diatoms is in contrast non-demanding an a large amount of material can be produces in short time with fast growing autotroph species, as described in the theory section. However, since autotroph species do not depend on light harvesting,it could be that these species do

not exhibit the same degree of periodic pores in the valve. Even if the diatom material is cheap it does not help if processing of a diatom laye ris demanding and not suitable for large scale production. A species with the correct dimensions must be found.

8   Conclusion

The valve structures of two species from the genus *Coscinodiscus* have been investigated in this study. The two species were found to have different levels of complexity. This illustrates the presence of a wide variety of diatom shapes. *Cosciondiscus sp.* was found to have several layers of silica, and the valve structure of this diatom has been investigated and described in detail.

A diffraction grating based on the valve structure of *C. sp.* was constructed in GD-Calc. The software enabled diffraction studies and investigation of the different diffraction orders and proved to be useful. Diffraction studies were done on the grating surrounded by air, and on two different arrangements that emulated a solar cell. In the first set up, the grating was placed on top of an amorphous silicon substrate. (Si_3N_4) were used to fill the pore. The superstrate was air. In the second setup, the grating was sandwiched between an aluminium substrate and an amorphous silicon superstrate.

The results from the diffraction studies indicate that the diatom valve transmits around 90% of the light and that the diffraction to higher orders is efficient. At wavelengths of around 600 nm, zero percent of the light is transmitted to the zero order. The different structural parameters were varied over a wide range of sizes and it was found that the properties can be further optimalized by changing the value of the parameters.

The inclusion of diatom biosilica in an anti-reflection setup gave, averaged over wavelengths, slightly lower reflection than a standard layer of Si_3N_4. The first order transmission was between 0.05 and 0.1. The back-side diffraction grating exhibited high reflection efficiencies, in the same range as a aluminium back-reflector. A portion of the reflection efficiency had to be sacrificed in order to achieve higher first-order diffraction efficiencies.

This study contributes to the development of greater insights into the structural and optical properties of one of the diatom species. The result from this work can serve as a starting point for further investigations. Tools which can be useful in future studies have been developed in the present study. A GD-Calc grating model of the *Cosciondiscus sp.* has been made and source code for diffraction calculations has been developed. The study constitutes a foundation and a collection of useful tools for guiding additional investigations into different setups and variations of other parameters, such as the angle for example. The final conclusion is that diatoms have been found to have interesting and promising properties, and the full potential of their optical properties and their role in solar cell technology should be subject to further investigation.

9   Future Work

This study could be extended into additional work in different directions. In this section, some of the different possibilities are listed, starting with the ones most relevant for this study and continuing with more general topics.

* More insight into the optical properties of diatom frustules could be gained through more extensive simulations in GD-Calc. The simulations could be carried out by adding new geometric parameters to the grating. Simulations should also be performed to show the angle dependence of the diffraction. A more detailed model, including the valve curvature and the radiating pore pattern, could be made in order to investigate how these features affect the optical properties of the diatom. With more computational capacity, additional diffraction orders could be retained in the simulation. The complex refractive index of aSi should be used to give more realistic result.

  Other solar cell arrangements could be investigated by addition of new materials. A set up with aluminium in the pores should be tested. The algorithm could be extended to give current as the output instead of diffraction efficiencies. This would make it easier to compare the results to previous studies. In addition, a thin homogeneous layer with the function of an anti-reflection coating could be added on top of the diatomic texture layer.

* The results from the simulations could be compared to experimental results obtained from integrating sphere studies. A hyperspectral camera could potentially serves as another possible tool in such studies.

* A search for species more suitable for this purpose could be carried out.

* Other solar cell applications could be tested, such as dye-sensitized solar cells.

* Before diatom frustules could be practically implemented in solar cells or other applications, a method for creating a monolayer of cells needs to be developed.

* As stated in the introduction, diatom biosilica could serve as a potential for a wide range of applications. There exists a potential for a wide range of research projects.

References

[1] J.-N. Audinot, C. Guignard, H.-N. Migeon, and L. Hoffmann. Study of the mechanism of diatom cell division by means of 29si isotope tracing. *Applied Surface Science*, 252(19):6813 – 6815, 2006.

[2] A. Bismuto, A. Setaro, P. Maddalena, L. De Stefano, and M. De Stefano. Marine diatoms as optical chemical sensors: A time-resolved study. *Sensors and Actuators B: Chemical*, 130(1):396 – 399, 2008.

[3] Bouhafs D., Chikouche A. Moussi A. and, and Ruiz J. M. Design and simulation of antireflection coating systems for optoelectronic devices: Application to silicon solar cells. *Appl. Phys.," Solar Energy Materials and Solar Cells*, 79, 1998.

[4] Campbell P. and Green M. A. Light trapping properties of pyramidally textured surfaces. *J. Appl. Phys. 62*, 243, 1987.

[5] Dobrowolski A., Guo Y., Tiwald T., Ma P., and Poitras D. Toward perfect antireflection coatings. 3. experimental results obtained with the use of reststrahlen materials. *Applied Optics*, 45(1555), 2006.

[6] Dobrowolski J. A., Poitras D., Ma P., Vakil H., and Acree M. Toward perfect antireflection coatings: Numerical investigation. *Applied Optics*, 41(3075), 2002.

[7] Hasle G.R. Syvertsen E.E. *Marine Diatoms. Identifying Marine Diatoms and Dinoflagellates.* Academic Press, Inc., California., 1996.

[8] Fuhrmann T. Diatoms as living photonic crystals. *Applied Physics B*, 78, 2004.

[9] Gjessing J., Marstein S, and Sudb Aø. 2d back-side diffraction grating for improved light trapping in thin silicon solar cells. *Opt. Express*, 18(6):5481–5495, 2010.

[10] Gordon R. The glass menangerie: diatoms for novel applications in nanotechnology. *Trends in Biotechnology*, 27(2), 2008.

[11] Hecht E. *Optics 2.nd edition.* Addison-Wesley Pub. Co., 1987.

[12] Robert Hull. *Optical Properties of Si Properties of Crystalline Silicon, emis DataReviews Series No 20.* INSPEC, IEE, 1999.

[13] P. Altermatt J. Zhao, A. Wang and M. A. Green. Twenty-four percent efficient silicon solar cells with double layer antireflection coatings and reduced resistance loss. *Appl. Phys. Lett*, 66:3636, 1995.

[14] Johnson R.C. Diatoms could triple solar cell efficiency. *EE Times*, 2009.

[15] Men Tao Li Chen, Hongjun Yang and Weidong Zho. Microstructured anti-reflection surface design for the omni-directional solar cells. *Optical Modeling and Measurements for Solar Energy Systems II, edited by Benjamin K. Tsai, Proc. of SPIE*, 7046, 2008.

[16] Li H., Jeffryes C., Gutu T., J. Jiao, and Rorrer G.L. Peptide-mediated deposition of nanostructured tio2 into the periodic structure of diatom biosilica and its integration into the fabrication of a dye-sensitized solar cell device. *Materials Research Society (MRS) Symposium Proceedings*, 1-8(1189E), 2009.

[17] Losic D, Rosengarten G, Mitchell JG, and Voelcker N. Porearchitecture of diatom frustules: Potential nanostructured membranes for molecular and particle separations. *J Nanosci Nanotec*, 6, 2006.

[18] David G. Mann. The species concept in diatoms. *Plant Systematics and Evolution*, 164:215–237, 1989. 10.1007/BF00940439.

[19] N. Poulsen N. Kröger. Diatoms - from cell wall biogenesis to nanotechnology. *Annu. Rev. Genet.*, 42, 2008.

[20] Michel Neviere and Evgeny Popov. *Light Propagation in Periodic Media: Differential Theory and Design (Optical Engineering)*. CRC, 2002.

[21] V. Nikolaev. The "‘pore"’ apparatus of centric diatoms: a description of terms. *Nova Hedwigia*, 106:33–42, 1993.

[22] Anne Kirsti Noren. Characterization of structure and properties of diaoms for enhanced efficiences in solar cells. 2010.

[23] Poitras D. and Dobrowolski J.A. Toward perfect antireflection coatings. 2. *Theory," Applied Optics*, 43(1286), 2004.

[24] Minseung Ahn Ralf Heilmann and Mark Schattenburg. Nanomirror array for high-efficiency soft x-ray spectroscopy. *SPIE Digital library*, 2008.

[25] F.E. Round, R.M.Crawford, and D.G.Mann. *The Diatoms*. Cambridge University Press, 1990.

[26] Stefano L. Lensles light focuseing with the centric marine diatom Cosinodiscus walesii. *Optics Express*, 15(26), 2007.

[27] Townley E. *et. al.* Modification of the physical and optical properties of the frustule of the diatom coscinodiscus wailesii by nickel sulfate. *Nanotechnology*, 18, 2007.

[28] Trupke T., Wiirfel P., and Green M. Up- and down-conversion as new means to improve solar cell efficiences. *3rd World Conference on Photovoltoic Enera Cowerrion*, 2003.

AppendixA

A glossary of diatom terminology used to describe features of a diatom frustule [21], [25], [7]. See also frustule.jx3.net/index.php.

Areola - Perforation through valve with internal or external sieve membrane.

Cribellum - see Cribal pore

Cribral pore - An opening (often circular) in the thin siliceous layer (velum) covering an areola. Sometimes cribral pores are covered by a thin siliceous, perforated plate (cribellum)

Cribrum - A velum perforated by cribral pores of uniform or various outlines, occasionally imperforate or interrupted near the inter-areolar walls. Sometimes the cribrum is uninterrupted across the areola walls, extending over the whole valve surface. (A multi-perforate or meshwork plate, with often an even thinner perforate or slit membrane across the meshes; this type has frequently been termed a "sieve membrane" in recent literature.)

Epivalve - Larger (and thus older) of two valves of a frustule.

Foramen - The opening of an areola on the side opposite to the velum.

Frustule - The valves and their associated girdleband elements

Girdle bands -Terminology used to describe the overlapping hooplike band that joins the two valves of a frustule (i.e. the part of frustule between the epitheca and hypotheca).

Hypovalve - Smaller (and thus newer) of two valves of a frustule.

Loculate areola - A chamber in the basal siliceous layer, occluded on the internal and external surface of the frustule by a velum of various types. The chamber diameter is larger than that of the foramen and varies in form from rounded to polyhedral.

Valve face - Portion of the valve apparent in valve view (oriented to the valvar plane.

Valve mantle - Portion of the valve, differentiated by slope, that is apparent in girdle view (oriented to the apical plane).

Valve - Siliceous part of the frustule containing most of the morphological features used to describe diatoms. Each valve has two surfaces, the face and the mantle.

Velum - A thin, usually perforated (rarely imperforate) siliceous layer on one of the frustule surfaces

Appendix B
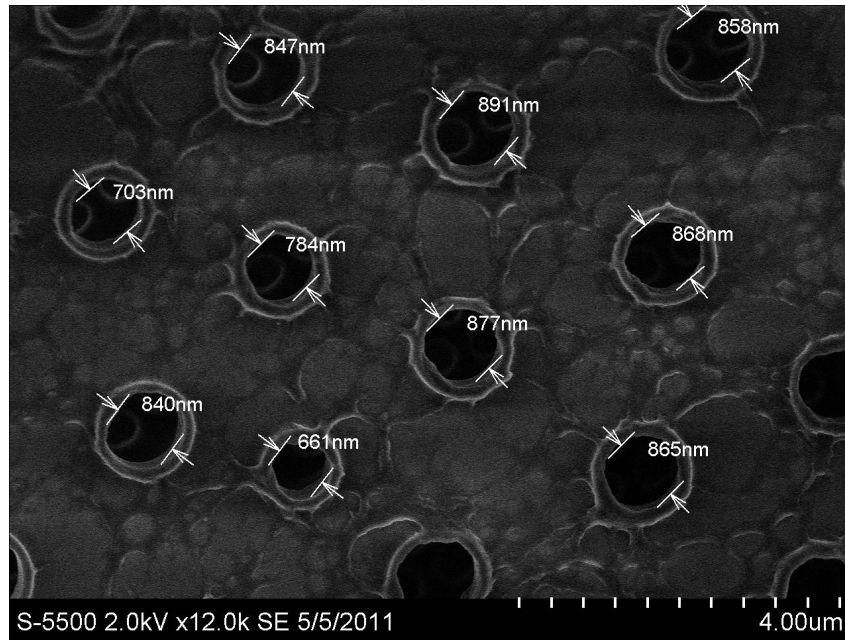
Figure 51: Radius foramen
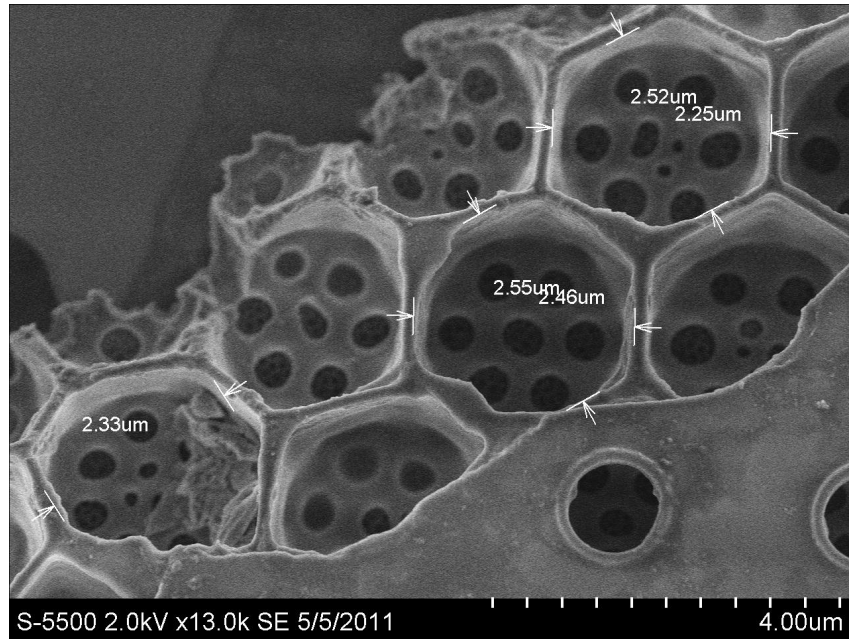
Figure 52: Period
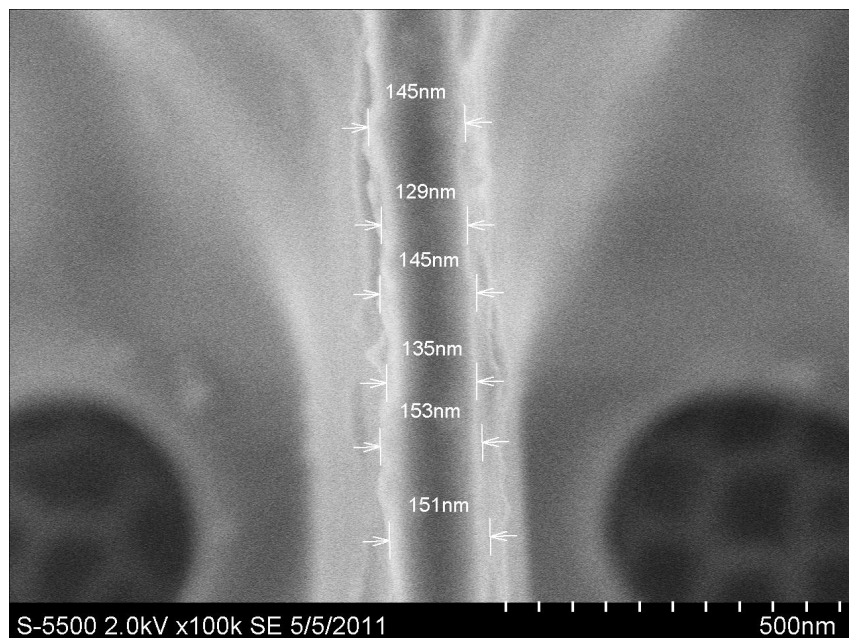
Figure 53: Measured thickness of areola wall
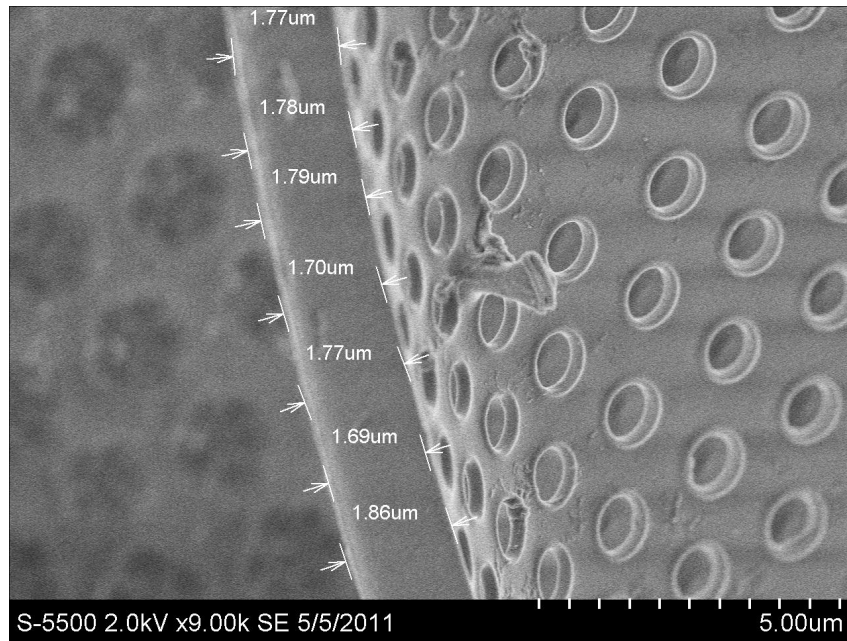
Figure 54: Height areola
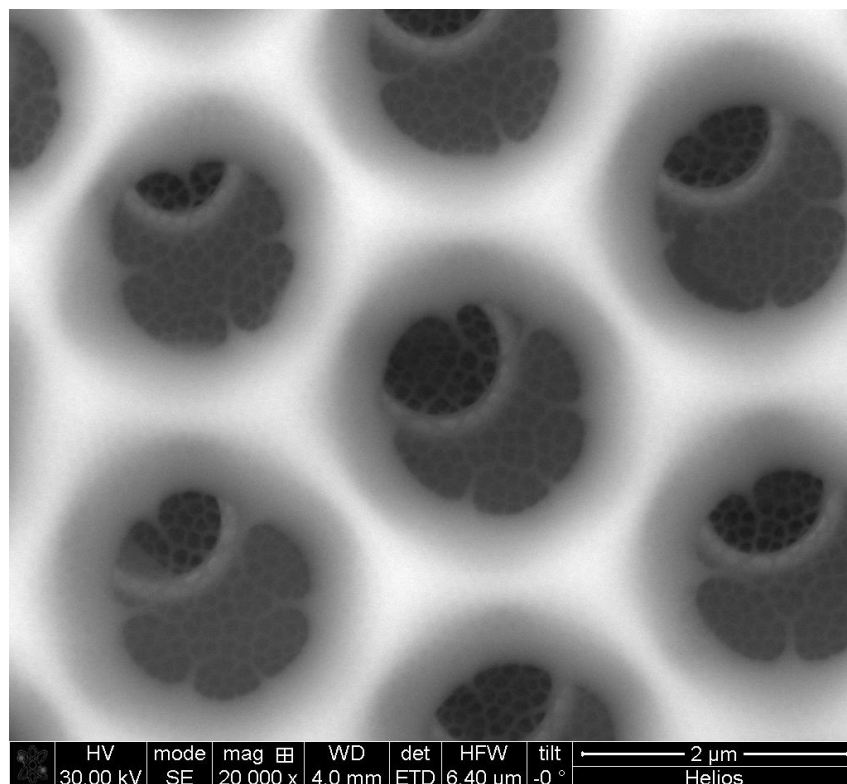
Figure 55: Image of the cribellum

HV	mode	mag ⊞	WD	det	HFW	tilt	⊢——— 4 µm ———⊣
30.00 kV	SE	10 000 x	4.1 mm	ETD	12.8 µm	52 °	Helios

Figure 56: FIBCUT

HV	mode	mag ⊞	WD	det	HFW	tilt	⊢——— 2 µm ———⊣
30.00 kV	SE	20 000 x	4.1 mm	ETD	6.40 µm	-0 °	Helios
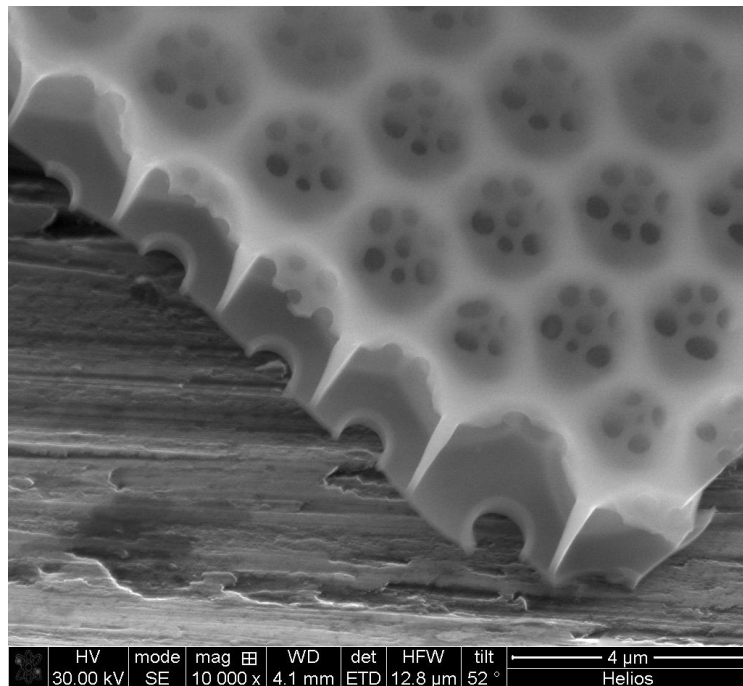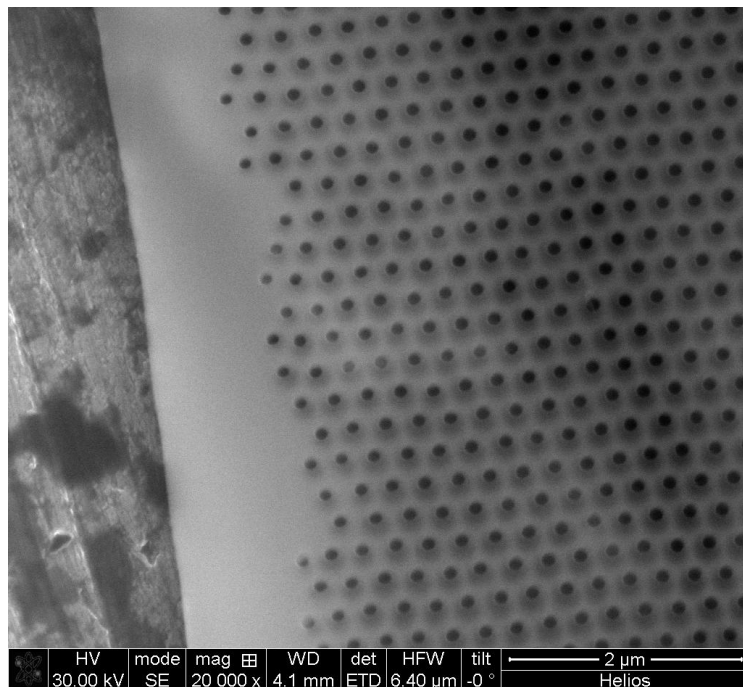
Figure 57: Girdle band

Radius foramen					
	1008	840	528	669	480
	912	661	564	610	592
	983	865	481	545	518
Total average	772	877	563	513	515
342	936	784	606	632	526
Total standard	912	703	608	538	435
deviation	870	847	562	680	596
184	946	891	538	518	482
	1002	858	542	558	372
	1004	868	...	...	...
Average	935	819	582	583	511
Standard dev.	74	78	45	45	61

Figure 58: Table with measurements of the radius of the foramen. ... means that some values are removed for the sake of the presentation in the report (nm).

Wall thickness				
	154	139	138	129
	139	139	124	127
	127	145	127	132
Total average	122	129	137	125
135	110	145	135	129
Total standard	128	135	136	153
deviation	116	153	125	156
13	122	151	124	173
	115	141	134	160
	131	132	131	143
Average	126,4	140,9	131,1	142,7
Standard dev.	13	8	6	17

Figure 59: Table with measurements of the wall thickness of the areola (nm).

Thickness areola (µm)	
	2,04
	1,23
	1,9
	1,4
	2,11
	1,82
	1,89
	1,43
	1,3
	2,2
	1,3
	2,09
	2,33
	2,09
	2,17
	2,17
	2,34
	2,32
	2,16
	1,78
	1,77
	1,9
	1,77
	1,9
	1,49
	1,42
	1,3
Average	1,84
Standard dev.	0,35

Figure 60: Table with measurements of the height of the areola.

Periode (µm)	
	2,32
	2,34
	2,4
	2,45
	2,33
	2,46
	2,55
	2,52
	2,25
	2,41
	2,22
Average	2,39
Standard dev.	0.11

Figure 61: Table with measurements of the period of the structure.

Appendix C

Diatom grating - Radius foramen - Reflection
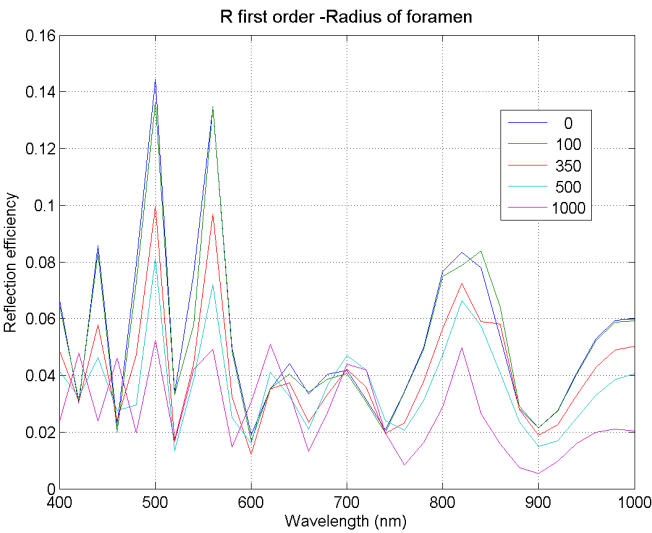
(a)
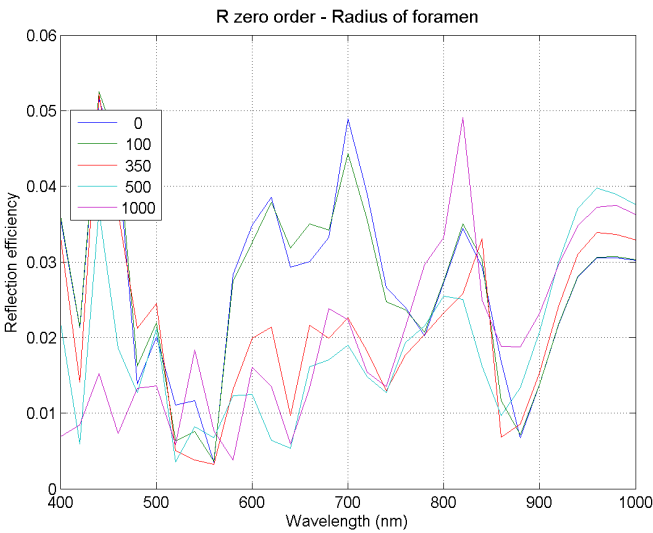
(b)
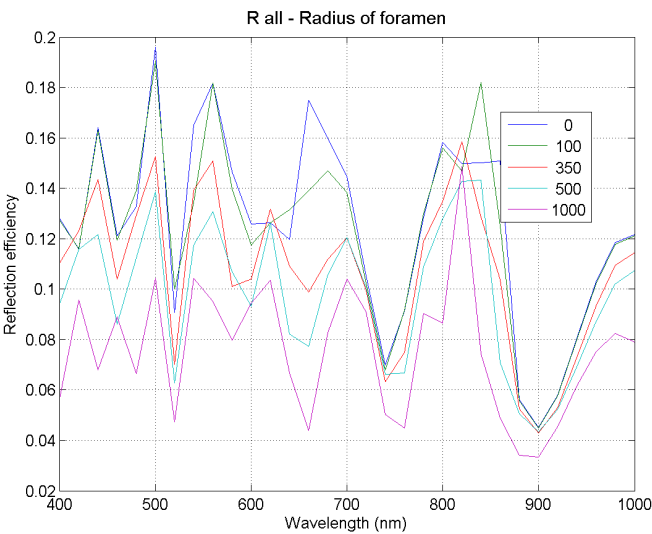
(c)
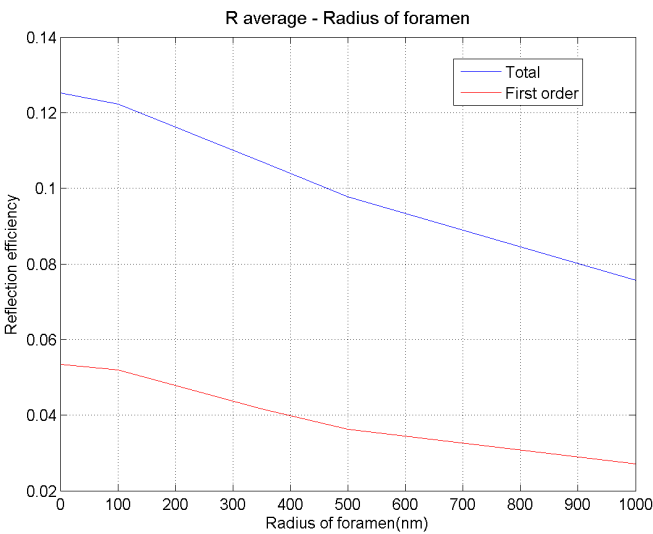
(d)

Diatom grating - Radius foramen - Transmission
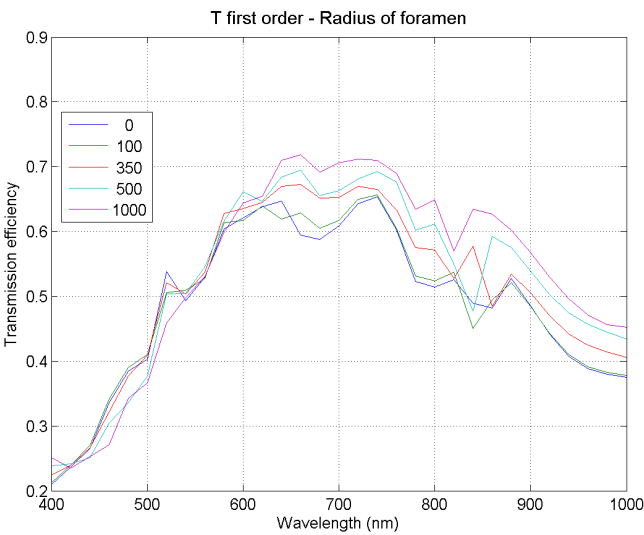
(e)
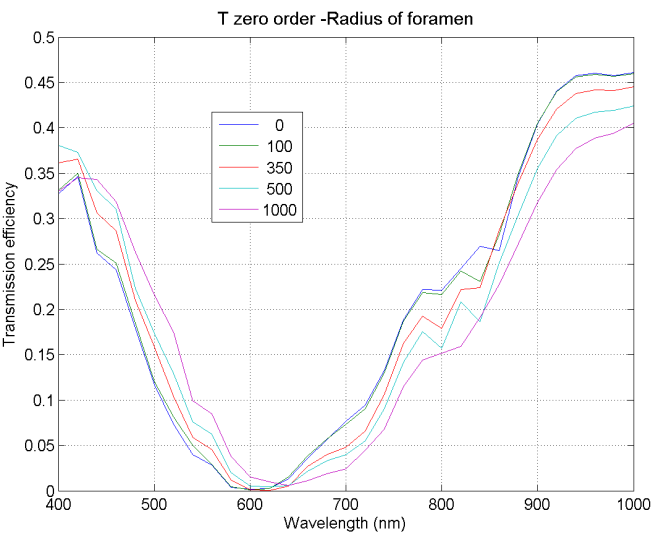
(f)
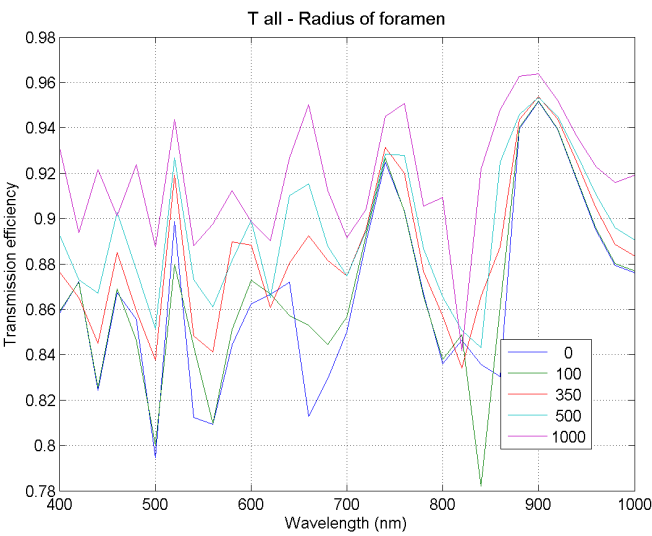
(g)
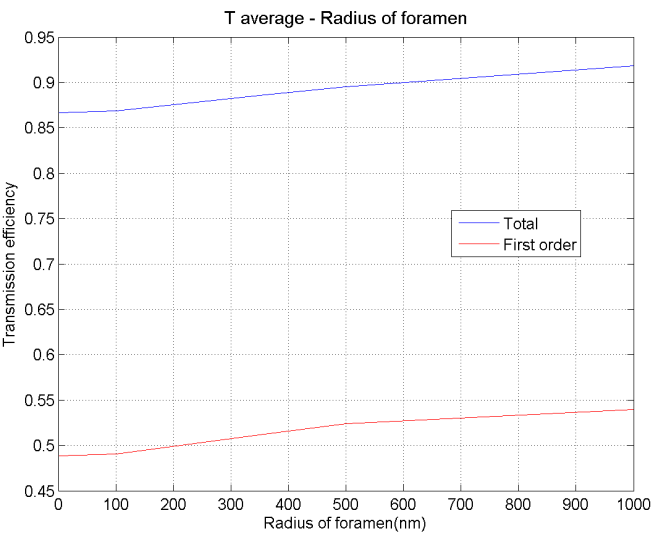
(h)

Diatom grating - Height foramen - Reflection
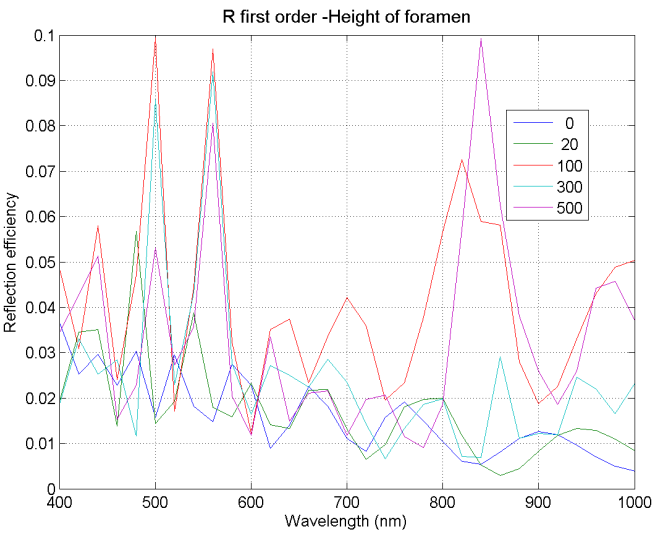
(i)
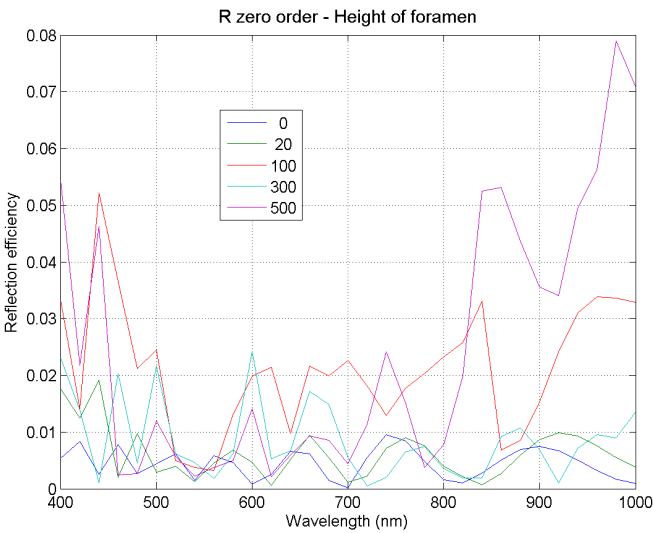
(j)
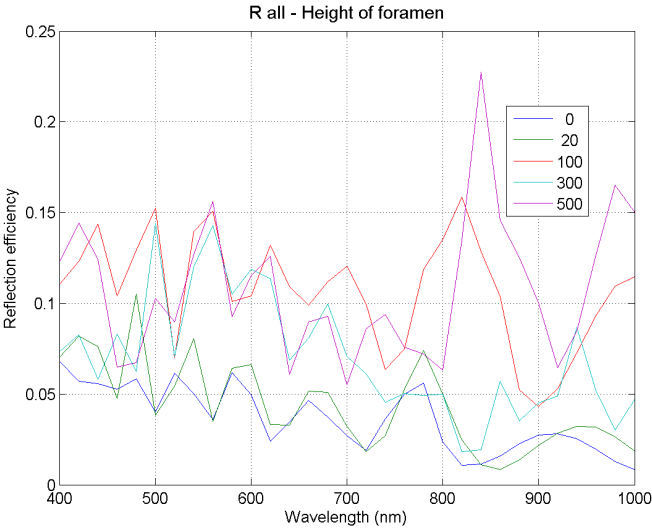
(k)
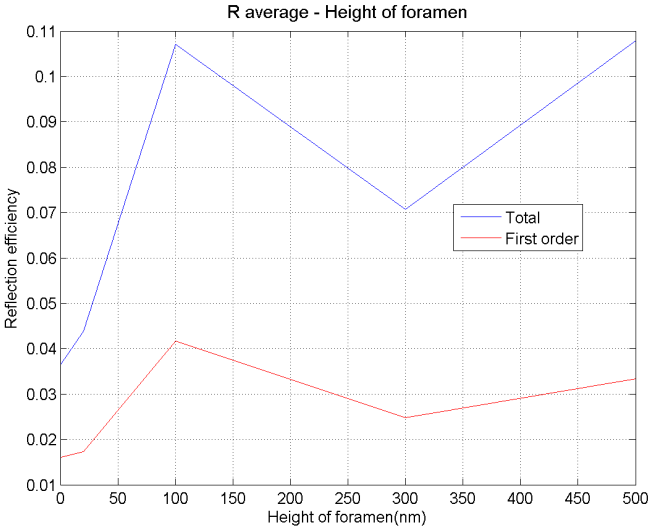
(l)

Diatom grating - Height foramen - Transmission
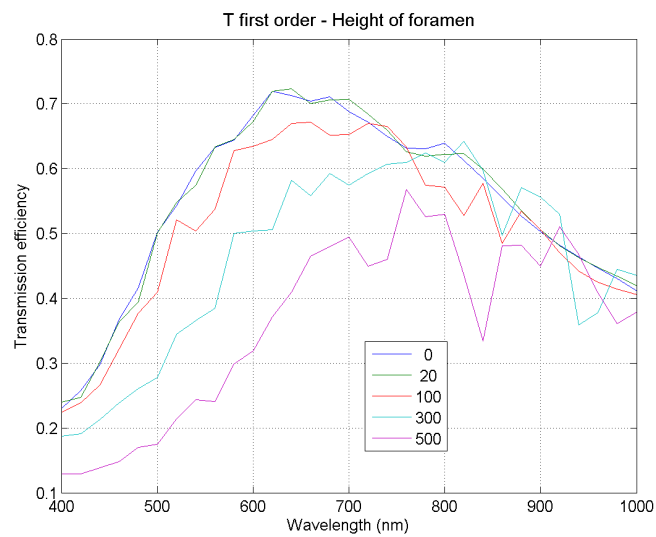
(m)
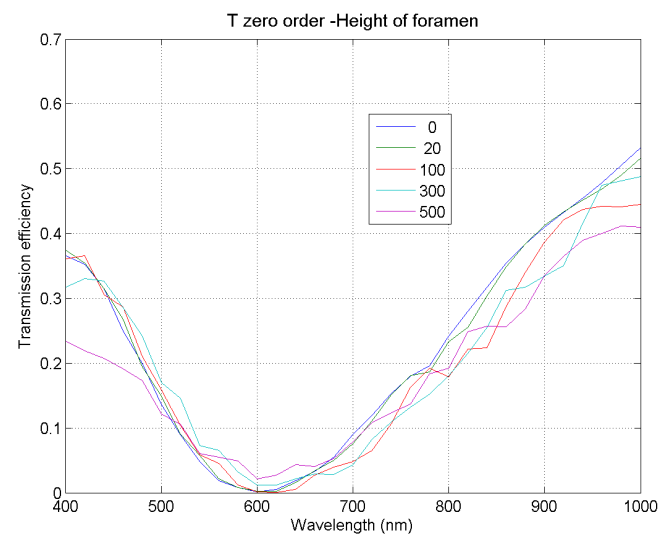
(n)
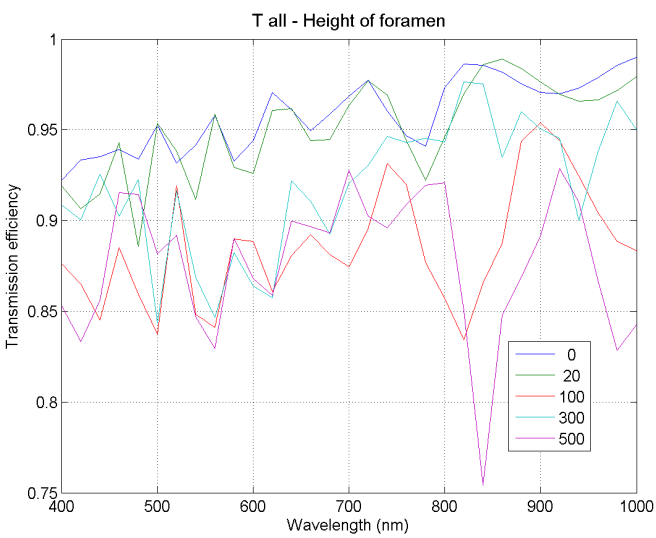
(o)
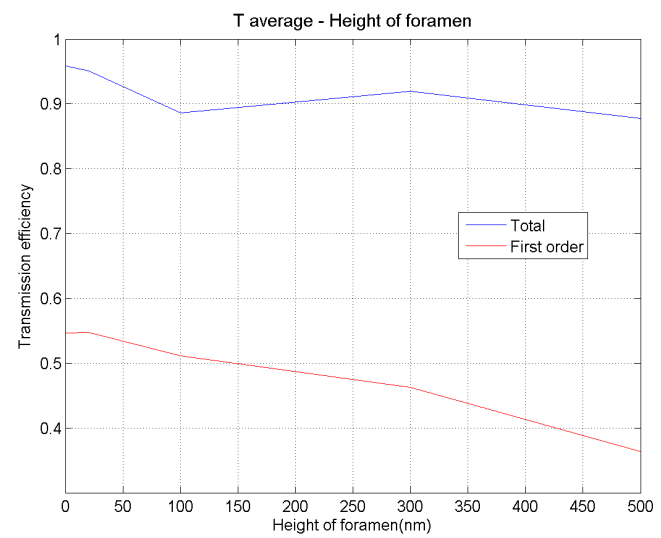
(p)

Diatom grating - Period - Reflection
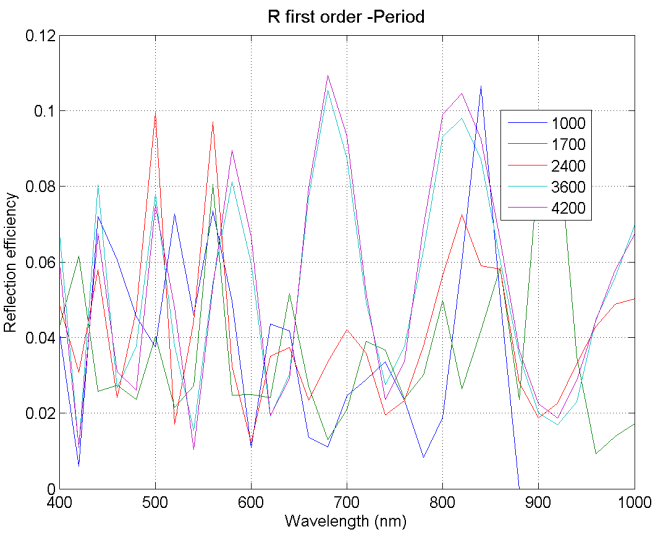
(q)
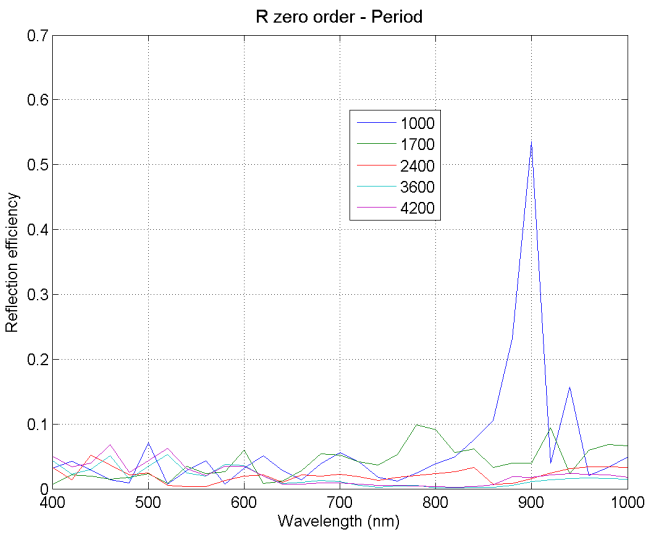
(r)
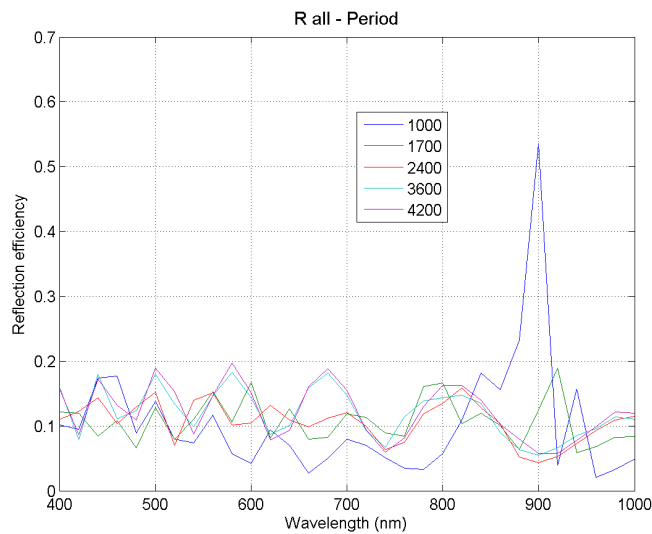
(s)
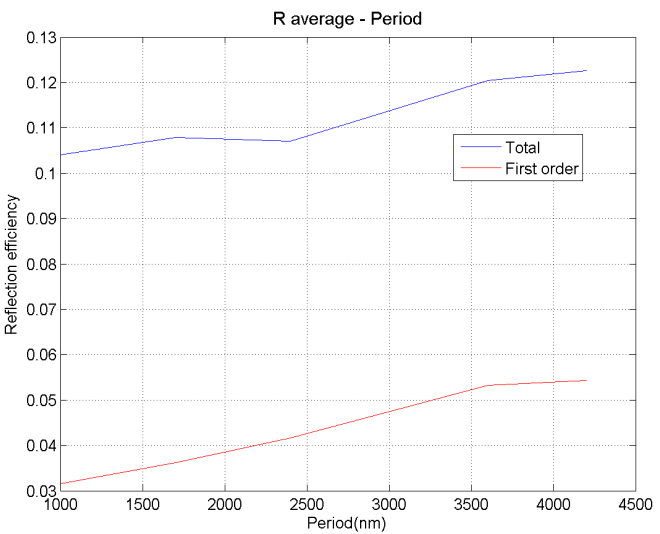
(t)

Diatom grating - Period - Transmission
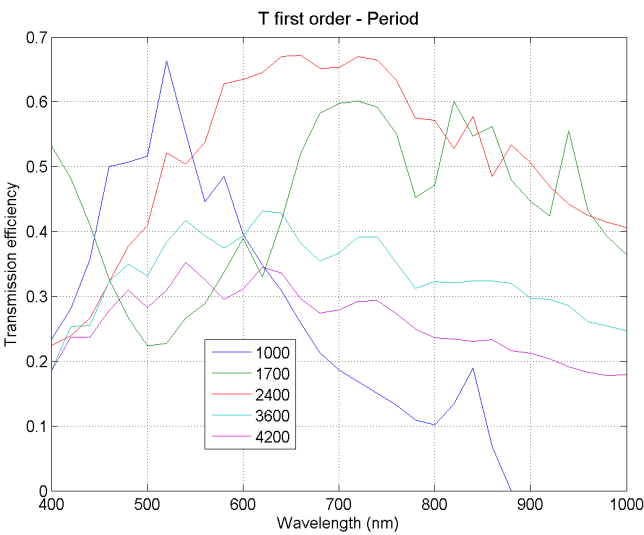
(u)
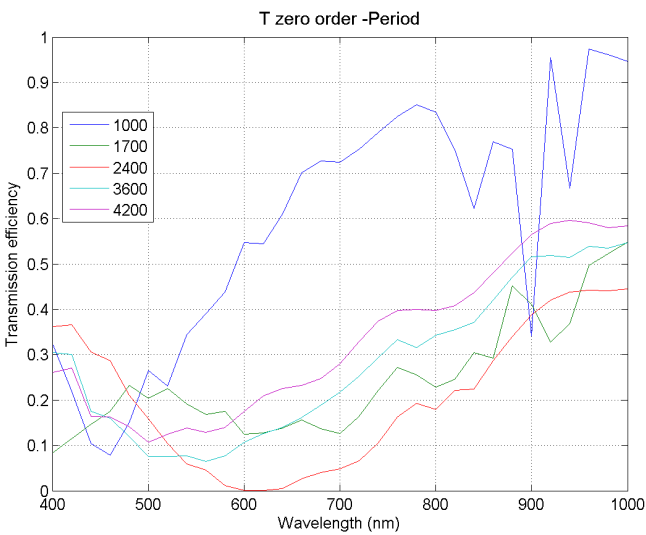
(v)
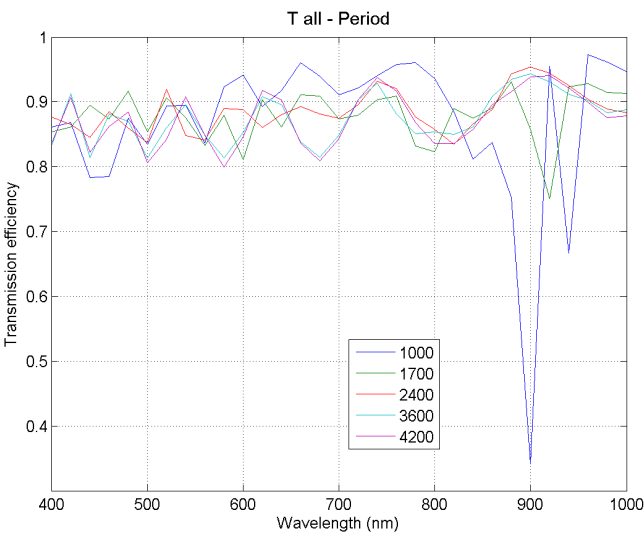
(w)
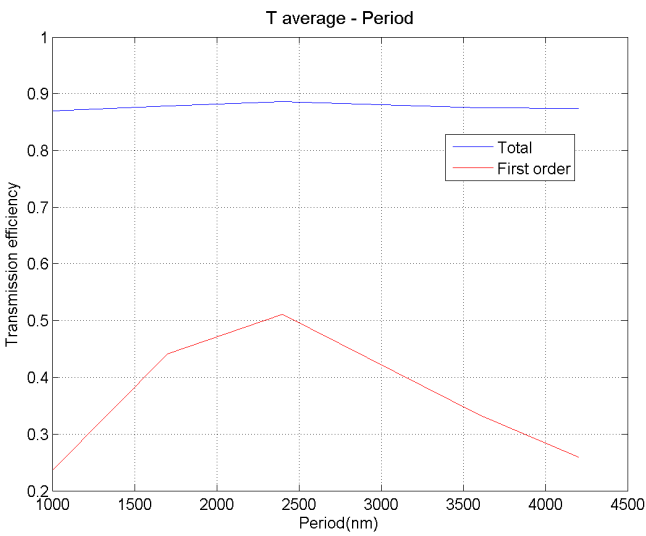
(x)

Diatom grating - Wall thickness - Reflection
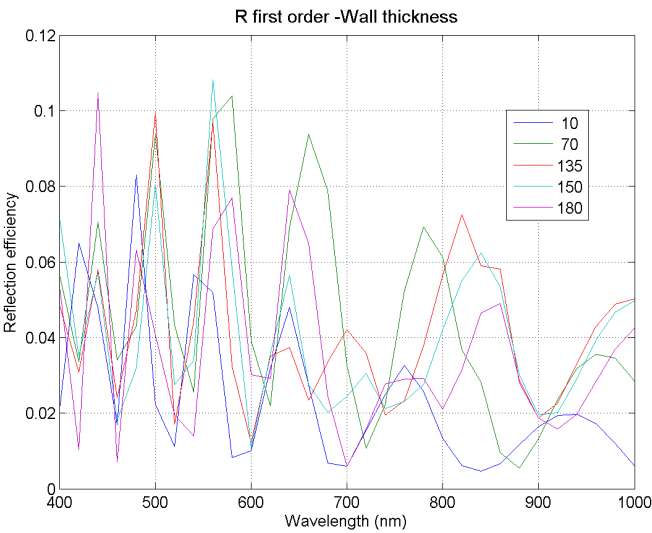
(y)
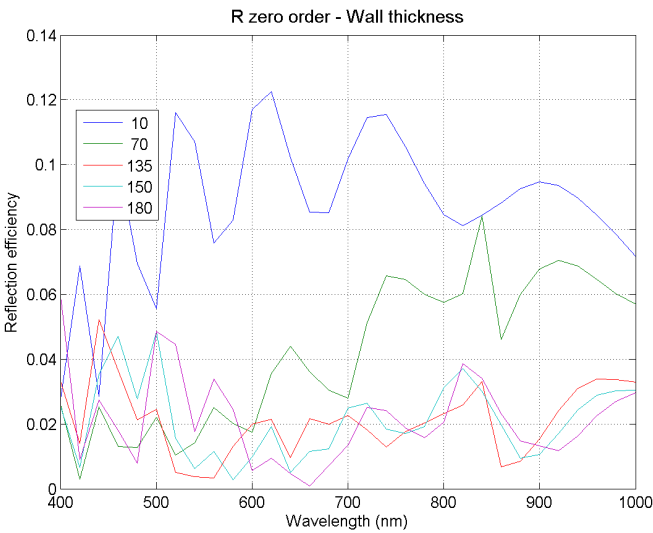
(z)

()

()
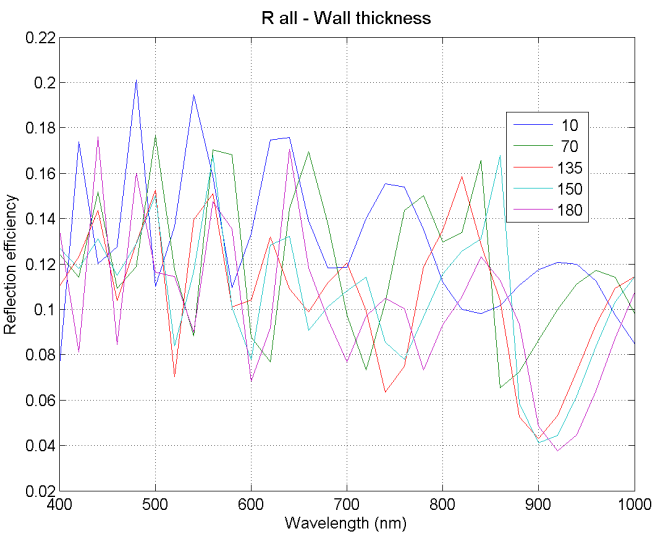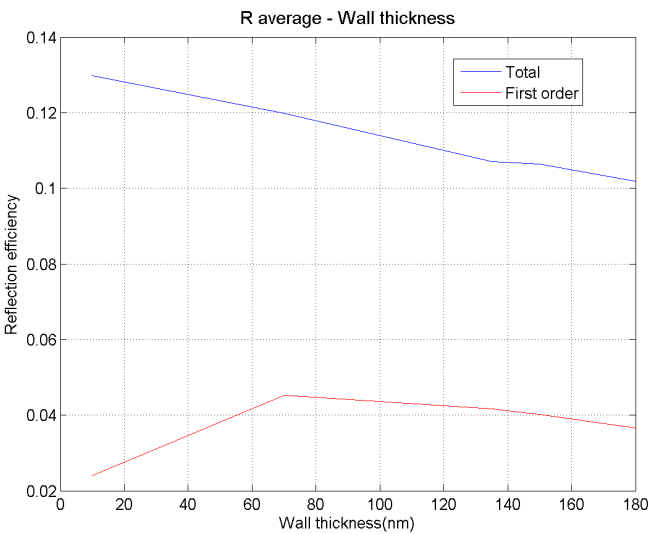
Diatom grating - Wall thickness - Transmission

()

()

()

()
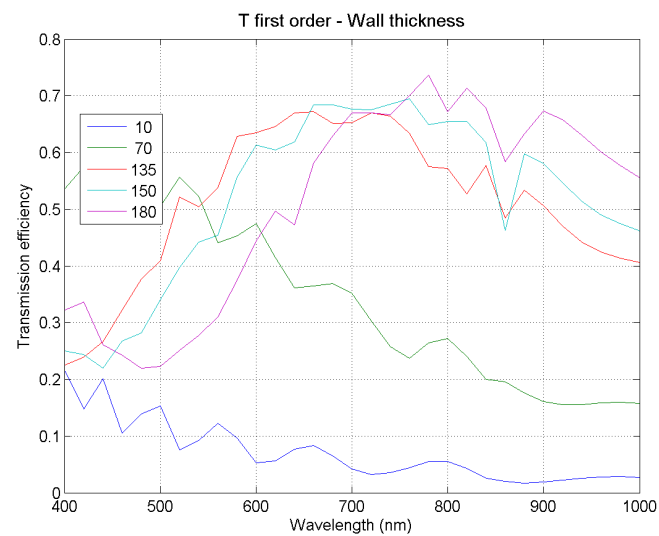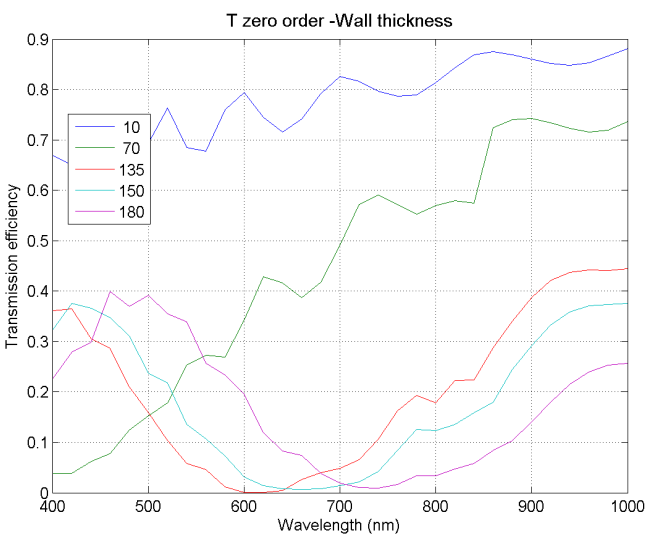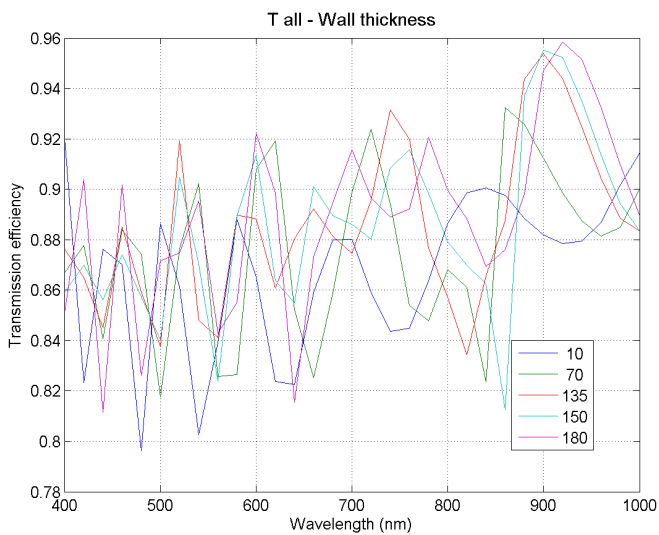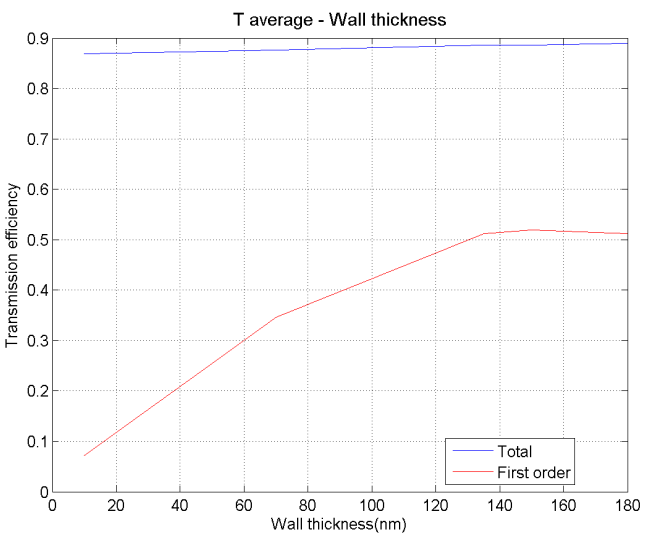
Diatom grating - Height of areola - Reflection

()

()

()

()
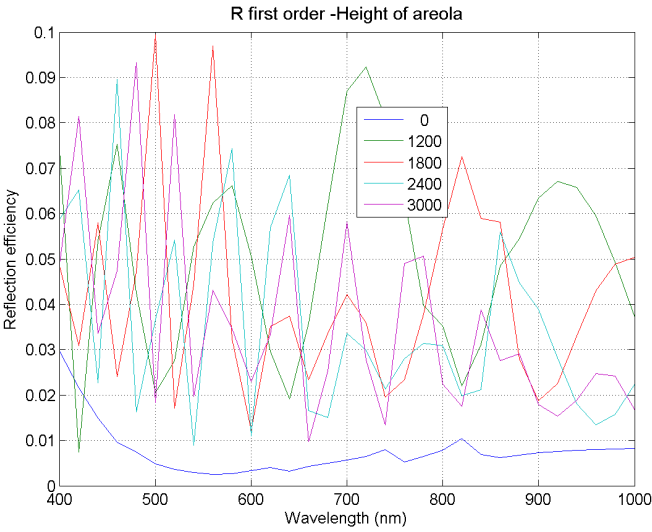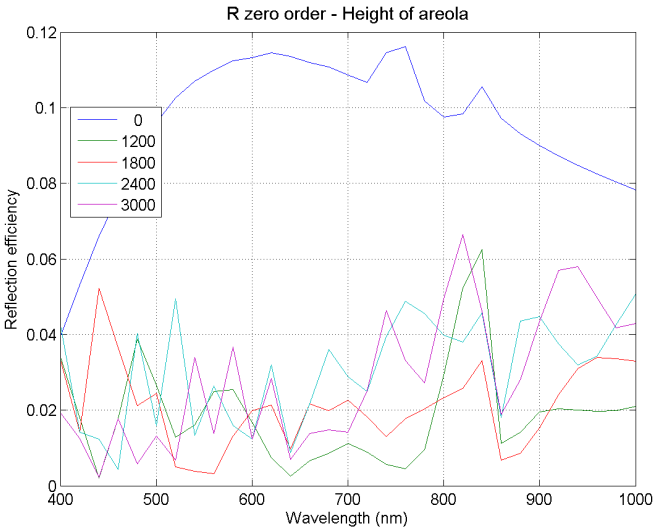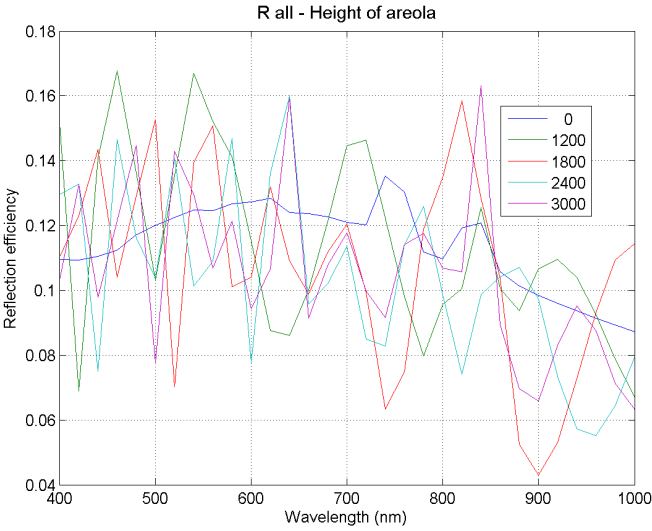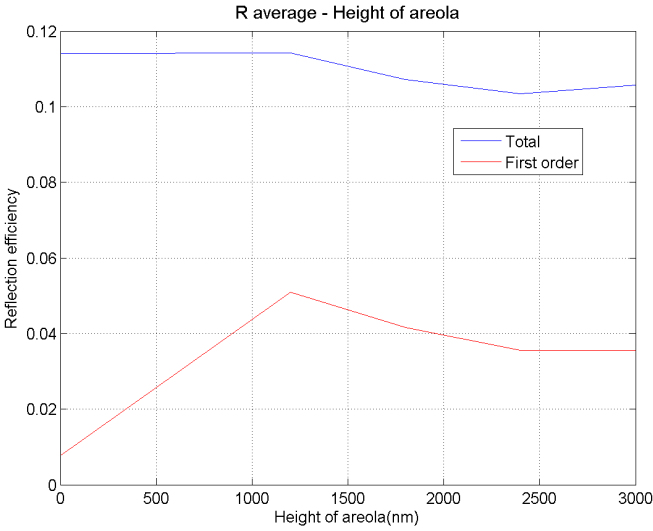
Diatom grating - Height of areolae - Transmission

()

()

()

()
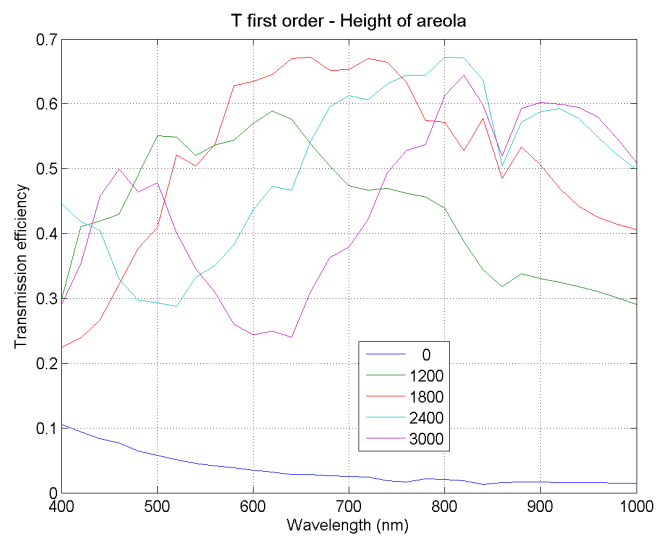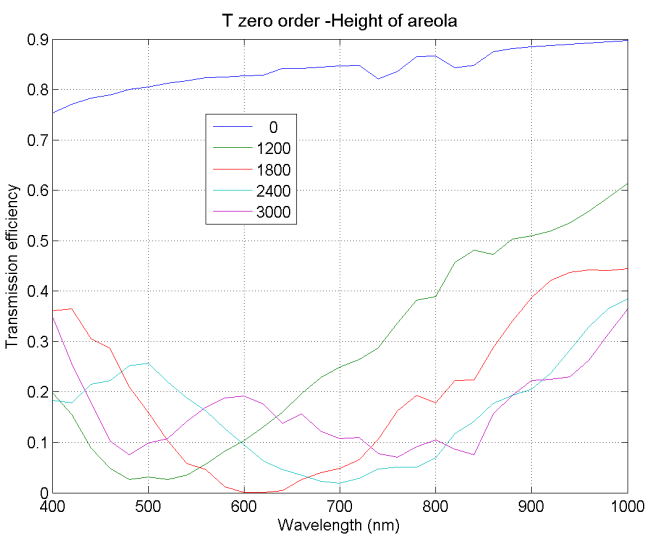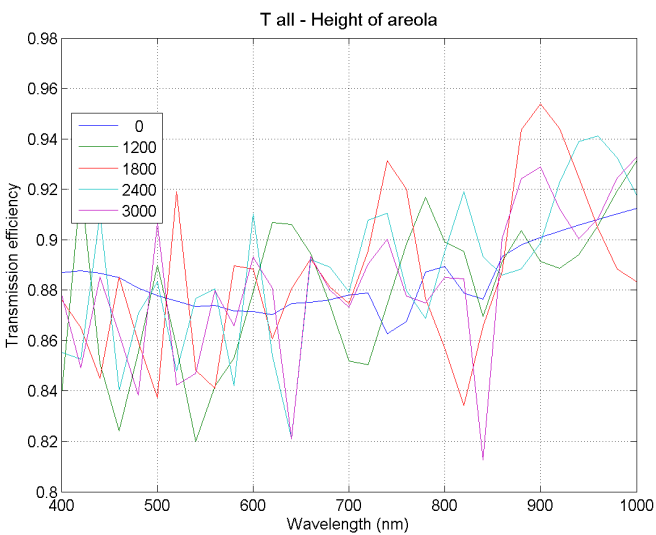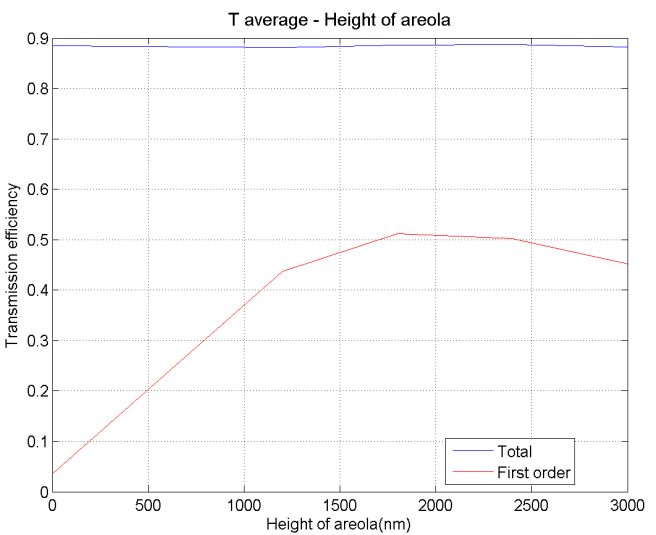
Anti-reflection structure

Anti-reflection - Radius of foramen - Reflection

()

()

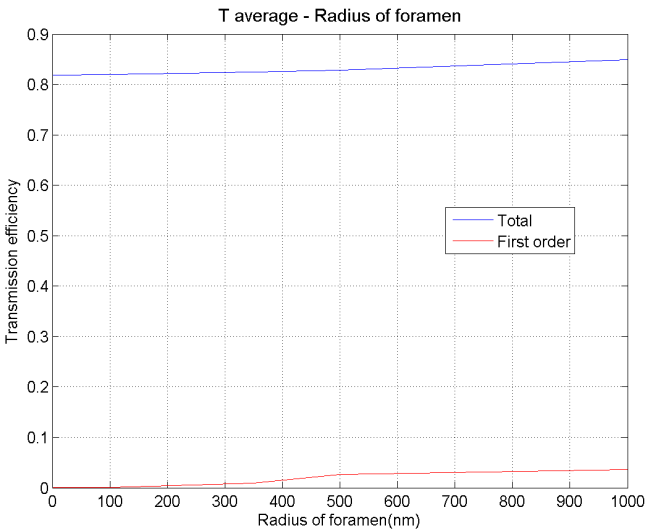()

()
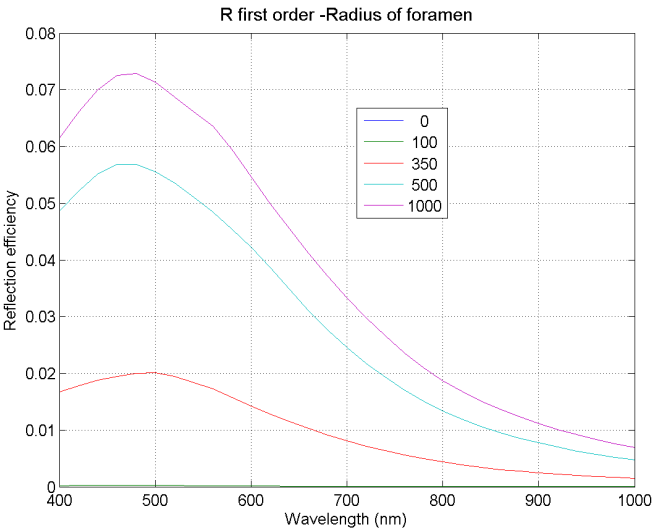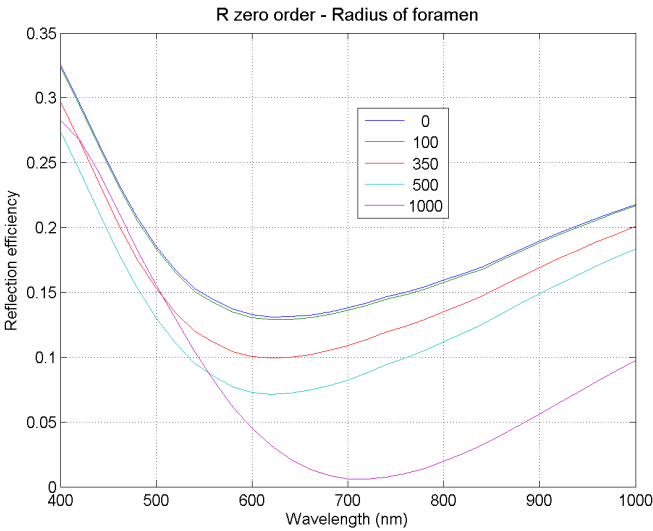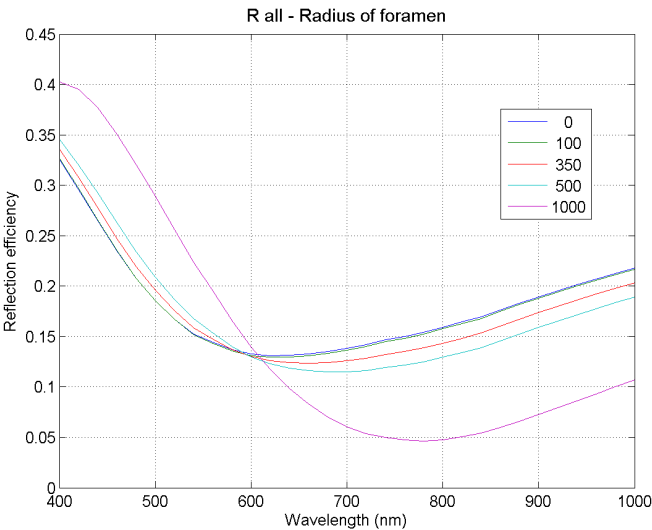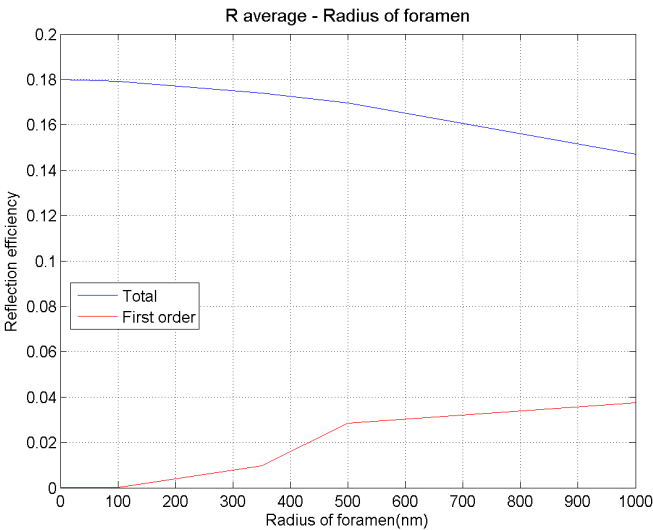
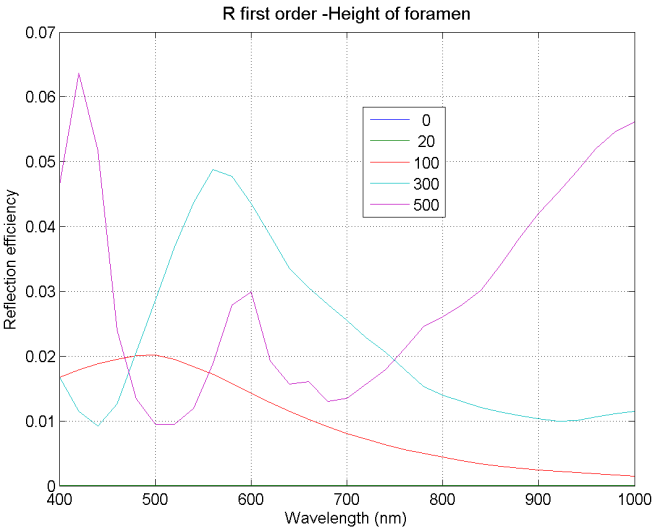# Anti-reflection - Radius of foramen - Transmission

()

()

()

()

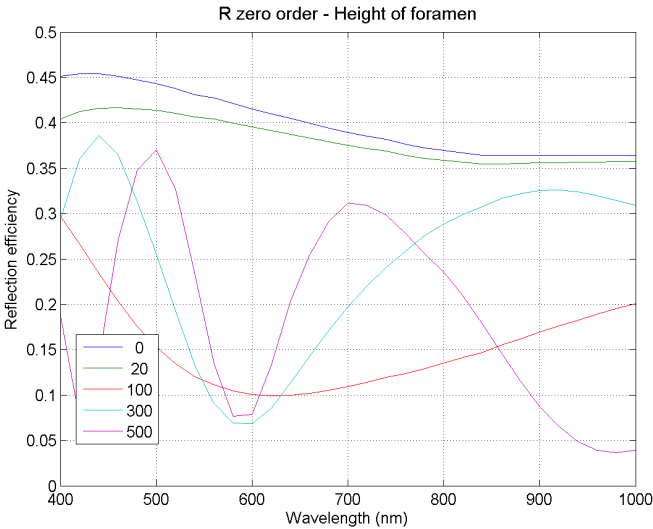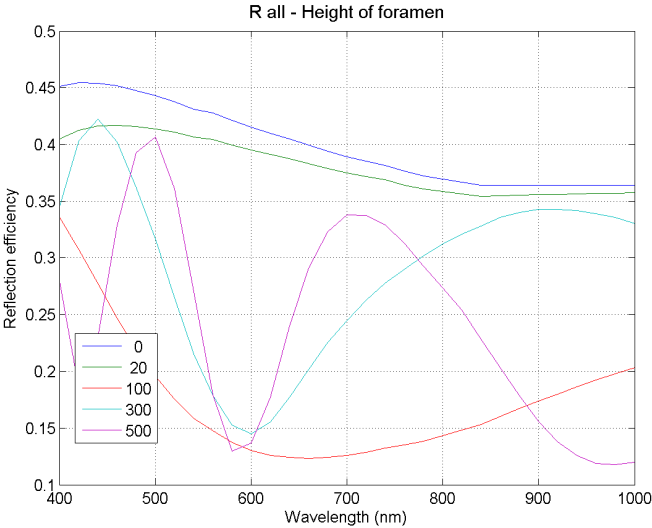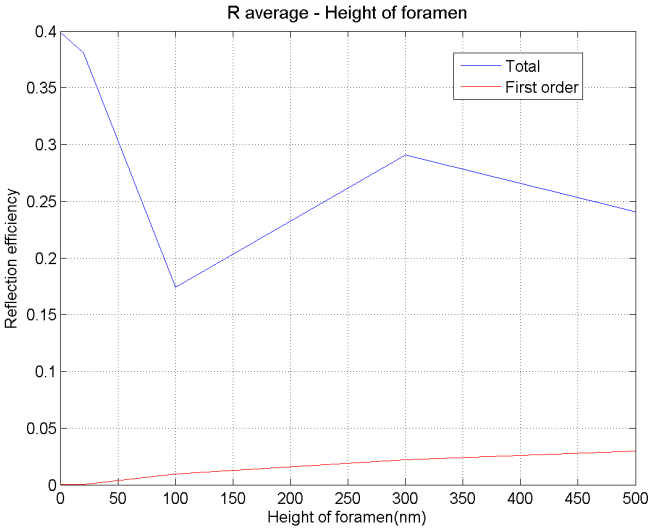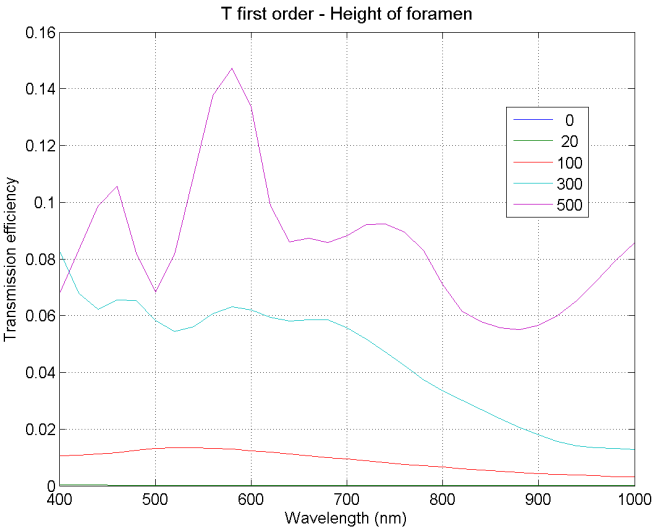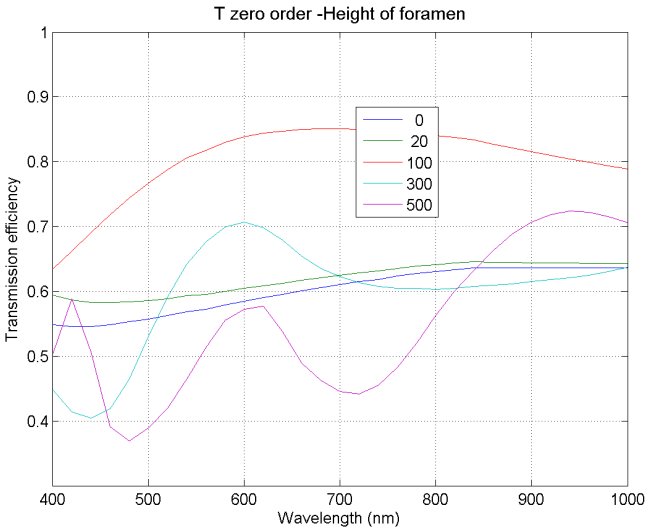# Anti-reflection - Height of foramen - Reflection

()

()

()

()
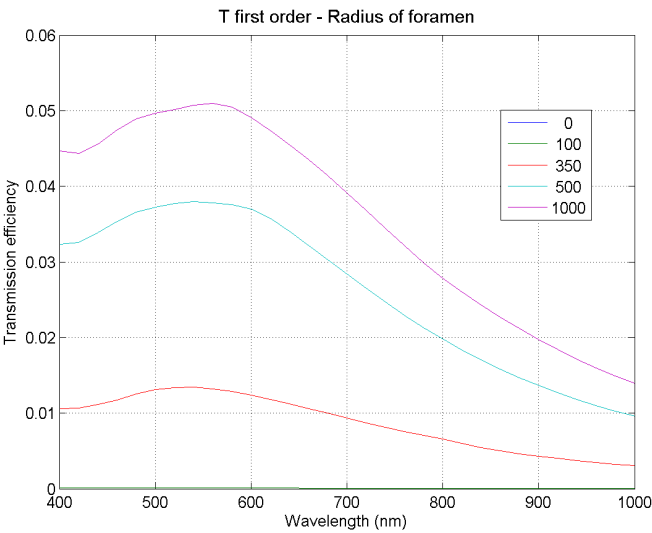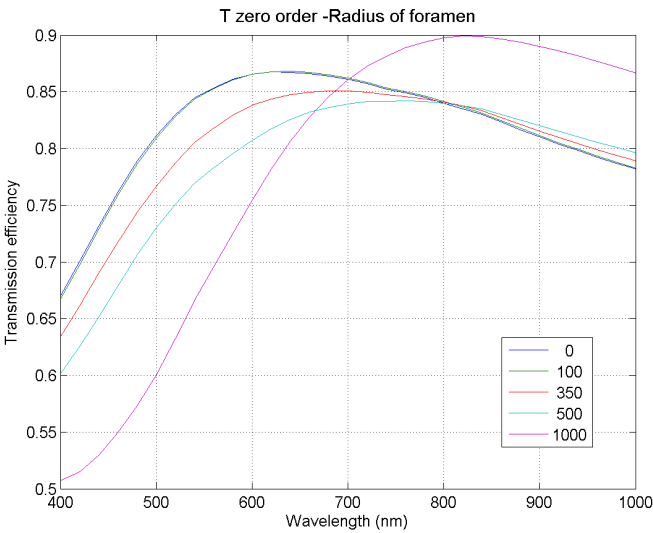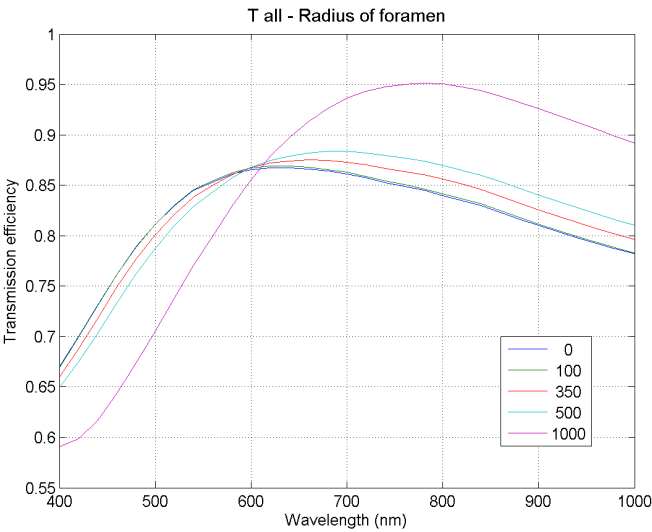
Anti-reflection - Height of foramen - Transmission
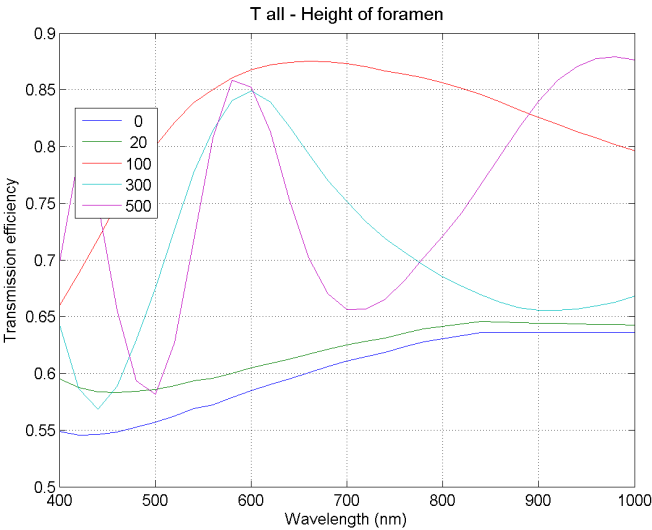
Anti-reflection - Period - Reflection
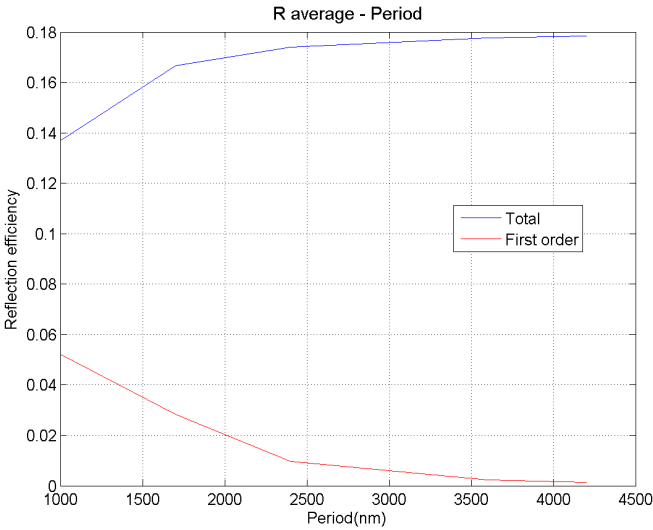
Anti-reflection - Period - Transmission

()

()

()

()

Back-side diffraction grating

Back-side diffraction grating - Radius of foramen - Reflection

()

()

()

()

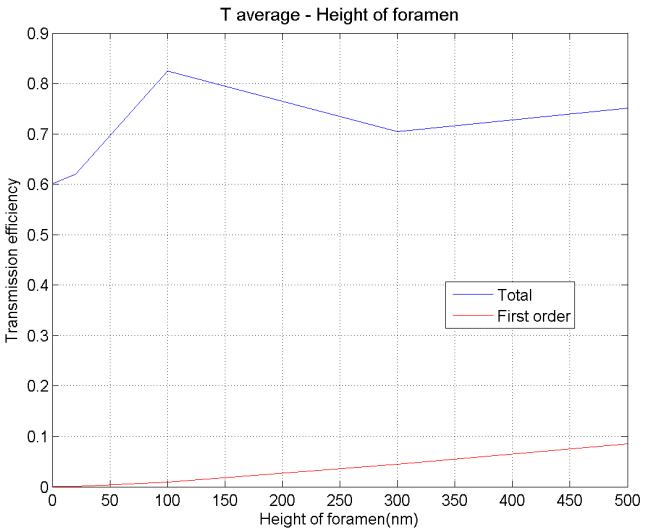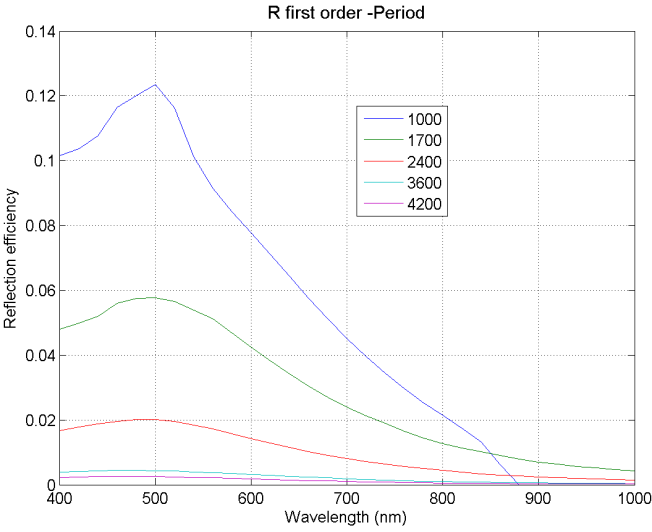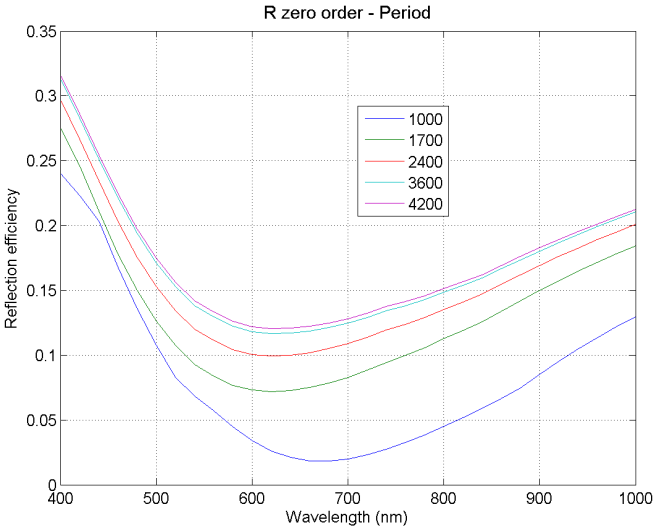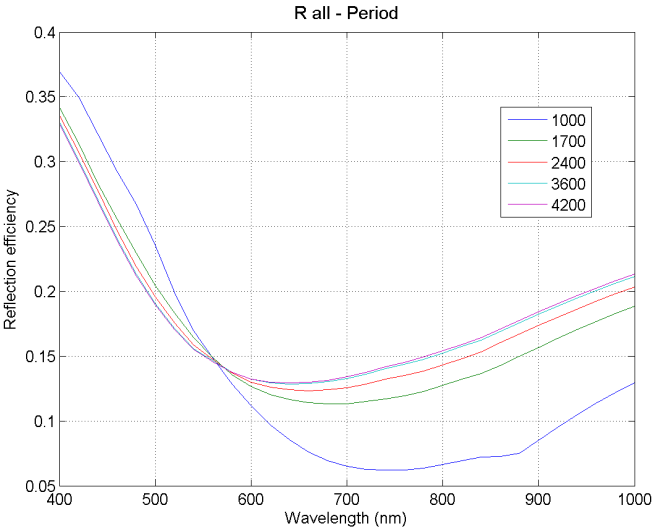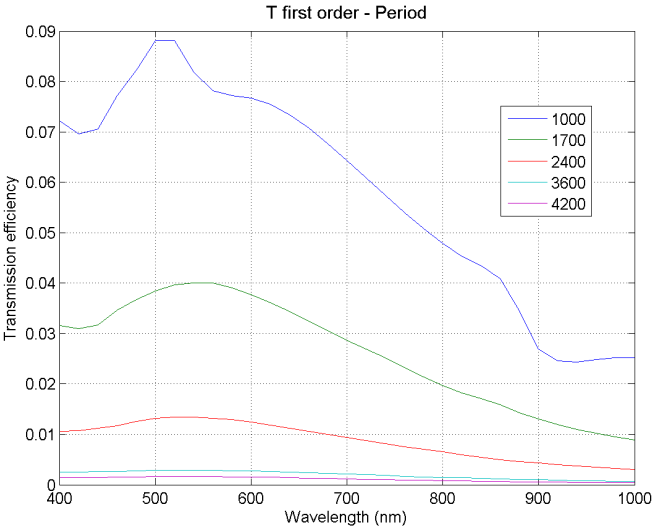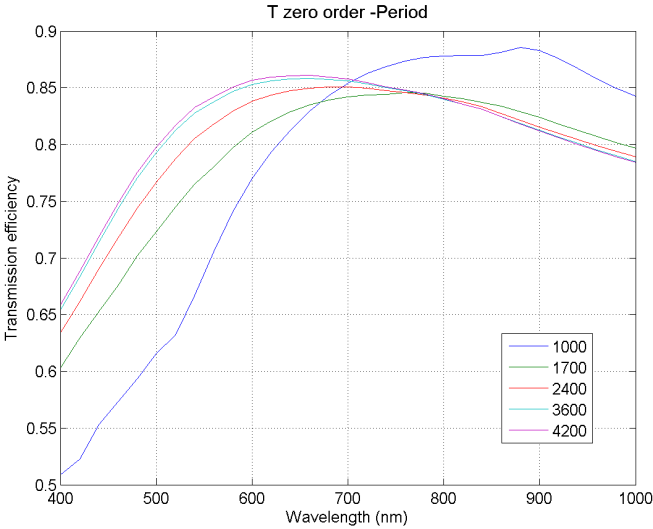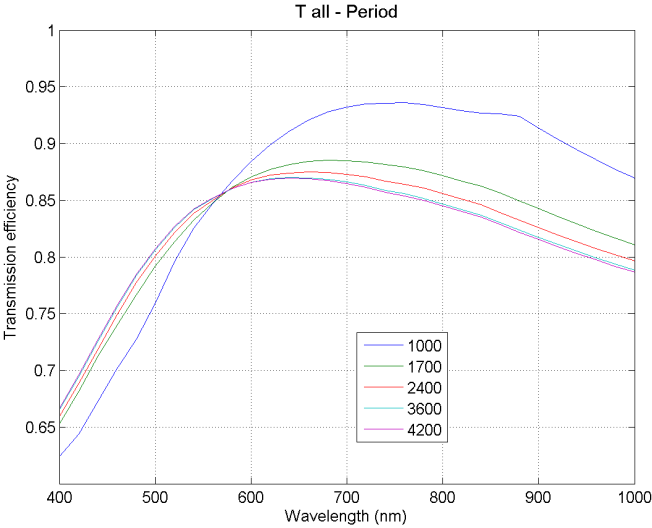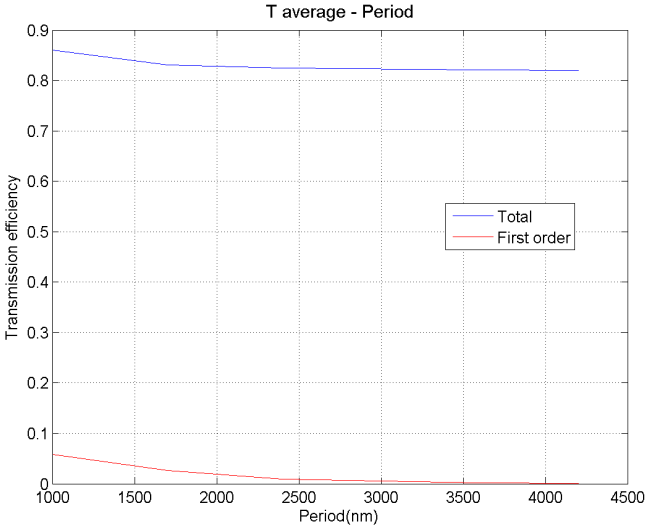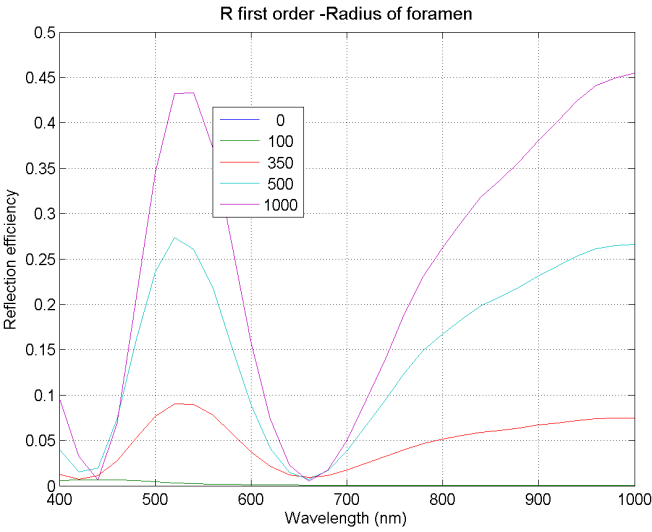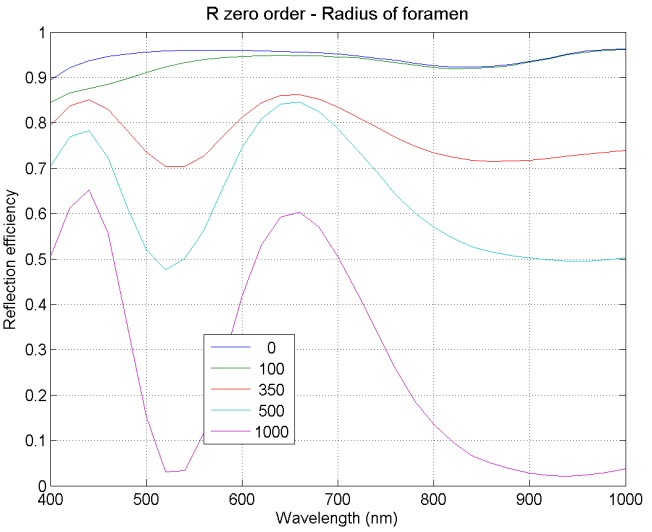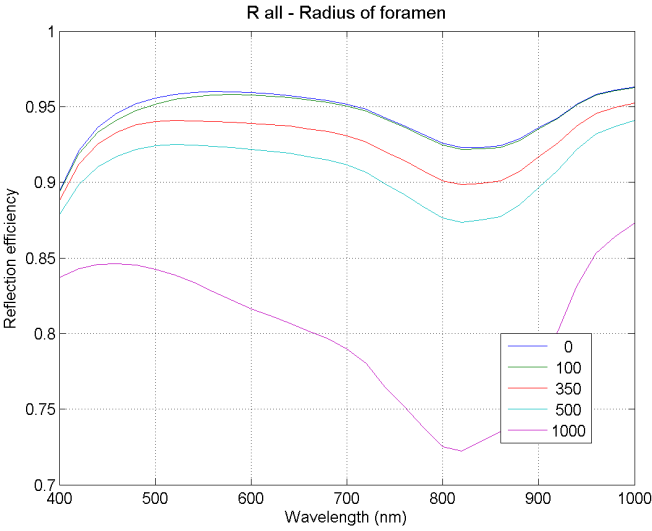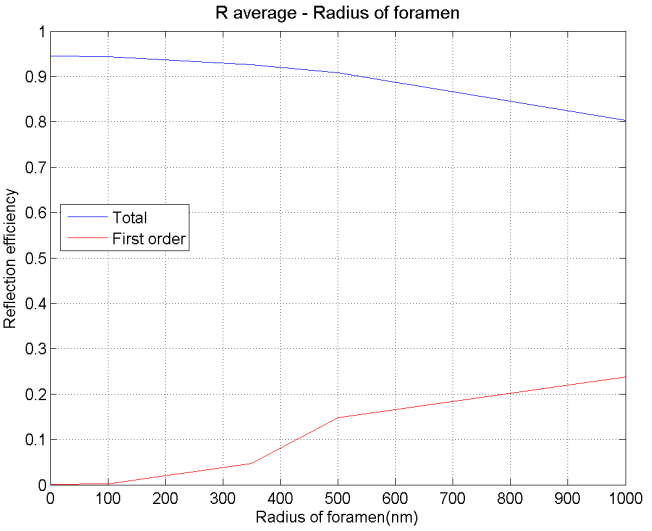# Back-side diffraction grating - Height of foramen - Reflection

()

()

()

()
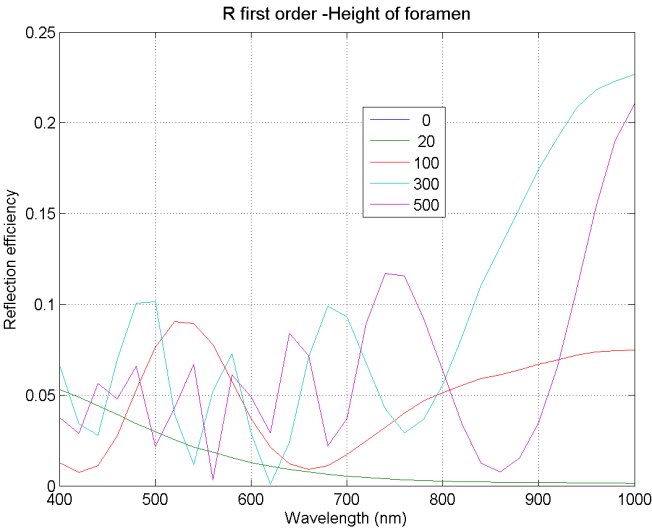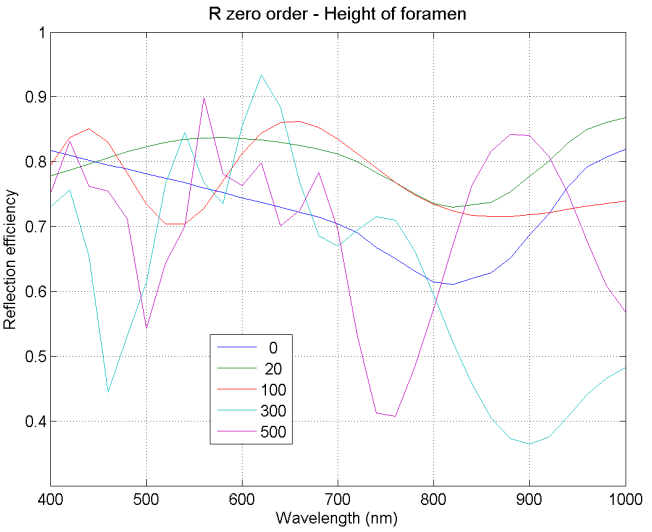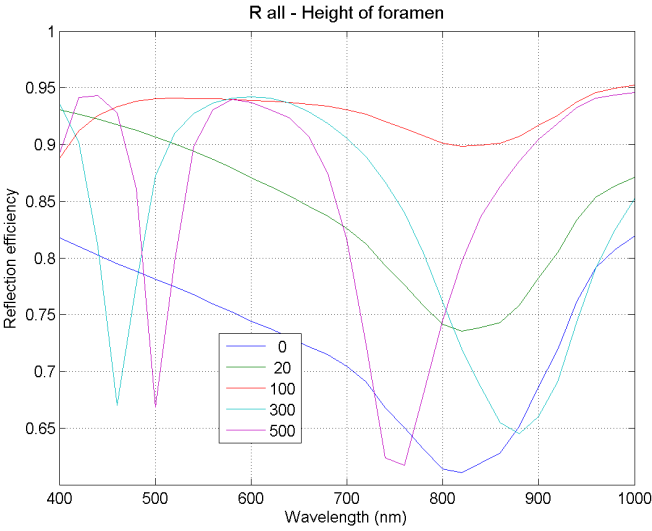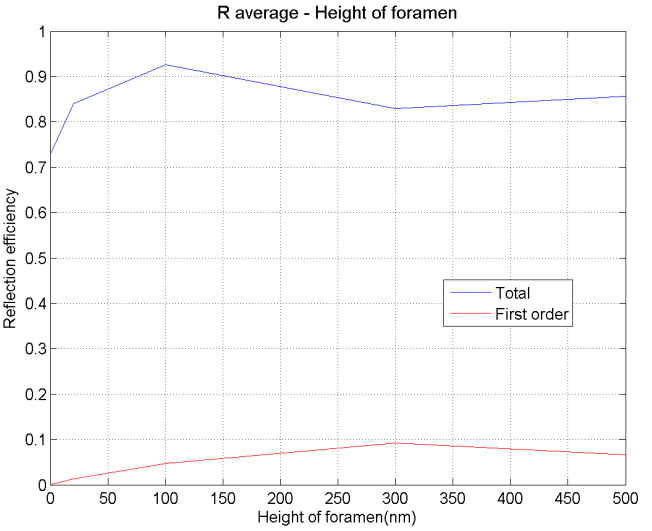
Back-side diffraction grating - Period - Reflection

()

()

()

()
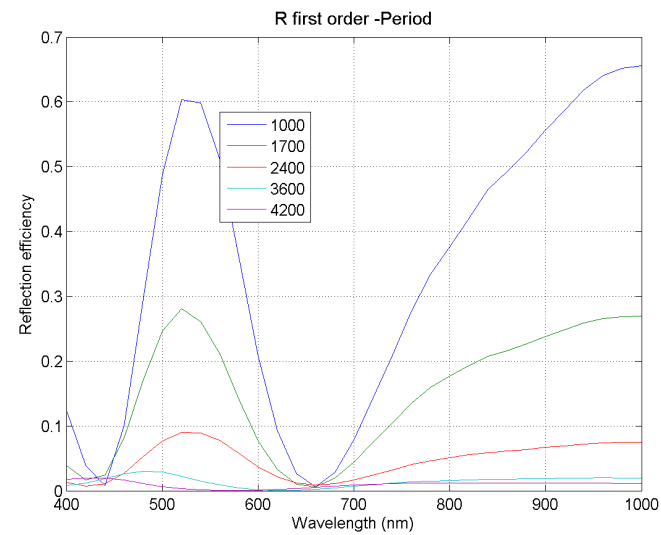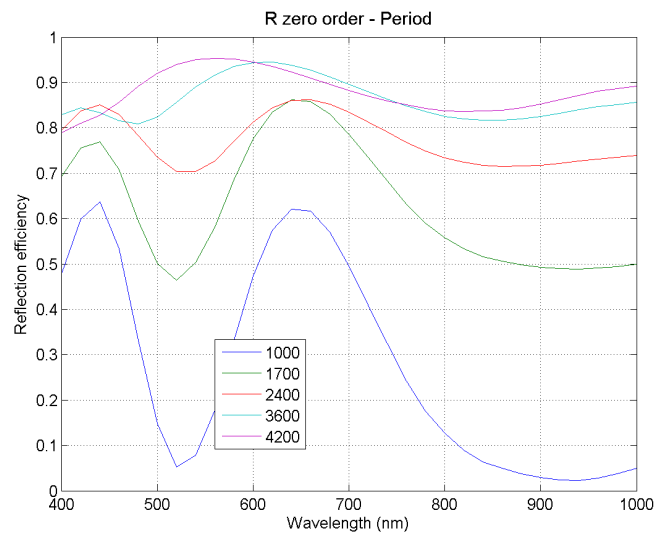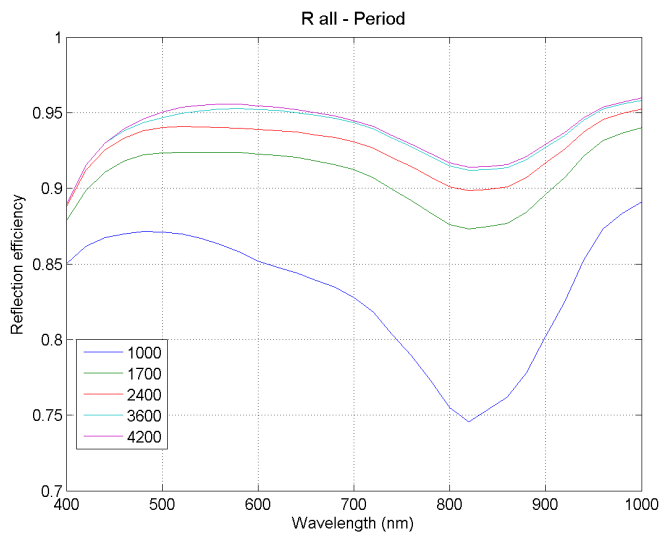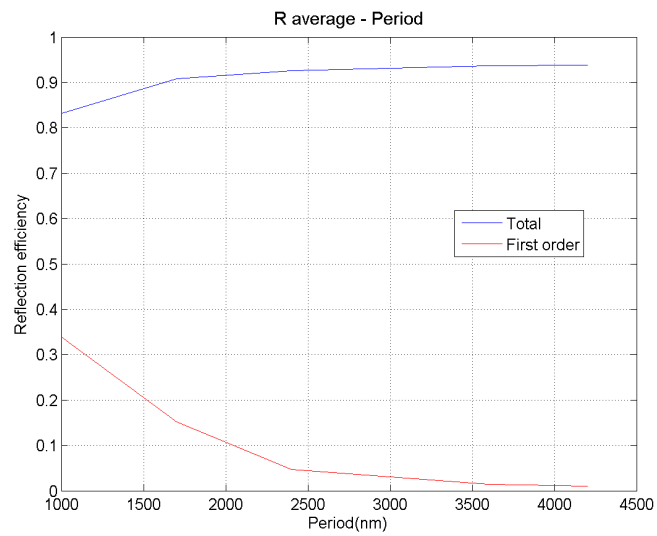
```matlab
%gdc_ak_diatom_simulering
%m file from demo 5
%
%Anne Kirsti Noren 28.04.2011

clear all

%Choices for plotting
plottgraf=1; % =1 Plot the resulting diffraction efficiency graphs
plotgrating=0; % =1 Plot the grating
plott=0; % =1 Plot the interpolation dispersion graphs

% Define parameters
demo=false; % true: run gdc_demo_engine; false: run gdc_engine
alt_stripe=1; % selector for alternate stripe orientation (1, 2, or 3)

%Incident field, orders, grating
wavelength_v=[400:20:1000]'; %wavelength vector
theta_v=[1 1 1 1 1]*pi/180; % angle of incident light wave
phi_v=[1 1 1 1 1]*pi/180; % angle of incident light wave
m_max=1;

%Refractive index calculation by interpolation or dispersion function
%SiO2
w_v=wavelength_v;
[eps_v, n_v, k_v]=ar_disp_lorenz(wavelength_v, 1, 2.12, 12, 0.1, 0);
ri_SiO2=eps_v;

%Si3N4
[eps_v, n_v, k_v]=ar_disp_lorenz(wavelength_v, 1, 4, 9, 0.1, 1);
ri_Si3N4=eps_v;

%Ag
Ag_index
filename=Ag_pal;
[nk_int_v, nk_all_v, w_all_v]=ar_wnk_interp(filename, w_v, plott);
ri_Ag=real(nk_int_v).^2;

%aSi - permittivity of aSi given by ri_aSi
ASi_index
filename=aSi_pal;
[nk_int_v, nk_all_v, w_all_v]=ar_wnk_interp(filename, wavelength_v, plott);
ri_aSi=real(nk_int_v).^2;

%Aluminium
Al_index
filename=al_pal;
[nk_int_v, nk_all_v, w_all_v]=ar_wnk_interp(filename, wavelength_v, plott);
ri_Al=(nk_int_v).^2;

%Allocating refractive index values to the grating.pmt positions
%Change to what ever fits for the specific setup
refractive_index_1=ri_SiO2;      %Diatom
refractive_index_2=ri_Si3N4;    %Inside porene
refractive_index_3=ri_aSi;      %Substrate
```

```matlab
refractive_index_4=1;              %Superstrate
refractive_index_5=0.2*ri_SiO2; %Inside the Cribrum

%Grating geometric parameters
% Radius of foramen
r=350; %Default value
%r=[0e-006 100 350 500 1000 ]; name1='Radius'; name2=r';

% Height of the areola layer
h1=100; %Default value
h1=[0e-006 20 100 300 500]; name1='Height'; name2=h1';

%Thickness of the areola wall
w=135; %Default value
%w=[10 70 135 150 180]; name1='Wall thickness'; name2=w';

%Height of the areola layer
h2=1800; %Default value
%h2=[0 1200 1800 2400 3000]; name1='Height grating'; name2=h2';

%Period
d=2400; %Periode default
%d=[1000 1700 2400 3600 4200]; name1='Period'; name2=d';

r2=d.*0.4; % Radius of cribrum
h3=50;   %The higth of the cribrum layer
h=2000; %Grating height

%Define number of stripes and blocks
N=8; % number of partition blocks per semicircle (for pillars)
%Define parameters for areola
N1=1; %number of stripes verical wall
N2=8; %number of stripes triangle
N3=16; %number of stripes in sloping wall
N4=8; %number of stripes in triangle

% Define parameters for the grating structure
zeta=30*pi/180;

%Define incident field and orders which are retained - from demo
gdc_ak_defineincidentfield

%Construct grating
gdc_ak_constructgrating

        % Create stratum resembeling the foramen layer
        stratum_nr=1;
        gdc_ak_stratum_foramen

        % Create stratum resembeling the areola layer
        stratum_nr=2;
        gdc_ak_stratum_areola

        Create stratum resembeling the cribrum layer
```

```matlab
        stratum_nr=3;
        gdc_ak_stratum_cribrum

% Run the diffraction calculations - from demo5
[param_size,scat_field,inc_field]=gdc(grating,inc_field,order);
if isempty(scat_field), disp('Interrupted by user.'); return, end

% Compute the diffraction efficiencies and sum of reflection and
% transmission efficiencies - partly from demo5
%[T_eff_all_m, T_eff_m, T_eff_00_m, T_eff_01all_m, T_eff_01sum_m, ...
%R_eff_all_m, R_eff_m, R_eff_00_m, R_eff_01all_m,
R_eff_01sum_m]=gdc_ak_eff(scat_field, inc_field);
gdc_ak_eff

if plottgraf==1;
%Plot the result
set(0,'DefaultFigureVisible','off')
if plottgraf==1
filename=(name1);
figure; plot(wavelength_v, R_eff_00_m), grid on, title(['R zero order - '
name1])
legend(num2str(name2), 'Location','best')
saveas(gcf, [name1 ' R zero order'] ,'fig')
saveas(gcf, [name1 ' R zero order'] ,'png')
figure; plot(wavelength_v, T_eff_00_m), grid on, title(['T zero order -'
name1])
legend(num2str(name2), 'Location','best')
saveas(gcf, [name1 ' T zero order' ] ,'fig')
saveas(gcf, [name1 ' T zero order' ] ,'png')
figure; plot(wavelength_v, R_eff_01sum_m), grid on, title(['R first order -'
name1])
legend(num2str(name2), 'Location','best')
saveas(gcf, [name1 ' R first order'] ,'fig')
saveas(gcf, [name1 ' R first order' ] ,'png')
figure; plot(wavelength_v, T_eff_01sum_m), grid on, title(['T first order - '
name1])
legend(num2str(name2), 'Location','best')
saveas(gcf, [name1 ' T first order'] ,'fig')
saveas(gcf, [name1 ' T first order'] ,'png')
figure; plot(wavelength_v, R_eff_sum_m), grid on, title(['R all - ' name1])
legend(num2str(name2), 'Location','best')
saveas(gcf, [name1 ' R all'] ,'fig')
saveas(gcf, [name1 ' R all'] ,'png')
figure; plot(wavelength_v, T_eff_sum_m), grid on, title(['T all - ' name1])
legend(num2str(name2), 'Location','best')
saveas(gcf, [name1 ' T all' ] ,'fig')
saveas(gcf, [name1 ' T all' ] ,'png')
figure; plot(name2', R_eff_avex2_m, name2', R_eff_ave_01, '-r'), grid on,
title(['R average - ' name1])
legend('Total', 'First order' , 'Location','best')
saveas(gcf, [name1 ' R ave' ] ,'fig')
saveas(gcf, [name1 ' R ave' ] ,'png')
figure; plot(name2', T_eff_avex2_m, name2', T_eff_ave_01, '-r'), grid on,
title(['T average - ' name1])
legend('Total', 'First order' , 'Location','best')
saveas(gcf, [name1 ' T ave' ] ,'fig')
```

```matlab
saveas(gcf, [name1 ' T ave' ] ,'png')
save temp
end

% Plot the grating
if plotgrating==1
x_limit=[-0.5*h,-1.5*d,-1.5*d;1.5*h,1.5*d,1.5*d];
h_plot=gdc_plot(grating,1,pmt_display,x_limit);
if ~isempty(h_plot)
    view(-45,45)
end
end
end
```

```matlab
function [nk_int_v, nk_all_v, w_all_v]=ar_wnk_interp(filename, wavelength_v, plott);
% loads refractive index from txt file and interpolates values for n and k
%
% AR 30.05.2011

% load txt file with three columns containing wavelength (nm), n and k
wnk=filename;

n_all_v = wnk(:,2);    % loaded n vector
k_all_v = wnk(:,3);    % loaded k vector
nk_all_v= n_all_v+1i*k_all_v;   %  complex loaded index
w_all_v = wnk(:,1);             %  loaded wavelength vector

n_int_v=interp1(w_all_v,n_all_v,wavelength_v) ;   % interpolated n vector
k_int_v=interp1(w_all_v,k_all_v,wavelength_v) ;    % interpolated k vector
nk_int_v= n_int_v+1i*k_int_v;              % interpolated complex index

if plott==1
figure(1), plot(w_all_v, n_all_v, w_all_v, k_all_v, wavelength_v, n_int_v, wavelength_v, k_int_v)
end
```

```matlab
function [eps_v, n_v, k_v]=ar_disp_lorenz(wavelength_v, eps_fin, eps_s,
omega_t, gamma_0, plott)
% calculates refractive index from dispersion constants
% use lorentz model for deltapsi2 ellipsometry software
% input w_v has unit nm,
%   eps is permittivity constants,  omega and gamma has unit eV,
%   gamma_0 must be zero for lossless real index
% example SiO2.dsp
%   [eps_v, n_v, k_v]=ar_disp_lorenz((400:100:1000)', 1, 2.12, 12, 0.1, 1);
% example Si3N4lz.dsp
%   [eps_v, n_v, k_v]=ar_disp_lorenz((400:100:1000)', 1, 5.377, 3.186,
%   1.787, 1);
%
% AR 31.05.2011

% convert nm to eV:
omega_v=1239.8./wavelength_v;
% Calculates dispersion relation
eps_v=eps_fin+((eps_s-eps_fin)*omega_t.^2)./((omega_t.^2)-
(omega_v.^2)+1i*gamma_0*omega_v);
eps_v=conj(eps_v);

n_v=real(sqrt(eps_v));
k_v=imag(sqrt(eps_v));

if plott==1
figure(1), plot(wavelength_v, n_v, wavelength_v, k_v), grid on, title('n and k
versus wavelength')
end
```

```matlab
%gdc_ak_defineincidentfield
%m file defining the incident field and specifying the diffraction
%orders which are to be retained.
%
%Anne Kirsti Noren 28.04.2011

% Define the indicent field.
clear inc_field
inc_field.wavelength=wavelength_v;
% f2 and f3 are the grating-tangential (x2 and x3) coordinate projections
% of the incident field's spatial-frequency vector. The grating-normal (x1)
% projection is implicitly f1=-cos(theta)/wavelength.
theta_m=repmat(theta_v, length(wavelength_v), 1);
phi_m=repmat(phi_v, length(wavelength_v), 1);
wavelength_m=repmat(wavelength_v,1, length(phi_v));
inc_field.f2=sin(theta_m).*cos(phi_m)./wavelength_m;
inc_field.f3=sin(theta_m).*sin(phi_m)./wavelength_m;

% Specify which diffracted orders are to be retained in the calculations.
% The orders are specified so that the retained diffracted orders' spatial
% frequencies form a hexagonal pattern such as that illustrated in
% GD-Calc.pdf, equations 4.13 and 4.14 and Figure 5.
order=[];
for m2=-m_max:m_max
    order(end+1).m2=m2;
    m1=-m_max:m_max;
    % The following line implicitly applies rectangular index truncation
    % with a different unit cell.
    m1=m1(abs(m1-m2)<=m_max);
    order(end).m1=m1;
end
```

```matlab
%gdc_ak_constructgrating
%m file for creating grating
%
%Anne Kirsti Noren 28.04.2011

clear grating
grating.pmt={refractive_index_1, refractive_index_2, refractive_index_3,
refractive_index_4, refractive_index_5;}; %
grating.pmt_sub_index=3; % substrate permittivity index
grating.pmt_sup_index=4; % superstrate permittivity index
zeta=30*pi/180;
grating.d21=d*sin(zeta);
grating.d31=d*cos(zeta);
grating.d22=d;
grating.d32=0;

pmt_display(1).name='';%Silica';
pmt_display(1).color=[0.7, 0.7, 0.7];
pmt_display(1).alpha=1;
pmt_display(2).name='Air';
pmt_display(2).color=[];
pmt_display(2).alpha=1;
pmt_display(3).name='';
pmt_display(3).color=[];%[0.3,0.7,0.7];
pmt_display(3).alpha=1;
pmt_display(4).name='';
pmt_display(4).color=[];%[0.4,0,0.3];
pmt_display(4).alpha=1;
pmt_display(5).name='';%'Silica and air';
pmt_display(5).color=[0.9,0.9,0.9];
pmt_display(5).alpha=1;
```

```matlab
%gdc_ak_stratum_foramen
%stratum from demo 5
%
%Anne Kirsti Noren 28.04.2011

clear stratum
stratum.type=2;
stratum.thick=h1;

if alt_stripe==1
        % Stripes are parallel to [grating.d22,grating.d32].
        stratum.h11=1;
        stratum.h12=0;
        stratum.h21=0;
        stratum.h22=1;
    elseif alt_stripe==2
        % Stripes are parallel to [grating.d21,grating.d31].
        stratum.h11=1;
        stratum.h12=0;
        stratum.h21=0;
        stratum.h22=1;
    else % alt_stripe==3
        % Stripes are parallel to
        % [grating.d21,grating.d31]-[grating.d22,grating.d32].
        stratum.h11=1;
        stratum.h12=1;
        stratum.h21=0;
        stratum.h22=-1;
    end

x=circle_partition(N);
    clear stripe block
    stripe.type=1; % inhomogeneous stripe
    % The x2, x3 coordinate origin is at the center of a pillar.
    for n=1:N
        if n<N
            % The next stripe intercepts a row of pillars between the x3
            % coordinate limits -x(n)*r and -x(n+1)*r.
            stripe.c1=-x(n+1).*r./grating.d31;
        else
            % The N-th stripe is centered on the pillar axes, and its x3
            % limits are -x(N)*r and +x(N)*r.
            stripe.c1=x(N).*r./grating.d31;
        end
        % The first block defines the open space between adjacent pillars.
        % The block's x2 coordinate limits are x(N+1-n)*r-d and
        % -x(N+1-n)*r.
        block.c2=(-x(N+1-n).*r-stripe.c1.*grating.d21)./d;
        block.pmt_index=1;
        stripe.block{1}=block;
        % The second block traverses the pillar interior. Its x2 coordinate
        % limits are -x(N+1-n)*r and +x(N+1-n)*r.
        block.c2=(x(N+1-n).*r-stripe.c1.*grating.d21)./d;
        block.pmt_index=2;
        stripe.block{2}=block;
        stratum.stripe{n}=stripe;
```

```matlab
    end
    for n=2:N
        % The next stripe intercepts a row of pillars between the x3
        % coordinate limits x(N+2-n)*r and x(N+1-n)*r.
        stripe.c1=x(N+1-n).*r./grating.d31;
        % The first block defines the open space between adjacent pillars.
        % The block's x2 coordinate limits are x(n)*r-d and -x(n)*r.
        block.c2=(-x(n).*r-stripe.c1.*grating.d21)./d;
        block.pmt_index=1;
        stripe.block{1}=block;
        % The second block traverses the pillar interior. Its x2 coordinate
        % limits are -x(n)*r and +x(n)*r.
        block.c2=(x(n).*r-stripe.c1.*grating.d21)./d;
        block.pmt_index=2;
        stripe.block{2}=block;
        stratum.stripe{N+n-1}=stripe;
    end
    clear stripe
    % The next stripe defines the open space between adjacent rows of
    % pillars. Its x3 coordinate limits are x(1)*r and grating.d31-x(1)*r.
    stripe.type=0; % homogeneous stripe
    stripe.c1=1-x(1).*r./grating.d31;
    stripe.pmt_index=1;
    stratum.stripe{2*N}=stripe;
    clear stripe
    grating.stratum(stratum_nr)={stratum};

    clear stratum
```

```matlab
%gdc_ak_stratum_honeycomb
%m file for creating a stratum mimicing the honeycombstructure of
%coscinodiscus.
%
%Anne Kirsti Noren 28.04.2011


    clear stratum
    stratum.type=2;
    stratum.thick=h2;
    b=w./2;
    if alt_stripe==1
        % Stripes are parallel to [grating.d22,grating.d32].
        stratum.h11=1;
        stratum.h12=0;
        stratum.h21=0;
        stratum.h22=1;
    else
        % Stripes are parallel to [grating.d21,grating.d31].
        stratum.h11=0;
        stratum.h12=1;
        stratum.h21=1;
        stratum.h22=0;
    end

    cos_1=1/2/cos(zeta); % =5/sqrt(75)
    cos_2=1/cos(zeta); % =10/sqrt(75)

  % Part 1 - Straight wall
    clear stripe block
    stripe.type=1;
    x1=(d./2-b);
    x2=(d./2+b);
    y1=d./sqrt(12)-b*sqrt(3/4);
    block.c2=(x1-y1*cos_1)./d;
    block.pmt_index=2;
    stripe.block{1}=block;
    block.c2=(x2-y1*cos_1)./d;
    block.pmt_index=1;
    stripe.block{2}=block;
    clear block
    stripe.c1=(y1*cos_2)./d;
    stratum.stripe{N1}=stripe;

  % Part 2 - First triangle
    clear stripe block
    for n=1:N2
        stripe.type=1;
        x1=(d./2-b-w.*3/2*n/N2);
        x2=(d./2+b+w.*3/2*n/N2);
        y2=d/sqrt(12)-b*sqrt(3/4)+(2*b*sqrt(3/4))*n/N2;

        block.c2=(x1-y2*cos_1)./d;
        block.pmt_index=2;
        stripe.block{1}=block;

        block.c2=(x2-y2*cos_1)./d;
```

```matlab
        block.pmt_index=1;
        stripe.block{2}=block;

        stripe.c1=(y2*cos_2)./d;
        stratum.stripe{n+N1}=stripe;
    end

  % Part 3 - Sloping wall
    clear stripe block
    for n=1:N3
        stripe.type=1;
        x1=1+(d./2-b-w*3/2)*(1-n/N3); % 1+ to make sure the block do not
overlapp with block 4.
        x2=4*b+(d./2-b-w*3/2)*(1-n/N3);
        x3=d./2+(d./2-b-w*3/2)*n/N3;
        x4=d./2+b+w*3/2+(d/2-b-w*3/2)*n/N3;
        y3=d./sqrt(12)+b*sqrt(3/4)+(d./sqrt(12)-2*b*sqrt(3/4))*n/N3;

        block.c2=(x1-y3*cos_1)./d;
        block.pmt_index=2;
        stripe.block{1}=block;

        block.c2=(x2-y3*cos_1)./d;
        block.pmt_index=1;
        stripe.block{2}=block;

        block.c2=(x3-y3*cos_1)./d;
        block.pmt_index=2;
        stripe.block{3}=block;

        block.c2=(x4-y3*cos_1)./d;
        block.pmt_index=1;
        stripe.block{4}=block;

        stripe.c1=(y3*cos_2)./d;
        stratum.stripe{n+N1+N2}=stripe;
    end

  % Part 4 - Second triangle
    clear stripe block
    for n=1:N4
        stripe.type=1;
        x1=(d-b-w*3/2*(1-n/N4));
        x2=(d+b+w*3/2*(1-n/N4));
        y4=d./sqrt(12)+d./sqrt(12)-b.*sqrt(3/4)+(2.*b*sqrt(3/4))*n/N4;

        block.c2=(x1-y4*cos_1)./d;
        block.pmt_index=2;
        stripe.block{1}=block;

        block.c2=(x2-y4*cos_1)./d;
        block.pmt_index=1;
        stripe.block{2}=block;

        stripe.c1=(y4*cos_2)./d;
```
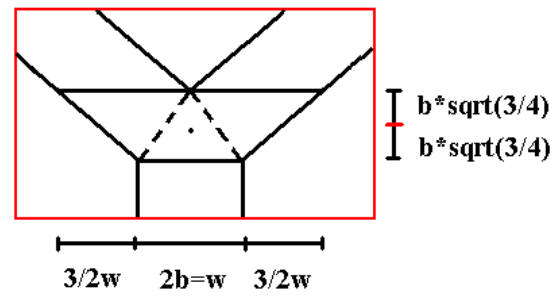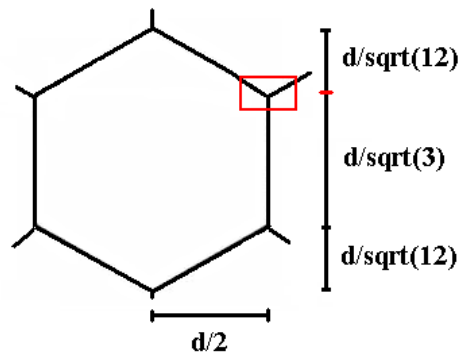
```
        stratum.stripe{n+N1+N2+N3}=stripe;
end
 grating.stratum(stratum_nr)={stratum};
 clear stratum
```


d/sqrt(12)

d/sqrt(3)

d/sqrt(12)

d/2

b*sqrt(3/4)

b*sqrt(3/4)

3/2w   2b=w   3/2w

```matlab
%gdc_ak_cribrum
%m file from demo 5
%
%Anne Kirsti Noren 28.04.2011

clear stratum
stratum.type=2;
stratum.thick=h3;

if alt_stripe==1
        % Stripes are parallel to [grating.d22,grating.d32].
        stratum.h11=1;
        stratum.h12=0;
        stratum.h21=0;
        stratum.h22=1;
    elseif alt_stripe==2
        % Stripes are parallel to [grating.d21,grating.d31].
        stratum.h11=1;
        stratum.h12=0;
        stratum.h21=0;
        stratum.h22=1;
    else % alt_stripe==3
        % Stripes are parallel to
        % [grating.d21,grating.d31]-[grating.d22,grating.d32].
        stratum.h11=1;
        stratum.h12=1;
        stratum.h21=0;
        stratum.h22=-1;
    end

x=circle_partition(N);
    clear stripe block
    stripe.type=1; % inhomogeneous stripe
    % The x2, x3 coordinate origin is at the center of a pillar.
    for n=1:N
        if n<N
            % The next stripe intercepts a row of pillars between the x3
            % coordinate limits -x(n)*r and -x(n+1)*r.
            stripe.c1=-x(n+1).*r2./grating.d31;
        else
            % The N-th stripe is centered on the pillar axes, and its x3
            % limits are -x(N)*r and +x(N)*r.
            stripe.c1=x(N).*r2./grating.d31;
        end
        % The first block defines the open space between adjacent pillars.
        % The block's x2 coordinate limits are x(N+1-n)*r-d and
        % -x(N+1-n)*r.
        block.c2=(-x(N+1-n).*r2-stripe.c1.*grating.d21)./d;
        block.pmt_index=1;
        stripe.block{1}=block;
        % The second block traverses the pillar interior. Its x2 coordinate
        % limits are -x(N+1-n)*r and +x(N+1-n)*r.
        block.c2=(x(N+1-n).*r2-stripe.c1.*grating.d21)./d;
        block.pmt_index=5;
        stripe.block{2}=block;
        stratum.stripe{n}=stripe;
```

```matlab
    end
    for n=2:N
        % The next stripe intercepts a row of pillars between the x3
        % coordinate limits x(N+2-n)*r and x(N+1-n)*r.
        stripe.c1=x(N+1-n).*r2./grating.d31;
        % The first block defines the open space between adjacent pillars.
        % The block's x2 coordinate limits are x(n)*r-d and -x(n)*r.
        block.c2=(-x(n).*r2-stripe.c1.*grating.d21)./d;
        block.pmt_index=1;
        stripe.block{1}=block;
        % The second block traverses the pillar interior. Its x2 coordinate
        % limits are -x(n)*r and +x(n)*r.
        block.c2=(x(n).*r2-stripe.c1.*grating.d21)./d;
        block.pmt_index=5;
        stripe.block{2}=block;
        stratum.stripe{N+n-1}=stripe;
    end
    clear stripe
    % The next stripe defines the open space between adjacent rows of
    % pillars. Its x3 coordinate limits are x(1)*r and grating.d31-x(1)*r.
    stripe.type=0; % homogeneous stripe
    stripe.c1=1-x(1).*r2./grating.d31;
    stripe.pmt_index=1;
    stratum.stripe{2*N}=stripe;
    clear stripe
    grating.stratum(stratum_nr)={stratum};
    clear stratum
```

```matlab
%function [T_eff_all_m, T_eff_m, T_eff_00_m, T_eff_01all_m, T_eff_01sum_m, ...
    % R_eff_all_m, R_eff_m, R_eff_00_m, R_eff_01all_m, R_eff_01sum_m] ...
    %=gdc_ak_eff(scat_field, inc_field, max_length_vector)

%T_eff_all_m
%T_eff_m
%T_eff_00_m
%T_eff_01all_m
%T_eff_01sum_m

[len1, len2]=size(scat_field(1).f1r);
len3=length(scat_field);
m1_v=[scat_field.m1];
m2_v=[scat_field.m2];
wavelength_v=inc_field.wavelength;
wavelength_2D_m=repmat(wavelength_v,1,len2);

for k=1:len3
    f1i_m(:,:,k)=inc_field.f1;
    f1r_m(:,:,k)=scat_field(k).f1r;
    f1t_m(:,:,k)=scat_field(k).f1t;
    Rss_m(:,:,k)=scat_field(k).Rss;
    Rsp_m(:,:,k)=scat_field(k).Rsp;
    Rps_m(:,:,k)=scat_field(k).Rps;
    Rpp_m(:,:,k)=scat_field(k).Rpp;
    Tss_m(:,:,k)=scat_field(k).Tss;
    Tsp_m(:,:,k)=scat_field(k).Tsp;
    Tps_m(:,:,k)=scat_field(k).Tps;
    Tpp_m(:,:,k)=scat_field(k).Tpp;
    wavelength_m(:,:,k)=wavelength_2D_m;
end

c_ti_m=real(f1t_m)./real(f1i_m);
c_ri_m=-real(f1r_m)./real(f1i_m);

R_eff_all_m=0.5*(abs(Rss_m).^2+abs(Rps_m).^2 ...
                +abs(Rsp_m).^2+abs(Rpp_m).^2).*c_ri_m;%*lagre_r;
T_eff_all_m=0.5*(abs(Tss_m).^2+abs(Tps_m).^2 ...
                +abs(Tsp_m).^2+abs(Tpp_m).^2).*c_ti_m;%*lagre_t;


real_f1r_m=[imag(f1r_m)==0]; %fjerner evanescent felt
real_f1t_m=[imag(f1t_m)==0];

%All values
R_eff_m=R_eff_all_m.*real_f1r_m; %dimension (len1, len2, len3)
T_eff_m=T_eff_all_m.*real_f1t_m;

%total efficiency
R_eff_sum_m=sum(R_eff_m,3); %dimension (len1, len2 / wavelength, parameter)
T_eff_sum_m=sum(T_eff_m,3);

%Finding the zero and first order positions
n_00_v=gdc_ak_m2n_fun(m1_v, m2_v, [0;0]);
n_01_v=gdc_ak_m2n_fun(m1_v, m2_v, [-1, -1, 0, 0, 1, 1; 0, -1, -1, 1, 1, 0]);
```

```matlab
%zero order scattering efficiencies
R_eff_00_m=R_eff_m(:,:,n_00_v); % dimension (len1, len2, 1)
T_eff_00_m=T_eff_m(:,:,n_00_v); % alle verdier for alle ordner,bølgelengder og
parameterverdier

%first order scattering efficiencies
R_eff_01all_m=R_eff_m(:,:,n_01_v); % dimension (len1, len2, 6)
T_eff_01all_m=T_eff_m(:,:,n_01_v); % verdier for alle bølgelengder og
parameterverdier, bare første ordner

%sum of first order scattering efficiencies
R_eff_01sum_m=sum(R_eff_01all_m,3); %summert over første orden,
T_eff_01sum_m=sum(T_eff_01all_m,3);

%average over all wavelengths
R_eff_ave_m=shiftdim(sum(R_eff_m,1)/length(wavelength_v));
T_eff_ave_m=shiftdim(sum(T_eff_m,1)/length(wavelength_v));

%sum over all orders
R_eff_avex2_m=shiftdim(sum(R_eff_ave_m,2));
T_eff_avex2_m=shiftdim(sum(T_eff_ave_m,2));

%first order sum averaged over wavelengths
R_eff_ave_01=shiftdim(sum(R_eff_01sum_m,1)/length(wavelength_v));
T_eff_ave_01=shiftdim(sum(T_eff_01sum_m,1)/length(wavelength_v));
```

```
function[n_v]=m2n_fun(m1_v, m2_v, m1m2_m)
Nm=length(m1_v);
[N1,N2]=size(m1m2_m);
n_v=NaN*ones(1,N2);
for n12=1:N2,
    for nm=1:nm
    if(m1_v(nm)==m1m2_m(1,n12)) & (m2_v(nm)==m1m2_m(2,n12)),
        n_v(n12)=nm;
    end
end
end
```